

**Metal Organic Framework derived
CeO₂/rGO/CeS₂ composite as efficient
supercapacitor electrode**



By

Usman Ali Khan

Reg#00000204272

Session 2017-2019

Supervised by

Dr. Naseem Iqbal

**A Thesis Submitted to the US-Pakistan Center for Advanced Studies in
Energy in partial fulfillment of the requirements for the degree of
MASTER of SCIENCE in
Energy Systems Engineering**

US-Pakistan Center for Advanced Studies in Energy (USPCAS-E)

National University of Sciences and Technology (NUST)

H-12, Islamabad 44000, Pakistan

April 2021

THESIS ACCEPTANCE CERTIFICATE

Certified that final copy of MS thesis written by Mr. **Usman Ali Khan**, (Registration No. 00000204272), of US-Pakistan Center for Advanced Studies in Energy (USPCAS-E) has been vetted by undersigned, found complete in all respects as per NUST Statues/Regulations, is within the similarity indices limit and is accepted as partial fulfillment for the award of MS degree. It is further certified that necessary amendments as pointed out by GEC members of the scholar have also been incorporated in the said thesis.

Signature: _____

Name of Supervisor _____

Date: _____

Signature (HoD ESE): _____

Date: _____

Signature (Dean/Principal): _____

Date: _____

Certificate

This is to certify that work in this thesis has been carried out by **Mr. Usman Ali Khan** and completed under my supervision in Synthesis and Energy Storage laboratory, US-Pakistan Center for Advanced Studies in Energy (USPCAS-E), National University of Sciences and Technology, H-12, Islamabad, Pakistan.

Supervisor:

Dr. Naseem Iqbal
USPCAS-E
NUST, Islamabad

GEC member # 1:

Dr. Rabia Liaquat
USPCAS-E
NUST, Islamabad

GEC member # 2:

Dr. Majid Ali
USPCAS-E
NUST, Islamabad

GEC member # 3:

Dr. Nadia Shahzad
USPCAS-E
NUST, Islamabad

HOD-(ESE):

Dr. Naseem Iqbal
USPCAS-E
NUST-Islamabad

Principal/Dean:

Dr. Adeel Waqas
USPCAS-E
NUST, Islamabad

DEDICATION

To my family and my teachers who supported me in every aspect of my life.

ACKNOWLEDGMENTS

All praise to Allah Almighty, who gave me the strength to successfully complete this dissertation. Completion of MS Degree has been a challenging, yet interesting journey filled with life lessons. As my research has been completed, I would like to take this opportunity to express sincere gratitude to my supervisor **Dr. Naseem Iqbal** for the continuous support and guidance throughout the MS program and research. I would also like to thank my guidance and evaluation committee: **Dr. Rabia Liaquat, Dr. Nadia Shahzad** and **Dr. Majid Ali** for their valuable feedback and insights which added value to this research.

I also appreciate the support of teaching and non-teaching faculty of U.S.-Pakistan Center for Advanced Studies in Energy for all the things that facilitated smooth work of my research.

I would particularly acknowledge the immense support of my dear parents who were like beacons of hope throughout this entire journey. I would also admire the wholehearted help of my friends and colleagues who always cheered for me and offered their support in every way possible.

Abstract

The excellent stability of CeO₂ coupled with the high-level conductivity of CeS₂ and enhanced electrochemical performance of rGO prove to be a workable nanocomposite electrode for supercapacitor applications. Here in this work, we synthesized mesoporous Ce-BTC metal-organic framework (MOF) derived CeO₂/rGO composite, which was then subjected to sulfidation to prepare CeO₂/rGO/CeS₂ nanocomposite, which was characterized by XRD, SEM, EDS, and TGA to find out its crystalline nature, material composition, morphology, and thermal stability. The electrochemical behavior of the metal oxide/sulfide composite was studied by making use of the cyclic voltammetry analysis (CV), chronopotentiometry (CP), and electrochemical impedance spectroscopy (EIS). The as-produced porous CeO₂/rGO/CeS₂ composite demonstrated the highest specific capacitance of 720 Fg⁻¹ in 3 M KOH electrolyte, with the specific energy and specific power of 23.5 Whkg⁻¹, and 2917.2 Wkg⁻¹ correspondingly, at a current density of 2.5 Ag⁻¹. The electrode demonstrated exceptional cyclic stability over 3000 cycles at a 100mVs⁻¹ scan rate. The brilliant electrochemical efficacy of the synthesized material was ascribed to its tiered structure. The obtained results show that the CeO₂/rGO/CeS₂ composite opens new possibilities of metal sulfide composites as efficient electrodes for supercapacitor applications.

Keywords: Electrochemical Supercapacitors, Metal-Organic Framework, Pseudocapacitance, metal-sulfide composite

Table of Contents

| | |
|--|------|
| Abstract | VII |
| List of Figures | XII |
| List of Tables | XIV |
| List of Abbreviations/Nomenclature..... | XV |
| List of Publications | XVII |
| Chapter 1 Introduction | 1 |
| 1.1 Energy Demand..... | 1 |
| 1.2 Energy Storage | 3 |
| 1.3 Energy Storage Technologies..... | 4 |
| 1.4 Types of Energy Storage Systems..... | 5 |
| 1.4.1 Flywheel Energy Storage..... | 6 |
| 1.4.2 Potential Energy Storage | 6 |
| 1.4.3 Electrochemical Energy Storage | 6 |
| 1.5 Battery Energy Storage | 7 |
| 1.5.1 Lithium Ion | 8 |
| 1.6 Energy storage in supercapacitors..... | 9 |
| 1.7 Supercapacitors vs Li-ion Batteries..... | 10 |
| 1.7.1 Energy Density | 10 |
| 1.7.2 Energy Discharging Rate..... | 11 |
| 1.7.3 Lifespan | 11 |
| 1.7.4 Energy Charging Time | 11 |
| 1.7.5 Cost..... | 11 |
| 1.7.6 Power Density..... | 11 |
| 1.7.7 Efficiency..... | 12 |
| 1.8 Problem Statement | 13 |
| Summary | 14 |
| References | 15 |
| Chapter 2 Literature Review | 19 |

| | | |
|--|---|----|
| 2.1 | Energy Storage Mechanism in Supercapacitors | 19 |
| 2.1.1 | Electrostatic Double Layer Capacitance..... | 20 |
| 2.1.2 | Electrochemical Pseudocapacitance | 21 |
| 2.2 | Electrode Materials for supercapacitors | 22 |
| 2.2.1 | Nanostructured Carbon Materials..... | 22 |
| 2.2.2 | Carbon Nanotubes (CNTs) | 22 |
| 2.2.3 | Graphene..... | 23 |
| 2.2.4 | Transition Metal Oxides/Hydroxides-Based Materials | 23 |
| 2.2.5 | Nanocomposite-Based Materials | 24 |
| 2.2.6 | Electrode materials based on zeolitic imidazolate frameworks (ZIFs) | 24 |
| 2.2.7 | MOF derived electrode materials | 25 |
| 2.2.8 | MOF-derived metal oxide/sulfide-based electrodes..... | 26 |
| 2.3 | Summary | 29 |
| | References | 30 |
| Chapter 3 Experimentation and Characterization Methods | | 33 |
| 3.1 | Synthesis Methods..... | 33 |
| 3.1.1 | Solvothermal Synthesis | 34 |
| 3.1.2 | Hydrothermal Method | 34 |
| 3.2 | Characterization Techniques | 35 |
| 3.2.1 | X-ray Diffraction | 35 |
| 3.2.2 | Scanning Electron Microscopy..... | 36 |
| 3.2.3 | Energy Dispersive Spectroscopy (EDS)..... | 37 |
| 3.2.4 | Thermo-Gravimetric Analysis..... | 38 |
| 3.2.5 | Fourier Transform Infrared Spectroscopy | 40 |
| 3.3 | Electrochemical Testing..... | 41 |
| 3.3.1 | Suspension formation | 41 |
| 3.4 | Electrochemical Workstation Techniques..... | 41 |
| 3.4.1 | Cyclic Voltammetry | 41 |
| 3.4.2 | Chronopotentiometry..... | 42 |
| 3.4.3 | Electrochemical Impedance Spectroscopy | 43 |
| 3.5 | Electrochemical parameters | 44 |

| | |
|--|----|
| Summary | 46 |
| References | 47 |
| Chapter 4 Methodology and Experimentation | 49 |
| 4.1 Materials..... | 49 |
| 4.2 Synthesis of Ce-BTC..... | 49 |
| 4.3 Preparation of CeO ₂ /rGO composite..... | 50 |
| 4.4 Ce-BTC derived CeO ₂ /rGO/CeS ₂ composite..... | 51 |
| 4.5 Material Characterization..... | 52 |
| 4.6 Electrochemical Testing..... | 52 |
| Summary | 53 |
| References | 54 |
| Chapter 5 Results and Discussion..... | 55 |
| 5.1 Material Characterization..... | 55 |
| 5.1.1 XRD..... | 55 |
| 5.1.2 Scanning Electron Microscope-SEM..... | 56 |
| 5.1.3 Transmission Electron Microscopy-TEM..... | 57 |
| 5.1.4 X-ray photoelectron spectroscopy-XPS..... | 58 |
| 5.1.5 Fourier Transform Infrared Spectroscopy-FTIR | 58 |
| 5.1.6 Raman Spectroscopy..... | 60 |
| 5.1.7 Thermal Gravimetric Analysis..... | 60 |
| 5.2 Electrochemical Measurements..... | 61 |
| 5.2.1 Cyclic Voltammetry..... | 62 |
| 5.2.2 Chronopotentiometry | 64 |
| 5.2.3 Cyclic Stability..... | 65 |
| 5.2.4 Electrochemical Impedance Spectroscopy | 66 |
| Summary | 67 |
| References | 68 |
| Chapter 6 Conclusions and Recommendation | 69 |
| 6.1 Conclusions | 69 |
| 6.2 Recommendations | 69 |
| Summary | 71 |

Appendix..... 73

List of Figures

| | |
|--|----|
| Figure 1 Consumption of energy in Developed and Developing Worlds..... | 2 |
| Figure 2 Benefits stemming from the adoption of energy storage, retrieved from “Overview of energy storage technologies for renewable energy systems.”..... | 4 |
| Figure 3 Role of Energy Storage, retrieved from Overview of energy storage technologies for renewable energy systems D. P. ZAFIRAKIS, TEI of Piraeus, Greece | 5 |
| Figure 4 Ratio of energy supply from batteries to total energy consumption | 7 |
| Figure 5 Schematic of the configuration of rechargeable Li-ion Battery | 8 |
| Figure 6 Schematic of configuration of nanocarbon based supercapacitor. | 9 |
| Figure 7 Comparison between energy storage devices based on energy and power densities..... | 10 |
| Figure 8 Difference of power densities of batteries vs supercapacitors | 12 |
| Figure 9 Difference is overall efficiency of batteries and supercapacitors..... | 13 |
| Figure 10 Comparison between Supercapacitors and Li-ion Batteries..... | 20 |
| Figure 11 Electric Double Layer Capacitor | 20 |
| Figure 12 Easy view of a double layer with specifically adsorbed ions which have submitted their charge to the electrode to clarify the pseudo-capacitance. | 21 |
| Figure 13 Graphical representation of the synthesis of N-pGr and graphene quantum dots (GQDs) and their potential application for the fabrication of the asymmetric supercapacitors (ASSC) device..... | 23 |
| Figure 14 The development of the metal organic framework (MOF) synthesis derived from porous. | 24 |
| Figure 15 Schematic illustration of $\text{Co}_3\text{O}_4/\text{C}$ nanowire array electrodes | 26 |
| Figure 16 Schematic presentation of challenges and future aspects for metal sulfides as energy material, retrieved from Current Opinion in Electrochemistry | 28 |
| Figure 17 Types of Synthesis techniques..... | 33 |
| Figure 18 Autoclave used for the hydrothermal synthesis technique. | 35 |
| Figure 19 Schematic of XRD Process | 36 |
| Figure 20 Schematic drawing of the electron and x-ray optics of a combined SEM-EPMA | 37 |

| | |
|---|----|
| Figure 21 Illustration of EDS..... | 38 |
| Figure 22 Illustration of TGA..... | 39 |
| Figure 23 Schematic diagram of FTIR. | 40 |
| Figure 24 Cyclic voltammogram..... | 42 |
| Figure 25 Chronopotentiometry, Galvanostatic charge/discharge curve..... | 43 |
| Figure 26 Electrochemical Impedance Spectroscopy. | 44 |
| Figure 27 Synthesis scheme for Ce-BTC..... | 50 |
| Figure 28 Synthesis scheme for CeO ₂ /rGO composite..... | 51 |
| Figure 29 Synthesis scheme for CeO ₂ /rGO/CeS ₂ composite..... | 52 |
| Figure 30 Represents the XRD pattern of, a) Ce-BTC, b) CeO ₂ /rGO composite and CeO ₂ /rGO/CeS ₂ composite..... | 55 |
| Figure 31 SEM images of, a) Pillar like rods of Ce-BTC, b) Cubic CeO ₂ /rGO, c) Irregular nanorods of CeO ₂ /rGO/CeS ₂ composite, and d) EDX measurements for C:O:S:Ce..... | 56 |
| Figure 32(a,b) TEM image for CeO ₂ /rGO/CeS ₂ nanocomposite at 20 nm and 10 nm respectively..... | 57 |
| Figure 33 a) XPS survey of CeO ₂ /rGO/CeS ₂ composite, b)XPS spectrum for Ce3d, c) XPS spectrum for S2p, d)XPS spectrum for C1s, e) XPS spectrum for O1s..... | 58 |
| Figure 34 FTIR spectra of CeO ₂ /rGO/CeS ₂ composite..... | 59 |
| Figure 35 Raman Spectroscopy of CeO ₂ /rGO/CeS ₂ composite..... | 60 |
| Figure 36 Thermogravimetric analysis of Ce-BTC MOF, CeO ₂ /rGO, and CeO ₂ /rGO/CeS ₂ composite..... | 61 |
| Figure 37 CV analysis at different scan rates for, (a) CeO ₂ /rGO (b) CeO ₂ /rGO/CeS ₂ (c) Comparison of CV curves for CeO ₂ /rGO and CeO ₂ /rGO/CeS ₂ (d) Scan Rate versus Specific Capacitance for CeO ₂ /rGO and CeO ₂ /rGO/CeS ₂ | 63 |
| Figure 38 Galvanic Charge-Discharge curves of, (a) CeO ₂ /rGO, (b) CeO ₂ /rGO/CeS ₂ , (c) Comparison between GCD curves of CeO ₂ /rGO and CeO ₂ /rGO/CeS ₂ | 64 |
| Figure 39 Capacitance Retention of CeO ₂ /rGO/CeS ₂ composite at 100mVs ⁻¹ for 3000 cycles..... | 65 |
| Figure 40 Electrochemical Impedance Spectroscopy (EIS) measurements, (a) Nyquist plot CeO ₂ /rGO and CeO ₂ /rGO/CeS ₂ , (b) Bode plot for CeO ₂ /rGO and CeO ₂ /rGO/CeS ₂ | 66 |

List of Tables

| | |
|--|----|
| Table 1 EDX analysis of CeO ₂ /rGO/CeS ₂ nanocomposite | 57 |
| Table 2 Scan Rates versus specific capacitances of CeO ₂ /rGO, and CeO ₂ /rGO/CeS ₂ | 63 |

List of Abbreviations/Nomenclature

| | |
|------------------|---|
| SCs | Supercapacitors |
| CAES | Compressed air energy storage |
| SMES | Superconducting magnetic energy storage |
| PHS | Pumped hydro storage |
| GO | Graphene oxide |
| rGO | Reduced graphene oxide |
| ZIF | Zeolitic imidazolate framework |
| MOF | Metal organic framework |
| NPC | Nanoporous carbon |
| MOs | Metal oxides |
| CNT | Carbon nanotubes |
| Li-ion | Lithium ion |
| Ce | Cerium |
| DMF | Dimethyl formamide |
| CeS ₂ | Cerium sulfide |
| CeO ₂ | Cerium oxide |
| TEM | Transmission electron microscope |
| XRD | X ray Diffraction |
| TGA | Thermogravimetric analysis |
| SEM | Scanning Electron Microscopy |
| E | Energy |
| EIS | Electrochemical impedance spectroscopy |
| P | Power |
| CV | Cyclic voltammetry |
| CP | Chronopotentiometry |
| C | Capacitance |
| m | Mass loading |
| r | Scan rate |

| | |
|------|---|
| V | Voltage |
| FTIR | Fourier transform infrared spectroscopy |
| EDS | Energy dispersive X-ray spectroscopy |
| XPS | X-ray photoelectron spectroscopy |
| BTC | Benzene-1,3,5-tricarboxylic acid |

List of Publications

1. **Usman Ali Khan**, Naseem Iqbal, Tayyaba Noor, Rabia Ahmad, Awais Ahmad, Zain Amjad, Abdul Wahab, "**Cerium based metal organic framework derived composite with reduced graphene oxide as efficient supercapacitor electrode**", submitted and under review at the Journal of "Energy Storage".
2. Rabia Ahmad, **Usman Ali Khan**, Naseem Iqbal, Tayyaba Noor, "**Zeolitic imidazolate framework (ZIF)-derived porous carbon materials for supercapacitors: an overview**" published at the Journal, "RSC Advances (RSC Adv., 2020, 10, 43733)."
3. Awais Ahmad, Tayyaba Noor, Ahmed Hassan, **Usman Ali Khan**, Abdul Wahab, Muhammad Arslan Raza, Sheeraz Ashraf, "**Cu-doped Zeolite Imidazole Framework (ZIF-8) for Effective Electrocatalytic CO₂ Reduction**", published at the "Journal of CO₂ Utilization (Volume 48, June 2021, 101523)."
4. Abdul Wahab, Naseem Iqbal, Tayyaba Noor, Sheeraz Ashraf, Muhammad Arslan Raza, Awais Ahmad and **Usman Ali Khan**, "**Thermally reduced mesoporous manganese MOF @reduced graphene oxide nanocomposite as bifunctional electrocatalyst for oxygen reduction and evolution**" published at the Journal, "RSC Advances (RSC Adv., 2020, 10, 27728)

Chapter 1 Introduction

1.1 Energy Demand

The developing world has been predicted to be the source of almost all the increase in the energy demand, utilization of fossil fuels, pollution, and emissions of greenhouse gases over the next 30 years. According to the “U.S. Energy Information Administration” the energy consumption in OECD will increase to about 14 % from a period of 2007 to 2035, while the increase in the energy consumption in the non-OECD countries will increase to about 84 percent of that in 2007. Whereas the two statistics were equal in the year 2007. According to research, the medium run increase in the consumption of energy will be defined by the poor countries of the world[1]. With the rise in the per capita income in addition to the rising stats of the economy of the world, the poor households in various countries of the world will be connected to the electricity grid which will become the primary cause of the rising demand of energy consumption[2]. In addition to being connected to the electricity grid, these poor households will have access to the latest electronics, good roads, and futuristic infrastructure of cities, which will impact the global energy demand[3]. The first-time purchases of the long lived and durable assets like cars and refrigerators, will have a substantial impact on the ever-increasing energy consumption and greenhouse gas emissions.

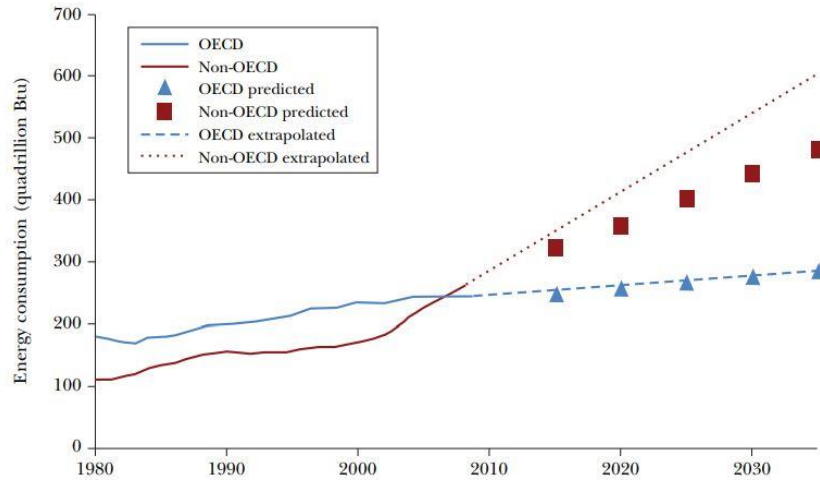


Figure 1 Consumption of energy in Developed and Developing Worlds

Largely, the association between the consumption of energy and economic growth in developing world has already been, and is expected to continue to be, severely inclined to the extent that the growth is “pro-poor”[4]. Moreover, it is also discussed in research that the existing projections for the demand of energy in the developing world might be rendered discreet, as the increase in the demand is not correctly measured along the extensive margin.

Figure 1, by making use of the statistics from the year 1980 to 2008 and the projections to upto 2035, explains the utilization of energy in both the developing world and the developed world[5]. The squares and triangles show the projections of the evolving trend of the use of energy. Evidently, according to the figure, most of the improvement in energy use is set to be in the developing countries.

Due to the ever-rising requirement of electrical energy in the current era, owing to the increase in the use of electronic devices, the scientific world has been focusing on harvesting energy from renewable resources like wind, solar, thermal, etc[6]. This increase in energy production has given rise to the need for efficient storage devices, i.e., Batteries and supercapacitors. Li-ion batteries are being developed and used for this very purpose for some time now. These batteries help improve the technological advancements ranging from compact electric gadgets to electric automobiles and renewable power generation and storage systems[7]. Among various examples of the use of batteries is the Hybrid Electric

Vehicle which uses a combination of a battery, an electric motor, and a combustion engine to increase the efficiency of the fuel. Lithium-ion batteries despite having the maximum energy densities of all other energy storage systems demonstrate lower levels of specific power and cycle life[8]. To cater to the specific power and cycle life, a new and more efficient storage device has been of significant importance these days, i.e., supercapacitors. Supercapacitors have drawn a lot of interest in the last decade due to their efficient cycle life, high charge/discharge rate, and high power density[9]. Supercapacitors are among the new energy storage devices that are raising a considerable amount of attention to be used as power sources for various electronic devices due to the marvelous electrochemical capabilities[10]. The search for innovative materials and combination of materials to be used as electrodes of supercapacitors has been developing in the research community. So far, among various promising candidates, research has been focused on the porous materials like carbon and its derivatives as they possess considerable large surface areas and good conductivities which allows these materials to store more charge and for longer periods of time. Nevertheless, the overall capacitance of supercapacitors made with such materials is rather low.

1.2 Energy Storage

The electricity that is being generated from various renewable resources, that ensures extraordinary development around the world, can hardly deliver abrupt response to the energy demand as the supply from these sources is not easily adaptable to the global consumption requirements. Hence, the development of the distributed production refers to the increased problems of network load stability and it needs to store the energy, typically using the Li ion batteries[11]. Though, lead-acid batteries are not able to endure large cycle rates in addition to the inability to store a considerable amount of energy in a limited volume. This gives rise to the development of alternate energy storage technologies and makes energy storage of prime importance in the energy generated from various renewable resources, which allows the generated energy to be integrated into the electricity grid in peak consumption hours.

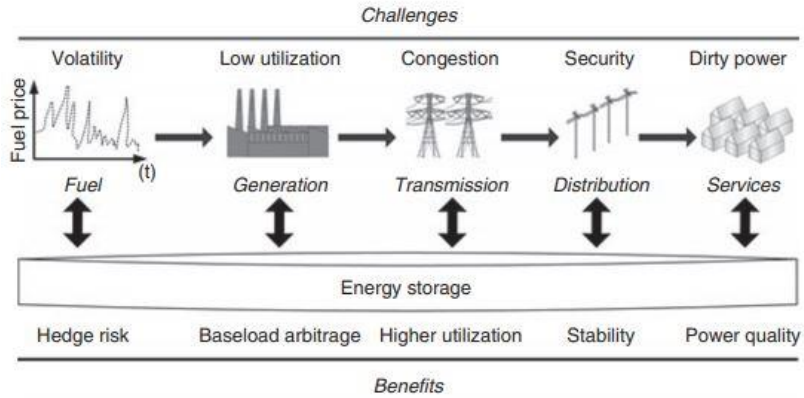


Figure 2 Benefits stemming from the adoption of energy storage, retrieved from “Overview of energy storage technologies for renewable energy systems.”

The advantages of the modern energy storage systems can be explained briefly as the effective utilization of the energy that was previously wasted, improved reliance on energy supply, and the efficient operation of the existing power plants. Though, energy storage systems are handled with skeptical perception, which is due to the considerably initial cost of such systems in addition to the transformation and integration losses[12]. The implementation of energy storage systems makes it possible for the base-load arbitrage and reduction of risk required by the unpredictability of the fuel price, supports increased usage and clearing out of the usually entangled transmission lines, confirms the firmness of the distribution system and delivers better quality power to the end consumer. (Figure 2).

1.3 Energy Storage Technologies

There are two basic challenges in the field of energy storage: first being the requirement of improvement in the existing power networks that are centralized and of conventional design, and second being the shift towards the new era of distributed energy generation based on the renewable energy systems[13]. Modern technologies consist of pumped hydro storage (PHS), fuel cell technology, compressed air energy storage (CAES), flywheels, supercapacitors (SCs), superconducting magnetic energy storage (SMES) and various battery systems (Figure 3).

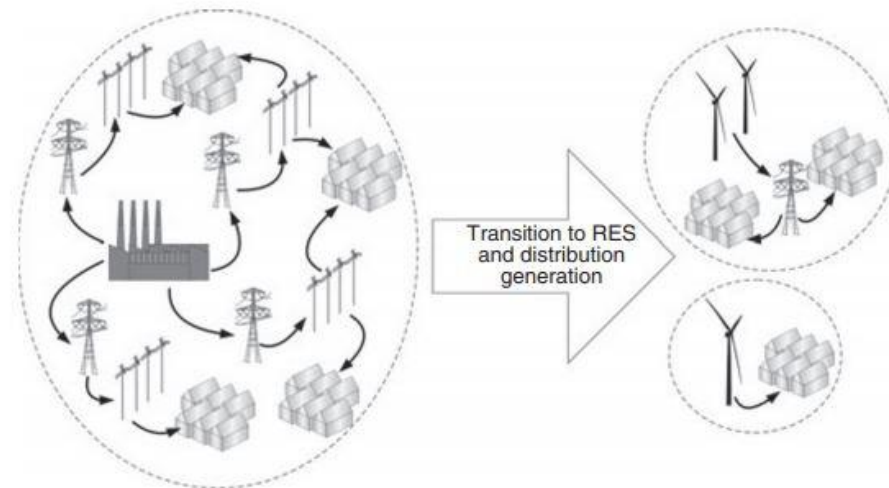


Figure 3 Role of Energy Storage, retrieved from Overview of energy storage technologies for renewable energy systems D. P. ZAFIRAKIS, TEI of Piraeus, Greece

The energy storage systems include various forms of energies, technologies, and corresponding applications. Energy can be stored in the form of chemical, kinetic, electrical, potential or even thermal energy[14]–[16]. Once the energy has been stored in any form, it can be directly or indirectly converted in order to be utilized. In terms of direct conversion, when certain amount of heat is extracted from a thermal energy store, it is the direct conversion of energy. On the other hand, in terms of indirect conversion when a turbine generator is used to generate electricity from a pumped hydro storage system, it is indirect conversion of energy[17], [18]. Overall, the energy storage systems are referred to as thermal or electrical. In case of electrical energy storage systems, all the technologies with electrical external interface, can be integrated.

1.4 Types of Energy Storage Systems

There are various forms energy storage systems. The systems of prime importance in context to this work are:

- Electrochemical energy storage systems
- Kinetic energy storage systems
- Potential energy storage systems

1.4.1 Flywheel Energy Storage

This is a kind of energy storage system that relies on the kinetic energy stored in a rotating drum known as the flywheel. In this type of kinetic energy storage system, a motor or a generator is used for the energy conversion during the operation[19]. Typically, there are two types of flywheel energy storage systems: first being the conventional steel rotor system that runs at a considerably low speed, and second being the advanced composite machine that runs at high speeds.

1.4.2 Potential Energy Storage

The pumped hydro energy storage system and the compressed air energy storage systems use the potential energy storage mechanism, where the former is extensively used across the world in various power systems, and it comprises of an installed capacity of over 90 GW. According to the principle of operation of the pumped hydro storage, when the supply of water is surplus the water is shifted to a reservoir on an upper level which is then discharged in times of high energy demand, through a turbo-alternator. The latter systems, i.e., the compressed air energy storage systems are comparatively less in number, i.e., two units exist in Huntorf and McIntosh. The operational procedure of the compressed air energy storage systems depicts the procedure of the split gas turbine where an underground cavity is used to store highly compressed air, which is expanded in times of high energy demand.

1.4.3 Electrochemical Energy Storage

According to the research in the field of energy storage, it is evident that the technologies based on the lithium-based cells will be represented as the apex point in the development of battery storage systems on the basis of specific energy. Development and research in the lithium-based cells and transition metal-based cells will benefit the energy storage technologies in the future as these materials will be used as electrodes, current collectors, etc. Various material combinations and composites are being studied for the fabrication of electrodes to be used in the electrochemical energy storage applications[20]. Similarly, innovative approach is being implemented for the development of various materials and designs based on the market demand to improve the energy densities of the storage equipment in addition to increasing the cycle life.

1.5 Battery Energy Storage

Batteries are known to be an established equipment used for the storage of electrical power in the form of chemical energy. Basic classifications of batteries include the primary batteries and the secondary batteries. The former type refers to the non-rechargeable batteries while the latter refers to the rechargeable batteries[21]. Assembly of a battery comprises of one or more electrochemical cells, negative and positive electrodes, and an electrolyte which can be a liquid, a solid or a paste like material[22]. The charging of a battery takes place with the help of an external potential or voltage, where an electron flow is generated in the external circuit resulting from chemical reactions at the electrodes. In case of the discharging process, the direction of flow is reversed. The range of the type of batteries is considerably large. It starts from the lead-acid batteries to the latest developed battery systems like Lithium-ion, Sodium-ion battery systems etc[23], [24]. Out of all the battery systems in place, the Li-ion batteries have become the primary source of the attention of the researchers and the commercial market.

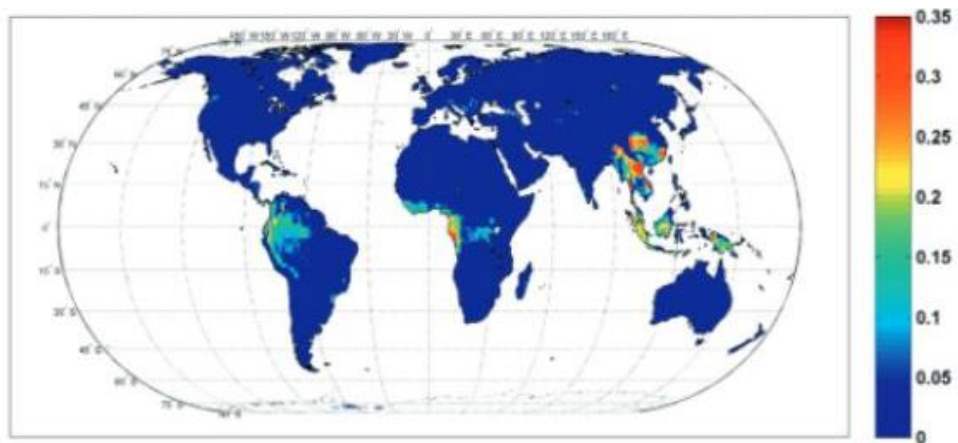


Figure 4 Ratio of energy supply from batteries to total energy consumption

Figure 4 represents the amount of energy supplied with the help of batteries is different parts of the world[25]. It can be seen that currently there is a lot of potential in expanding the battery energy storage systems.

1.5.1 Lithium Ion

The development of the Lithium-ion battery systems has been a rather fast paced process. It has emerged to be a significant global market product for various application in a very short period of 20 years[26]. The Li-ion technology has become a very attractive storage system in the market owing to its 3Cs applications as this technology has proven to provide high energy densities and power densities in addition to a very reasonable cycle life. The basic operational procedure of the Li-ion batteries comprises of a reversible transfer of Li-ions (Figure 5)[27]. The charging process de-intercalates the lithium ions from the metal oxide cathode towards the graphite anode. While on the other hand, in the case of discharging of the battery, the reverse happens[28], [29]. The role pf the electrolyte in this whole process is to conduct the lithium ions during the charging and discharging of the battery.

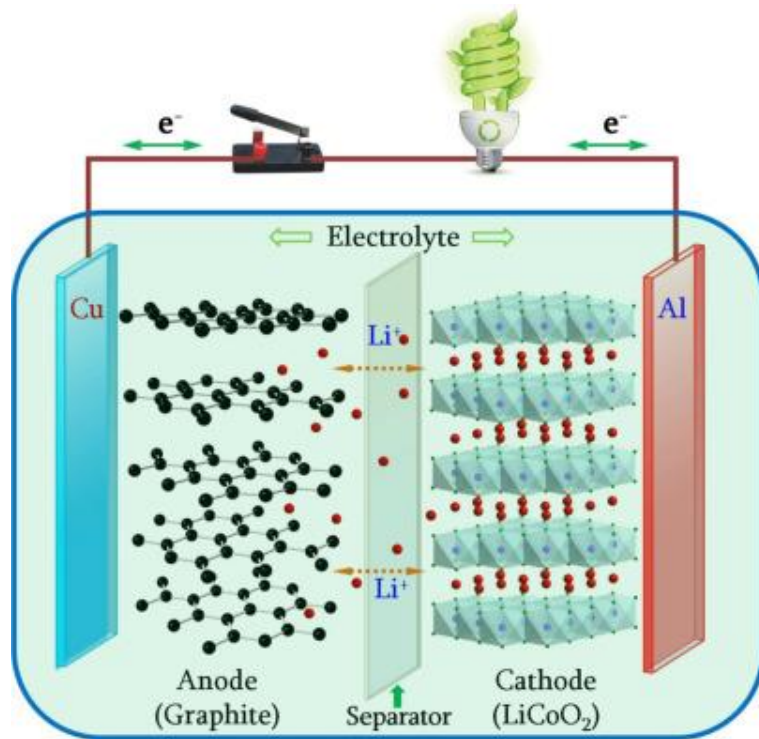


Figure 5 Schematic of the configuration of rechargeable Li-ion Battery

The lithium-ion technology possesses a few limitations in addition to the advantages of the system. For instance, these systems are supposed to be operated in a defined operational limit in order to avoid damages to the electrochemical cells[26]. Also, there does not exist

any innate ability of the technology to align the total amount of charge in the cells. Considering the advantages and the disadvantages, it is evident that these systems require effective and reliable management systems to avoid any irregularities and damages.

1.6 Energy storage in supercapacitors

Supercapacitors are a type of electrochemical devices that comprise of a combination of capabilities including the batteries and conventional capacitors (Figure 6). In supercapacitors, the energy is stored in the form of electric field lying between the two electrodes[30]. This is same working principle as of the conventional capacitors, but in this case the central insulator is replaced with an ionic electrolyte that is used to conduct the ions along an electrode containing a large surface area[31]. The energy density obtained in the case of supercapacitors is far greater than that of conventional capacitors. The cost of these devices is relatively higher, but the discharge time is also significantly better because of the relatively slower displacement of ions in the conducting electrolyte. The drawback of this technology is that the operating voltage has a limited value, i.e., even the maximum value for the voltage is only a few volts for each element.

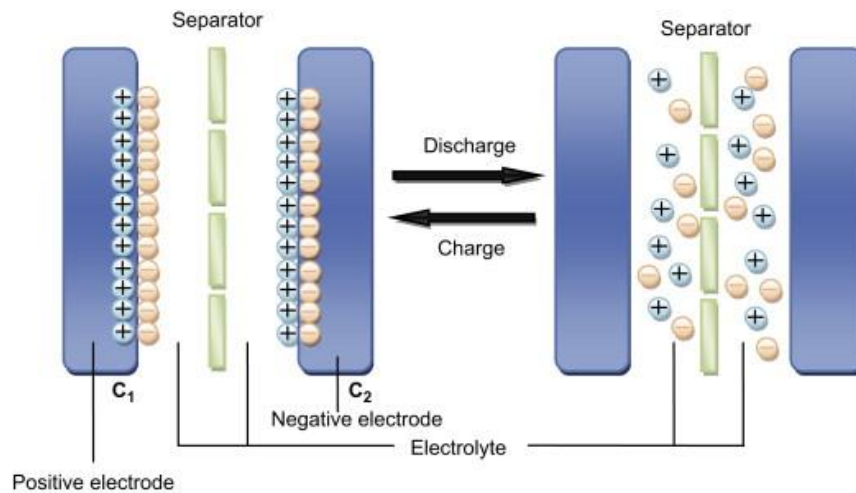


Figure 6 Schematic of configuration of nanocarbon based supercapacitor.

The increasing energy demand in the entire world calls for a dedicated research and development of energy storage devices at lower costs but with higher overall performance. Currently a lot of research has been done on the carbon-based electrodes for

supercapacitors and a lot of venues in this research filed are yet to be exploited to attain a better product with higher energy and power densities in addition to increased cycle life and stability[32], [33]. In addition to the research on electrode materials, there is a need to work on the types of electrolytes suitable for better performance of supercapacitors. Also, the package design of the supercapacitors should also be altered in order to enhance the overall performance of the device to be used in various applications.

1.7 Supercapacitors vs Li-ion Batteries

1.7.1 Energy Density

The basic difference between batteries and supercapacitors lies in the energy densities of the two devices. The energy density of batteries is considerably higher than that of supercapacitors. The weight of the device helps in defining the energy density of that device. It is clear from the figure that the energy densities of battery systems are very much higher than that of supercapacitors. (Figure 7)

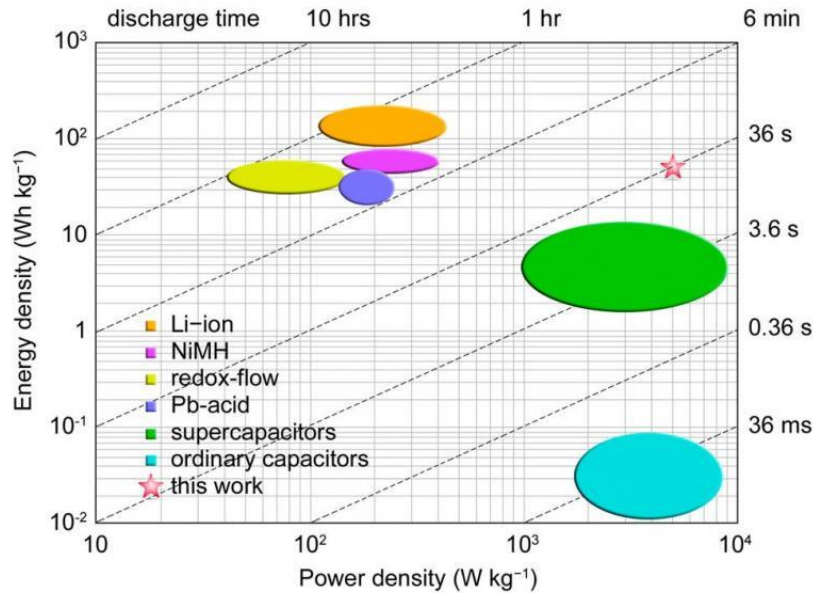


Figure 7 Comparison between energy storage devices based on energy and power densities.

1.7.2 Energy Discharging Rate

Various electronic devices like smartphones are not fitted with supercapacitors as their energy storage devices because the energy discharge rate in supercapacitors is extremely high than that of batteries, which means that the supercapacitors does not have the ability to contain electrical power for long periods of time. Typically, supercapacitors discharge almost twenty percent more power in a day than their battery counterparts. While on the other hand, batteries are able to hold power for longer period of time.

1.7.3 Lifespan

The total lifespan of supercapacitors is longer than that of batteries. For instance, a lead acid battery can do no more than 1000 charge-discharge cycles while a supercapacitor can go for more than a million cycles. This explains the fact that a supercapacitor needs to be replaced every 20 years while batteries are needed to be replaced after 5 years or so.

1.7.4 Energy Charging Time

The charging time for supercapacitors is very short as compared to that of batteries. Supercapacitors are known to have small discharge times, but they also get fully charged in almost no considerable time. This means that supercapacitors are the best choice if a device is needed to be charged faster without the need of excessive energy for a considerable period of time. On the other hand, batteries require a lot of time to get fully charged. But unlike supercapacitors, the batteries are not needed to be charged frequently as the energy density is far greater than that of supercapacitors.

1.7.5 Cost

The cost of supercapacitors is a severe limiting factor for this energy storage technology. Supercapacitors are far more expensive than batteries, i.e., a supercapacitor is ten times more costly than a battery of the exact same capacity. The great difference in the cost is one of the reasons supercapacitors are not as popular as batteries in the market.

1.7.6 Power Density

The power density of supercapacitors is far more than batteries, which means that a supercapacitor can provide energy instantly when required while a battery is unable to

provide huge burst of energy in times of an emergency. The Figure 8 below shows a comparison between the power densities of supercapacitors vs batteries.

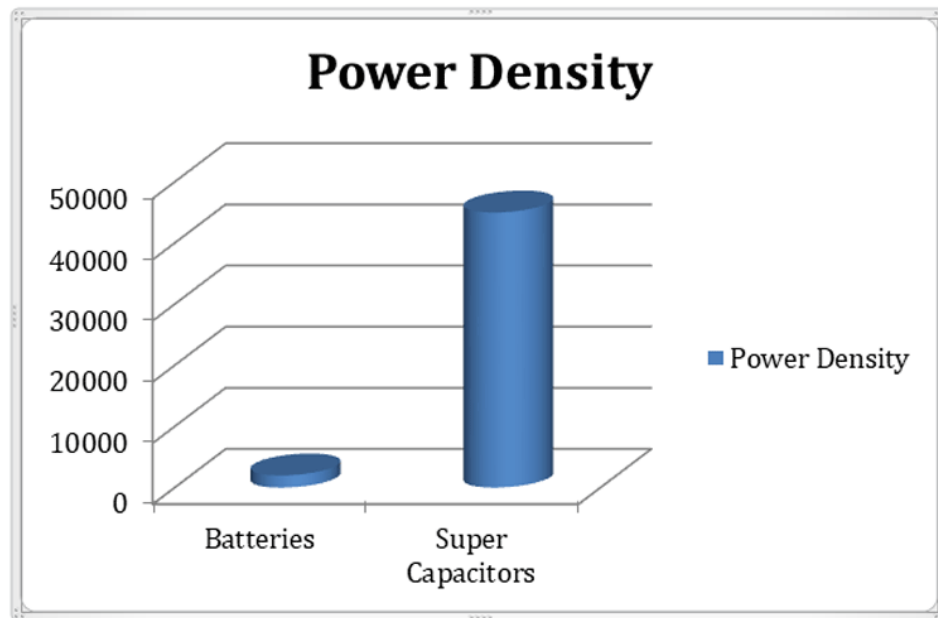


Figure 8 Difference of power densities of batteries vs supercapacitors

1.7.7 Efficiency

Batteries are typically 60 to 80 % efficient when full load is applied while a supercapacitor can be up to 95% efficient under the same conditions. This is because, the batteries dissipate tremendous amount of heat when extreme load is applied[29]. Moreover, while operating a battery, it requires constant monitoring of the temperature and other parameters to avoid any disfunction while a supercapacitor does not require such kind of monitoring, however, a supercapacitor also releases a normal amount of heat during operation, but this heat is relatively negligible as compared to batteries. Figure 9 demonstrates the difference in efficiencies of supercapacitors vs batteries.

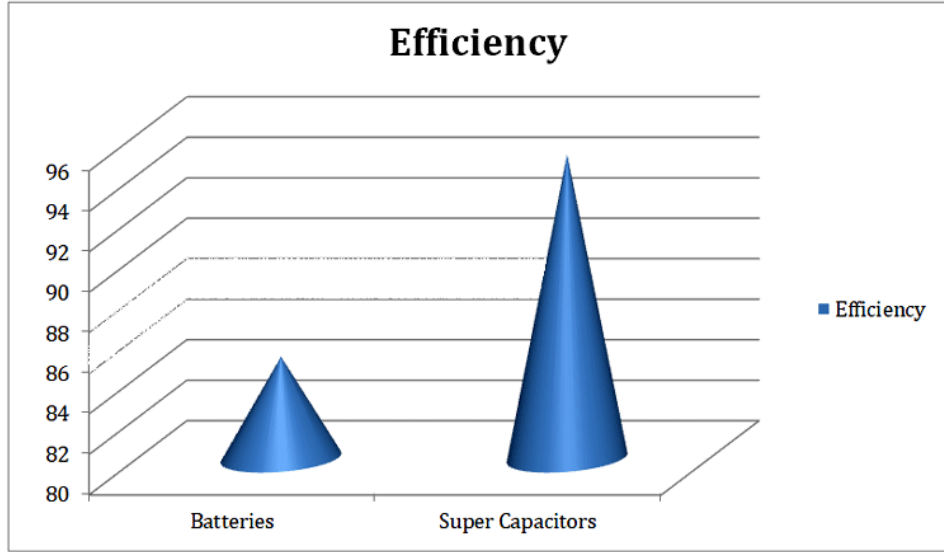


Figure 9 Difference is overall efficiency of batteries and supercapacitors.

1.8 Problem Statement

This work is an attempt to acknowledge the significance of rare earth metals, and their derivatives in electrochemical applications, especially as electrode materials for supercapacitors. This work discusses that the transition metal oxides show promising specific capacitance but metal sulfide composites with reduced graphene oxide based on a template of metal organic framework demonstrate high specific capacitance and better stability.

Summary

This chapter discusses the global energy demand and the increasing need for better and efficient energy storage devices. It also discusses the efficiency of available energy storage systems and their comparison.

References

- [1] R. G. Newell, D. Raimi, and G. Aldana, “Global Energy Outlook 2019: The Next Generation of Energy,” 2019. Accessed: May 25, 2021. [Online]. Available: www.rff.org/geo.
- [2] N. Armaroli and V. Balzani, “The future of energy supply: Challenges and opportunities,” *Angewandte Chemie - International Edition*, vol. 46, no. 1–2. John Wiley & Sons, Ltd, pp. 52–66, Jan. 01, 2007, doi: 10.1002/anie.200602373.
- [3] E. De Cian and I. Sue Wing, “Global Energy Consumption in a Warming Climate,” *Environ. Resour. Econ.*, vol. 72, no. 2, pp. 365–410, Feb. 2019, doi: 10.1007/s10640-017-0198-4.
- [4] P. V. Kamat, “Meeting the clean energy demand: Nanostructure architectures for solar energy conversion,” *J. Phys. Chem. C*, vol. 111, no. 7, pp. 2834–2860, Feb. 2007, doi: 10.1021/jp066952u.
- [5] “International Energy Outlook 2020.” <https://www.eia.gov/outlooks/ieo/> (accessed May 26, 2021).
- [6] F. Birol, “WORLD ENERGY PROSPECTS AND CHALLENGES.”
- [7] D. Steward, A. Mayyas, and M. Mann, “Economics and challenges of Li-ion battery recycling from end-of-life vehicles,” in *Procedia Manufacturing*, Jan. 2019, vol. 33, pp. 272–279, doi: 10.1016/j.promfg.2019.04.033.
- [8] Y. Miao, P. Hynan, A. Von Jouanne, and A. Yokochi, “Current li-ion battery technologies in electric vehicles and opportunities for advancements,” *Energies*, vol. 12, no. 6. MDPI AG, p. 1074, Mar. 20, 2019, doi: 10.3390/en12061074.
- [9] M. Passalacqua, D. Lanzarotto, M. Repetto, and M. Marchesoni, “Advantages of using supercapacitors and silicon carbide on hybrid vehicle series architecture,” *Energies*, vol. 10, no. 7, p. 920, Jul. 2017, doi: 10.3390/en10070920.
- [10] S. Banerjee, B. De, P. Sinha, J. Cherusseri, and K. K. Kar, “Applications of

- supercapacitors,” in *Springer Series in Materials Science*, vol. 300, Springer, 2020, pp. 341–350.
- [11] Y. Li and J. Lu, “Metal-Air Batteries: Will They Be the Future Electrochemical Energy Storage Device of Choice?,” *ACS Energy Letters*, vol. 2, no. 6. American Chemical Society, pp. 1370–1377, Jun. 09, 2017, doi: 10.1021/acsenergylett.7b00119.
- [12] M. A. Hessami, H. Campbell, and C. Sanguinetti, “A feasibility study of hybrid wind power systems for remote communities,” *Energy Policy*, vol. 39, no. 2, pp. 877–886, Feb. 2011, doi: 10.1016/j.enpol.2010.11.011.
- [13] J. Howes, “Concept and development of a pumped heat electricity storage device,” in *Proceedings of the IEEE*, 2012, vol. 100, no. 2, pp. 493–503, doi: 10.1109/JPROC.2011.2174529.
- [14] A. Smallbone, V. Jülch, R. Wardle, and A. P. Roskilly, “Levelised Cost of Storage for Pumped Heat Energy Storage in comparison with other energy storage technologies,” *Energy Convers. Manag.*, vol. 152, pp. 221–228, Nov. 2017, doi: 10.1016/j.enconman.2017.09.047.
- [15] M. Aneke and M. Wang, “Energy storage technologies and real life applications – A state of the art review,” *Applied Energy*, vol. 179. Elsevier Ltd, pp. 350–377, Oct. 01, 2016, doi: 10.1016/j.apenergy.2016.06.097.
- [16] T. M. Gür, “Review of electrical energy storage technologies, materials and systems: Challenges and prospects for large-scale grid storage,” *Energy and Environmental Science*, vol. 11, no. 10. Royal Society of Chemistry, pp. 2696–2767, Oct. 01, 2018, doi: 10.1039/c8ee01419a.
- [17] A. Palacios, C. Barreneche, M. E. Navarro, and Y. Ding, “Thermal energy storage technologies for concentrated solar power – A review from a materials perspective,” *Renewable Energy*, vol. 156. Elsevier Ltd, pp. 1244–1265, Aug. 01, 2020, doi: 10.1016/j.renene.2019.10.127.

- [18] B. P. Tarasov *et al.*, “Metal hydride hydrogen storage and compression systems for energy storage technologies,” *Int. J. Hydrogen Energy*, vol. 46, no. 25, pp. 13647–13657, Apr. 2021, doi: 10.1016/j.ijhydene.2020.07.085.
- [19] A. G. Olabi, T. Wilberforce, M. A. Abdelkareem, and M. Ramadan, “Critical Review of Flywheel Energy Storage System,” *Energies*, vol. 14, no. 8, p. 2159, Apr. 2021, doi: 10.3390/en14082159.
- [20] P. Poizot, J. Gaubicher, S. Renault, L. Dubois, Y. Liang, and Y. Yao, “Opportunities and Challenges for Organic Electrodes in Electrochemical Energy Storage,” *Chemical Reviews*, vol. 120, no. 14. American Chemical Society, pp. 6490–6557, Jul. 22, 2020, doi: 10.1021/acs.chemrev.9b00482.
- [21] Y. Yang, S. Bremner, C. Menictas, and M. Kay, “Battery energy storage system size determination in renewable energy systems: A review,” *Renewable and Sustainable Energy Reviews*, vol. 91. Elsevier Ltd, pp. 109–125, Aug. 01, 2018, doi: 10.1016/j.rser.2018.03.047.
- [22] P. Denholm, J. Nunemaker, P. Gagnon, and W. Cole, “The potential for battery energy storage to provide peaking capacity in the United States,” *Renew. Energy*, vol. 151, pp. 1269–1277, May 2020, doi: 10.1016/j.renene.2019.11.117.
- [23] J. Jiang, Y. Li, J. Liu, X. Huang, C. Yuan, and X. W. Lou, “Recent advances in metal oxide-based electrode architecture design for electrochemical energy storage,” *Advanced Materials*, vol. 24, no. 38. John Wiley & Sons, Ltd, pp. 5166–5180, Oct. 02, 2012, doi: 10.1002/adma.201202146.
- [24] M. Killer, M. Farrokhseresht, and N. G. Paterakis, “Implementation of large-scale Li-ion battery energy storage systems within the EMEA region,” *Applied Energy*, vol. 260. Elsevier Ltd, p. 114166, Feb. 15, 2020, doi: 10.1016/j.apenergy.2019.114166.
- [25] *Advancing the science of climate change*. National Academies Press, 2011.
- [26] T. Chen *et al.*, “Applications of Lithium-Ion Batteries in Grid-Scale Energy Storage

- Systems,” *Transactions of Tianjin University*, vol. 26, no. 3. Tianjin University, pp. 208–217, Jun. 01, 2020, doi: 10.1007/s12209-020-00236-w.
- [27] C. Liu, Z. G. Neale, and G. Cao, “Understanding electrochemical potentials of cathode materials in rechargeable batteries,” *Materials Today*, vol. 19, no. 2. Elsevier B.V., pp. 109–123, Mar. 01, 2016, doi: 10.1016/j.mattod.2015.10.009.
- [28] A. Maheshwari, N. G. Paterakis, M. Santarelli, and M. Gibescu, “Optimizing the operation of energy storage using a non-linear lithium-ion battery degradation model,” *Appl. Energy*, vol. 261, p. 114360, Mar. 2020, doi: 10.1016/j.apenergy.2019.114360.
- [29] S. I. AL-Saedi, A. J. Haider, A. N. Naje, and N. Bassil, “Improvement of Li-ion batteries energy storage by graphene additive,” in *Energy Reports*, Feb. 2019, vol. 6, pp. 64–71, doi: 10.1016/j.egy.2019.10.019.
- [30] B. Yang *et al.*, “Applications of battery/supercapacitor hybrid energy storage systems for electric vehicles using perturbation observer based robust control,” *J. Power Sources*, vol. 448, p. 227444, Feb. 2020, doi: 10.1016/j.jpowsour.2019.227444.
- [31] C. V. V. Muralee Gopi, R. Vinodh, S. Sambasivam, I. M. Obaidat, and H. J. Kim, “Recent progress of advanced energy storage materials for flexible and wearable supercapacitor: From design and development to applications,” *Journal of Energy Storage*, vol. 27. Elsevier Ltd, p. 101035, Feb. 01, 2020, doi: 10.1016/j.est.2019.101035.
- [32] Y. Zhou *et al.*, “Two-birds-one-stone: Multifunctional supercapacitors beyond traditional energy storage,” *Energy and Environmental Science*, vol. 14, no. 4. Royal Society of Chemistry, pp. 1854–1896, Apr. 01, 2021, doi: 10.1039/d0ee03167d.
- [33] Q. Guo, X. Zhao, Z. Li, B. Wang, D. Wang, and G. Nie, “High Performance Multicolor Intelligent Supercapacitor and Its Quantitative Monitoring of Energy Storage Level by Electrochromic Parameters,” *ACS Appl. Energy Mater.*, vol. 3, no. 3, pp. 2727–2736, Mar. 2020, doi: 10.1021/acsaem.9b02392.

Chapter 2 Literature Review

2.1 Energy Storage Mechanism is Supercapacitors

As of right now, batteries are the leading energy storage devices when it comes to the electrochemical energy storage. These days Li-ion batteries are used to power various electronic devices in addition to the electric vehicles in the market[1]. The operational procedure of batteries is electrochemical, and it can be explained in terms of the charging and discharging of the battery. In a typical procedure, when the battery is discharging, the Li-ions move from the anode towards the cathode, and in doing so it releases energy which is then extracted through an external circuit. During the charging process of the battery, Li-ions are moved towards the lower energy cathode with the help of an external energy. As the processes of charging and discharging take place with the help of chemical reactions, the electrode materials are deteriorated overtime in addition to it being a very slow process. This makes batteries low in power density and the cycle life of the batteries also deteriorates faster than that of supercapacitors.

The storage mechanism for supercapacitors is quite different than that of the batteries as the storage mechanism is electrostatic in nature Figure 10. In the storage procedure of supercapacitors, the energy is stored on the surface of electrodes without the use of any chemical reactions[2]. The absence of chemical reactions renders the supercapacitors to have high power densities and the materials do not deteriorate overtime[3]. The lack of deterioration of materials makes it possible for the supercapacitors to have millions of cycles of charging and discharging but the energy densities of these devices tend to be very low.

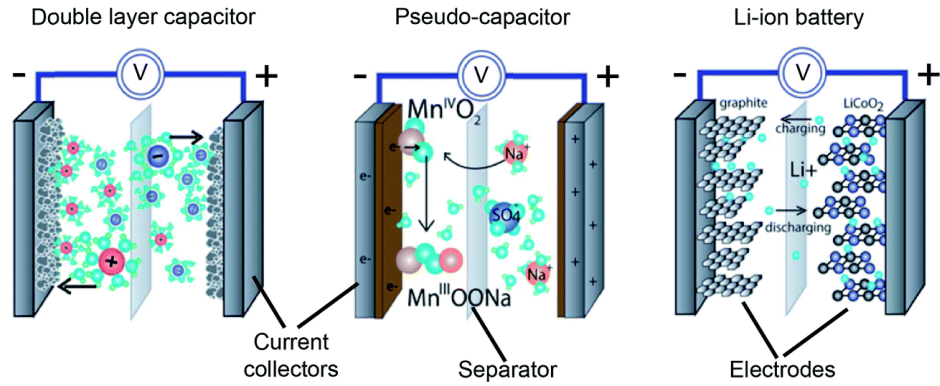


Figure 10 Comparison between Supercapacitors and Li-ion Batteries

2.1.1 Electrostatic Double Layer Capacitance

In 1950 in a US patent the conception of electrochemical double layer was proposed in which working principle of supercapacitor was expressed. After that various models like Helmholtz model, Grahame model, Gouy-Chapman model and Gouy-Chapman-Stein model have been explained which gave the performance for electrodes under potentiostatic control in electrolyte. In general, an EDLC can be referred to as an electrochemical capacitor but the charge storage mechanism is electrostatic in nature[4]. As the electrode is immersed into the electrolyte, spontaneously two opposite charges appear at the electrode-electrolyte interface Figure 11. The appeared charges form a double layer of electric charge on the interface. The dielectric between the two layers of charges is made up of a solvent or water molecules[5]. The dielectric formed between the charges prevents them from flowing across the interface.

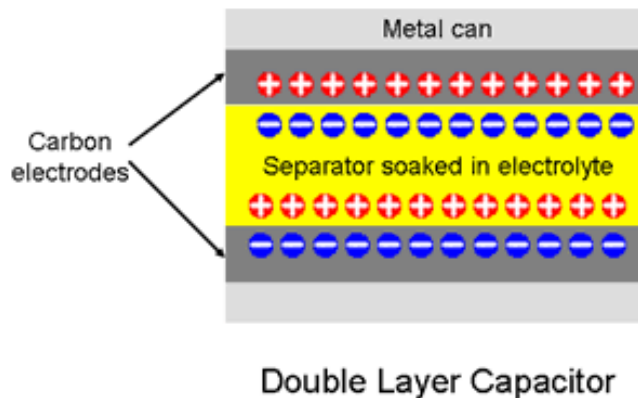


Figure 11 Electric Double Layer Capacitor

2.1.2 Electrochemical Pseudocapacitance

Unlike EDLC, this method totally depends on swift and reversible redox reactions and it stores energy faradaically. The energy densities of pseudocapacitors greater than the EDLCs because of the fast and reversible transference of charge through faradaic reactions Figure 12. During the charging of the supercapacitor, the ions in the electrolyte tend to proceed towards the electrodes forming a double layer[6], [7]. This pseudocapacitive behavior is achieved by the transfer of charge between the electrodes and electrolyte. The ion that is adsorbed on the surface does not undergo any chemical reaction with the electrode material but only charge transfer is occurred. The difference in batteries and pseudocapacitors lies in the fact that redox reactions only occur at the surface of the electrode which does not deteriorate the electrode material resulting in increased stability.

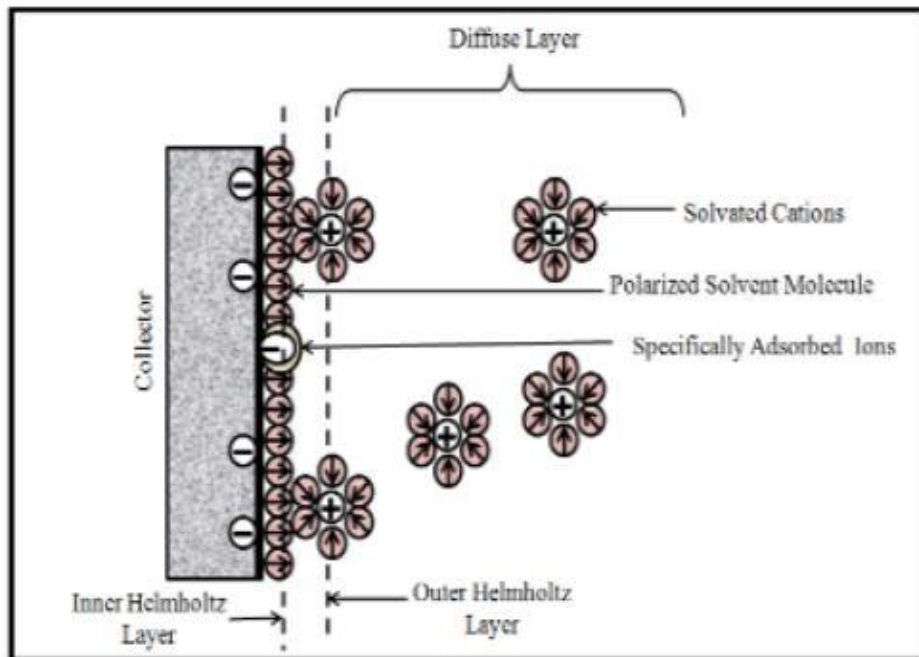


Figure 12 Easy view of a double layer with specifically adsorbed ions which have submitted their charge to the electrode to clarify the pseudo-capacitance.

2.2 Electrode Materials for supercapacitors

The capacitance of the device is mostly reliant on properties of the electrode materials. Electrodes must have the properties as good conductivity, high chemical stability, controlled pore structure, high corrosion resistance, temperature stability, processability, environmentally friendly and low cost[8]. The capacitance can be increased due to the capacity of the material to carry out faradaic transfer of charge. The thickness of the double layer and charge stored by electrochemical pseudocapacitance mechanism highly depends upon the electrode surface area. So spongy, porous material can be used as electrode[9]. By porous electrode material having proper structure that matches with the size of the electrolyte ions improves the electrochemical performance. Suitable pore size distribution has greater influence on capacitance, specific energy, equivalent series resistance and specific power.

2.2.1 Nanostructured Carbon Materials

The first ever EDLC was developed by Becker in 1975 with the help of carbon materials. Due to the various properties of the carbon materials like cost effectiveness, environment friendly nature, large surface area, and rather simple synthesis procedures, they are mostly used as electrode materials for EDLCs[3]. Moreover, the electrochemical performance of the EDLCs made with carbon based materials as electrodes is a significant improvement over the previously used materials which makes the carbonaceous materials effective electrode materials[10]. Similarly, the enhanced capacitance of the EDLCs is because of the large specific surface area and the high porous nature of the carbonaceous materials.

2.2.2 Carbon Nanotubes (CNTs)

The electrodes fabricated from carbon nanotubes comprise of various useful properties like the high porosity, large surface area, thermal stability, and high electrical conductivity. The large specific surface area of the carbon nanotube electrodes can be better accessed due to the increased mechanical agility of the CNTs, which provides better interconnection and distribution[10]. CNTs can be coupled with other materials to make a composite electrode for supercapacitor devices. These materials include graphene, metal oxides, metal sulfides, etc. The composite made by the combination of CNTs and graphene shows a promising electrochemical performance and considerable rectangular geometry.

2.2.3 Graphene

Graphene is a carbon material which comprise of a layered structure Figure 13. The layers of graphene are one atom thick where the carbon atoms have sp^2 hybridization. The carbon atoms in graphene are arranged in a honey-comb pattern making up the crystal structure of graphene[11]–[13]. Owing to the unique properties of graphene it demonstrates better mechanical properties, electrochemical capabilities, and phenomenal morphological properties in addition to large surface area and high electrical conductivity. Owing to these unique properties, graphene can be known as a promising candidate for the fabrication of electrode materials for supercapacitors.

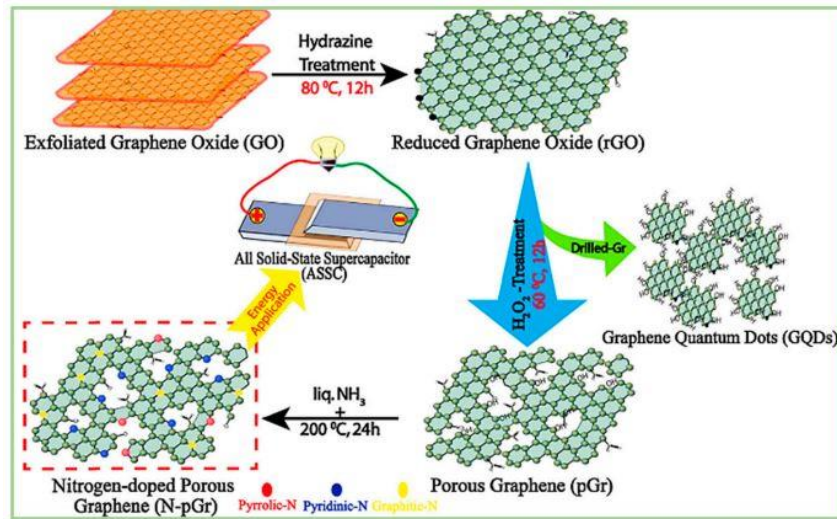


Figure 13 Graphical representation of the synthesis of N-pGr and graphene quantum dots (GQDs) and their potential application for the fabrication of the asymmetric supercapacitors (ASSC) device

2.2.4 Transition Metal Oxides/Hydroxides-Based Materials

Transition metal oxides and hydroxides are used as electrode materials for supercapacitor applications, and they provide better capacitance due to the redox-active nature. Various transition metal oxides are being used and studied as effective electrode materials (Figure 14). For instance, a few transition metals used for this purpose are Co, Fe, Ti, etc.

Tin has been reported in literature before for converting carbondioxide to formate and formic acid with high activity and selectivity. Lee et al. tested Sn particles by loading them

and sizes of the material by the combination of organic compounds with the inorganic compounds[9], [15], [16]. ZIFs can also be converted into porous carbon materials with the help of pyrolysis. Owing to the porous structure of the ZIFs, they can also be used as a sacrificial template for the synthesis of various metal oxides and sulfide composites. As a sacrificial template, ZIFs provide an increased interfacial movement of charges due to their increased surface area. In comparison to the other templates and materials that are manufactured by traditional techniques, the ZIFs have an advantage in terms of the facile synthesis procedures as it provides better control of the physiochemical characteristics[17]. Recently, ZIFs and ZIF derived materials have become a point of interest for the researchers in the field of energy storage and electrochemical applications.

2.2.7 MOF derived electrode materials

MOF based templates can be utilized for the manufacture and fabrication of carbon-based hybrid materials. This synthesis method has various benefits that include a wide variety of target materials, prevention of the nanostructures to be damaged during high temperature treatments like calcination, highly porous structures formed as a result of this treatment provide increased sites for the active material to be incorporated, simplicity of the preparation methods, and the materials formed as a result of these procedures can be characterized with various shapes and morphologies like nanowires, nanorods, hollow spheres, etc. (Figure 15)

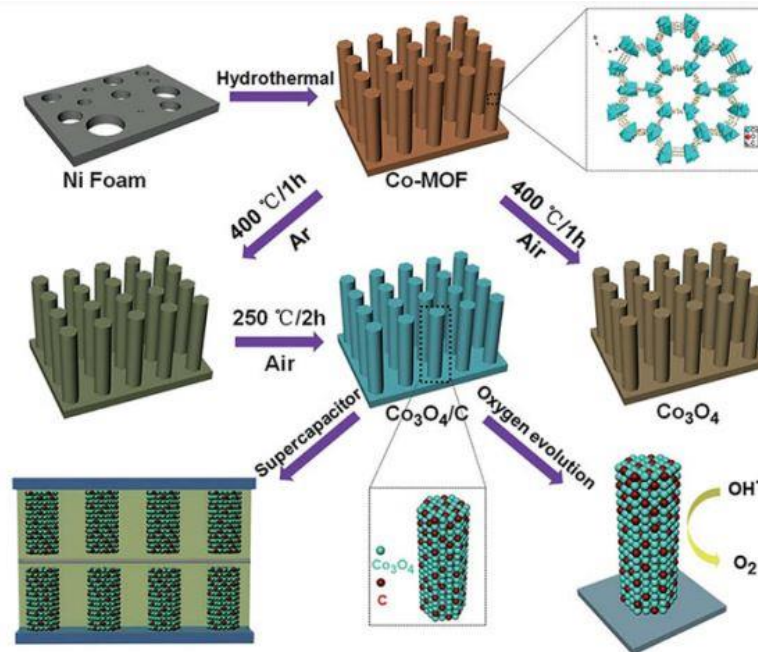


Figure 15 Schematic illustration of $\text{Co}_3\text{O}_4/\text{C}$ nanowire array electrodes

2.2.8 MOF-derived metal oxide/sulfide-based electrodes

Recently, various electrode materials have been fabricated and studied that are made up from transition metal oxides and sulfides. For instance, cobalt oxide (Co_3O_4), ruthenium oxide (RuO_2), manganese oxide (MnO_2), nickel oxide (NiO), and cobalt sulfides (CoS_x) are among some of the materials that demonstrate excellent electrochemical activity which is significantly better than the traditional carbon-based materials[18]–[21]. It is clear from literature that the morphologies and porous structure of electrodes adds significantly to the electrochemical performance of the supercapacitors, hence, the researchers are interested in the careful design and manufacture of metal oxide/sulfide-based composites to increase the electrochemical performance of the supercapacitor devices. Electrochemical supercapacitors are a kind of energy-storage device that can merge the remarkable specific power of a capacitor with the high specific energy of a battery, making it an efficient alternative for a battery.

Metal-Organic Frameworks (MOFs) have demonstrated promising results when used as base materials for electrodes of supercapacitor devices due to large surface area, adjustable pore sizes, and assimilated metal centers based on redox reactions. MOFs can be

incorporated into a supercapacitor in two ways. 1) By directly using them as an electrode for supercapacitors. 2) MOF-derived materials like oxides, nanoporous carbons, and sulfides, etc. can be developed and then used as electrode materials. So far, several MOFs and their derivatives have been developed as supercapacitor electrode material. Several research papers have been published by our research group regarding the MOF derived and zeolitic imidazolate framework (ZIF) derived carbon materials and other derivatives to be used as effective electrocatalysts[22]. Porous carbon materials originated from ZIF are extensively examined as potential materials for electrode of supercapacitors. But apart from the use of metallic or bimetallic MOF-derived materials, MOFs have a major limitation in the use of electrolytes, which decreases cyclic stability during an electrochemical charge/discharge process. Moreover, MOFs can also be coupled with carbon compounds including carbon nanotubes, graphene, and reduced graphene oxide (rGO), etc. to increase the electrochemical performance of a supercapacitor. Wen et al. reported a combination of Ni-MOF/CNT as a composite utilized for various applications in supercapacitor devices which consist of considerable specific energy value of 36.6 Whkg^{-1} . Sarah et al. recently investigated the effects of rGO on a Cu-MOF and described that with the add-on of rGO, the electrochemical activity of Cu-MOF was significantly improved. In short, the addition of carbon-based material in a MOF structure increases the stability of pseudocapacitors in addition to a tremendous increase in the electrochemical performance of the device.

MOF-76 signifies a category of compounds that are synthesized by the reaction of lanthanides and BTC (1,3,5-benzenetricarboxylic acid). Among various applications of MOF-76 include highly efficient uranium sorption, adsorbing dyes, and fluorescence detecting aromatic pollutants. Ce-BTC is one of the MOFs formed from the mentioned combination and it was used as a favorable material for electrode of supercapacitors. Also, Ce-BTC transition metal sulfides and oxides have recently established their usefulness for supercapacitors, due to the large internal surface area that is easily accessible, and it can expedite the diffusion of ions through the extremely porous substructure[23], [24]. Guojin Zeng et. al. synthesized Ce-oxide derived from Ce-BTC, which showed excellent specific capacitance of 779 Fg^{-1} at 1 Ag^{-1} current density, while the retention of capacitance was maintained at 91% at 10000 cycles. Rajendran Ramachandran et. al. reported a specific

capacitance of a huge value of 2221.2 Fg⁻¹ with an amazing specific energy value of 111.05 Whkg⁻¹ at 1 Ag⁻¹ current density for Ce-BTC/GO composite in an electrolyte combination of 3 M KOH+0.2 M K₃Fe(CN)₆.

Apart from metal oxides, metal sulfides are gaining importance regarding being used as electrodes for supercapacitors because of their better electrical conductivity and more flexibility than the corresponding oxides of metals because of the smaller values of electronegativity for sulfur as compared to oxygen[16], [22]. But the limitation of metal sulfide is that they do not show considerable cyclic stability when used directly as the electrodes (Figure 16). To cater to this limitation metal sulfides can be coupled with metal oxides to make a composite that shows good electrical conductivity and better cyclic stability. In this work we synthesized Ce-BTC derived CeO₂/rGO and further converted it into CeO₂/rGO/CeS₂ nanocomposite by a wet chemical route. The as-obtained composite was then characterized by various techniques to find out its crystal structure, morphology, and electrochemical capability.

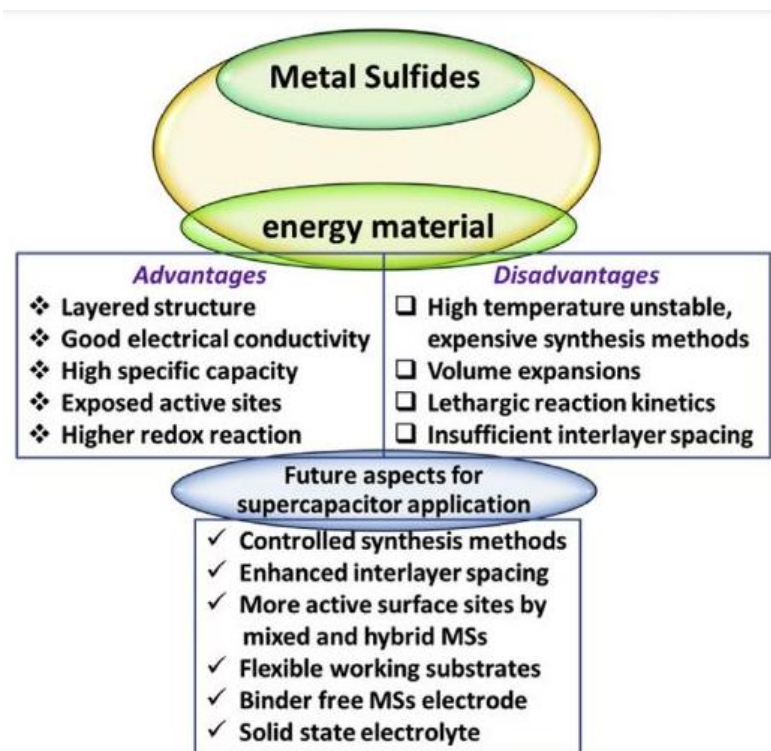


Figure 16 Schematic presentation of challenges and future aspects for metal sulfides as energy material, retrieved from Current Opinion in Electrochemistry

2.3 Summary

This chapter consists of the literature review on the types of electrode materials used for supercapacitor application. In addition, the performance of the electrode materials is also discussed in the chapter. Moreover, this chapter also contains the benefits and shortcomings of various MOF derived materials for the energy storage applications.

References

- [1] Y. Zhou, C. H. Wang, W. Lu, and L. Dai, “Recent Advances in Fiber-Shaped Supercapacitors and Lithium-Ion Batteries,” *Advanced Materials*, vol. 32, no. 5. Wiley-VCH Verlag, p. 1902779, Feb. 01, 2020, doi: 10.1002/adma.201902779.
- [2] J. Xie, P. Yang, Y. Wang, T. Qi, Y. Lei, and C. M. Li, “Puzzles and confusions in supercapacitor and battery: Theory and solutions,” *Journal of Power Sources*, vol. 401. Elsevier B.V., pp. 213–223, Oct. 15, 2018, doi: 10.1016/j.jpowsour.2018.08.090.
- [3] R. Dubey and V. Guruviah, “Review of carbon-based electrode materials for supercapacitor energy storage,” *Ionics*, vol. 25, no. 4. Institute for Ionics, pp. 1419–1445, Apr. 01, 2019, doi: 10.1007/s11581-019-02874-0.
- [4] R. Tamilselvi *et al.*, “Graphene oxide – Based supercapacitors from agricultural wastes: A step to mass production of highly efficient electrodes for electrical transportation systems,” *Renew. Energy*, vol. 151, pp. 731–739, May 2020, doi: 10.1016/j.renene.2019.11.072.
- [5] O. Yanshyna, H. Weissman, and B. Rybtchinski, “Recyclable electrochemical supercapacitors based on carbon nanotubes and organic nanocrystals,” *Nanoscale*, vol. 12, no. 16, pp. 8909–8914, Apr. 2020, doi: 10.1039/d0nr00395f.
- [6] A. Ehsani, H. Mohammad Shiri, E. Kowsari, R. Safari, J. Torabian, and S. Hajghani, “High performance electrochemical pseudocapacitors from ionic liquid assisted electrochemically synthesized p-type conductive polymer,” *J. Colloid Interface Sci.*, vol. 490, pp. 91–96, Mar. 2017, doi: 10.1016/j.jcis.2016.11.024.
- [7] A. Ehsani, A. A. Heidari, and H. M. Shiri, “Electrochemical Pseudocapacitors Based on Ternary Nanocomposite of Conductive Polymer/Graphene/Metal Oxide: An Introduction and Review to it in Recent Studies,” *Chemical Record*, vol. 19, no. 5. John Wiley and Sons Inc., pp. 908–926, May 01, 2019, doi: 10.1002/tcr.201800112.
- [8] F. Wang, S. Xiao, Y. Hou, C. Hu, L. Liu, and Y. Wu, “Electrode materials for aqueous asymmetric supercapacitors,” *RSC Advances*, vol. 3, no. 32. The Royal

- Society of Chemistry, pp. 13059–13084, Aug. 28, 2013, doi: 10.1039/c3ra23466e.
- [9] R. Ahmad, N. Iqbal, M. M. Baig, T. Noor, G. Ali, and I. H. Gul, “ZIF-67 derived nitrogen doped CNTs decorated with sulfur and Ni(OH)₂ as potential electrode material for high-performance supercapacitors,” *Electrochim. Acta*, vol. 364, p. 137147, Dec. 2020, doi: 10.1016/j.electacta.2020.137147.
- [10] Y. Wang, Y. Lei, J. Li, L. Gu, H. Yuan, and D. Xiao, “Synthesis of 3D-Nanonet Hollow Structured Co₃O₄ for High Capacity Supercapacitor,” *ACS Appl. Mater. Interfaces*, vol. 6, no. 9, pp. 6739–6747, May 2014, doi: 10.1021/am500464n.
- [11] N. M. S. Hidayah *et al.*, “Comparison on graphite, graphene oxide and reduced graphene oxide: Synthesis and characterization,” in *AIP Conference Proceedings*, Oct. 2017, vol. 1892, no. 1, p. 150002, doi: 10.1063/1.5005764.
- [12] T. Saravanan *et al.*, “Facile synthesis of graphene-CeO₂ nanocomposites with enhanced electrochemical properties for supercapacitors,” *Dalt. Trans.*, vol. 44, no. 21, pp. 9901–9908, Jun. 2015, doi: 10.1039/c5dt01235j.
- [13] Y. Zhan, Y. Meng, N. Yan, Y. Li, D. Wei, and X. Tao, “Enhancing electrochemical performance of Fe₃O₄/graphene hybrid aerogel with hydrophilic polymer,” *J. Appl. Polym. Sci.*, vol. 134, no. 48, p. 45566, Dec. 2017, doi: 10.1002/app.45566.
- [14] C. Zhang *et al.*, “Hierarchically porous Co₃O₄/C nanowire arrays derived from a metal-organic framework for high performance supercapacitors and the oxygen evolution reaction,” *J. Mater. Chem. A*, vol. 4, no. 42, pp. 16516–16523, Oct. 2016, doi: 10.1039/c6ta06314d.
- [15] R. Ahmad, U. A. Khan, N. Iqbal, and T. Noor, “Zeolitic imidazolate framework (ZIF)-derived porous carbon materials for supercapacitors: An overview,” *RSC Advances*, vol. 10, no. 71, Royal Society of Chemistry, pp. 43733–43750, Nov. 13, 2020, doi: 10.1039/d0ra08560j.
- [16] R. Ahmad, N. Iqbal, and T. Noor, “Development of ZIF-Derived Nanoporous Carbon and Cobalt Sulfide-Based Electrode Material for Supercapacitor,” *Materials (Basel)*, vol. 12, no. 18, p. 2940, Sep. 2019, doi: 10.3390/ma12182940.

- [17] S. Hanif, X. Shi, N. Iqbal, T. Noor, R. Anwar, and A. M. Kannan, "ZIF derived PtNiCo/NC cathode catalyst for proton exchange membrane fuel cell," *Appl. Catal. B Environ.*, vol. 258, p. 117947, Dec. 2019, doi: 10.1016/j.apcatb.2019.117947.
- [18] P. Wen, P. Gong, J. Sun, J. Wang, and S. Yang, "Design and synthesis of Ni-MOF/CNT composites and rGO/carbon nitride composites for an asymmetric supercapacitor with high energy and power density," *J. Mater. Chem. A*, vol. 3, no. 26, pp. 13874–13883, Jul. 2015, doi: 10.1039/c5ta02461g.
- [19] R. Anwar *et al.*, "MOF-Derived CuPt/NC Electrocatalyst for Oxygen Reduction Reaction," *Catalysts*, vol. 10, no. 7, p. 799, Jul. 2020, doi: 10.3390/catal10070799.
- [20] J. Yang, C. Zheng, P. Xiong, Y. Li, and M. Wei, "Zn-doped Ni-MOF material with a high supercapacitive performance," *J. Mater. Chem. A*, vol. 2, no. 44, pp. 19005–19010, Nov. 2014, doi: 10.1039/c4ta04346d.
- [21] M. Saraf, R. Rajak, and S. M. Mobin, "A fascinating multitasking Cu-MOF/rGO hybrid for high performance supercapacitors and highly sensitive and selective electrochemical nitrite sensors," *J. Mater. Chem. A*, vol. 4, no. 42, pp. 16432–16445, Oct. 2016, doi: 10.1039/c6ta06470a.
- [22] C. S. Lee, J. M. Lim, J. T. Park, and J. H. Kim, "Direct growth of highly organized, 2D ultra-thin nano-accordion Ni-MOF@NiS₂@C core-shell for high performance energy storage device," *Chem. Eng. J.*, vol. 406, p. 126810, Feb. 2021, doi: 10.1016/j.cej.2020.126810.
- [23] X. Lian and B. Yan, "A lanthanide metal-organic framework (MOF-76) for adsorbing dyes and fluorescence detecting aromatic pollutants," *RSC Adv.*, vol. 6, no. 14, pp. 11570–11576, Jan. 2016, doi: 10.1039/c5ra23681a.
- [24] P. F. Santos and P. P. Luz, "Synthesis of a CE-based MOF-76 with high yield: A study of reaction parameters based on a factorial design," *J. Braz. Chem. Soc.*, vol. 31, no. 3, pp. 566–573, Mar. 2020, doi: 10.21577/0103-5053.20190218.

Chapter 3 Experimentation and Characterization Methods

3.1 Synthesis Methods

Two most important categories of inorganic synthesis are the hydrothermal synthesis method and the solvothermal synthesis method (Figure 17). In addition to the synthesis of the traditional materials and composites, the hydrothermal and solvothermal methods also cover other interdisciplinary branches of science like waste treatment etc[1]. This chapter sheds some light on the synthesis category of the hydrothermal and solvothermal methods.

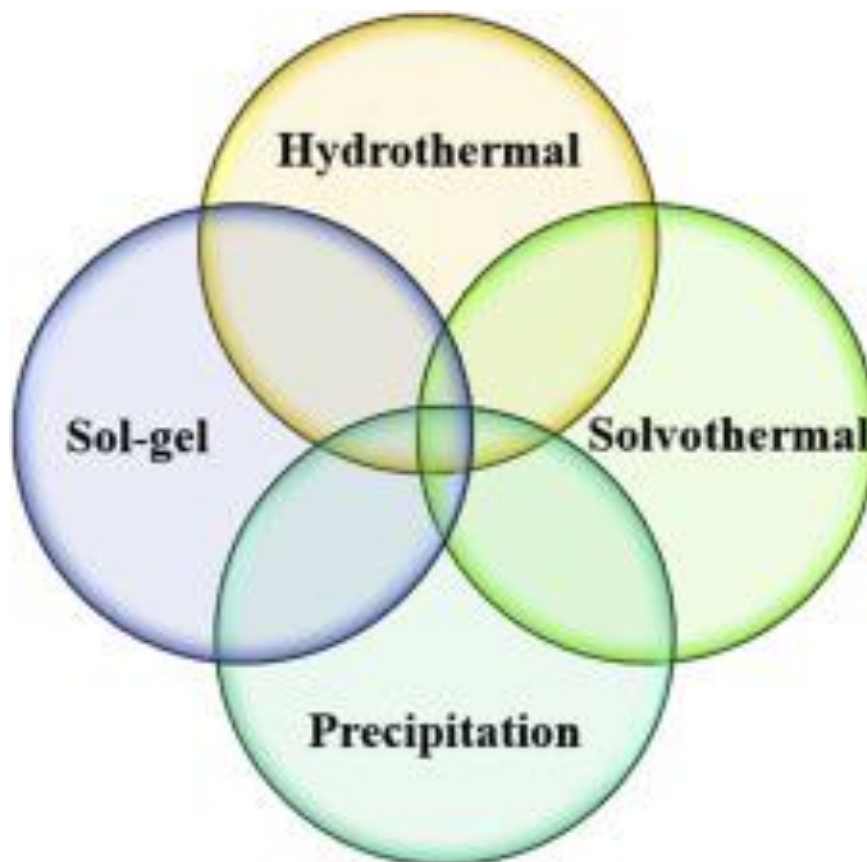


Figure 17 Types of Synthesis techniques

3.1.1 Solvothermal Synthesis

A wide variety of materials can be prepared by the solvothermal method, for instance, metal composites, semiconductors, polymers, and ceramics, etc. the basic process includes the utilization of a certain solvent under varying pressure and temperatures ranges to facilitate the interaction of the precursors in a synthesis[2], [3]. This technique can be utilized to synthesize complex materials that are thermally stable and can not be prepared by the conventional synthesis methods. In the recent literature, researchers have focused on the synthesis of nanocrystals by the solvothermal method in addition to other morphologies.

3.1.2 Hydrothermal Method

This method is used to synthesize materials that require special conditions for the synthesis. Also, this method helps control the structure, morphology, and other properties of the material. Metal Oxides, halides, composites that require specific temperature as well as pressure are usually synthesized by this method. The nanoparticles obtained by this method have characteristic properties[4]–[6]. This method normally requires the use of an autoclave a device in which temperature and pressure can be simultaneously controlled (Figure 18). The benefit of utilizing this technique involves the ability to manufacture a large number of nanoparticles that have an optimized morphology, material composition and suitable particle size in addition to the improved surface chemistry.

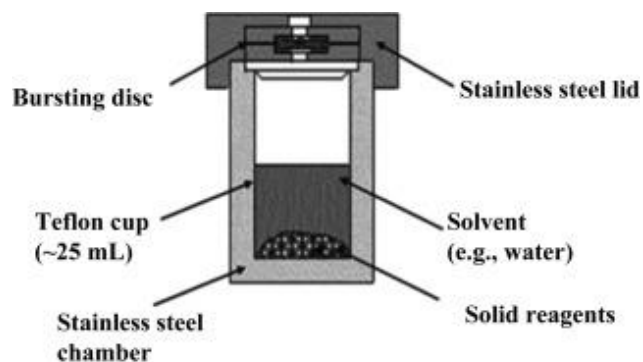


Figure 18 Autoclave used for the hydrothermal synthesis technique.

3.2 Characterization Techniques

3.2.1 X-ray Diffraction

This is one of the most important and common material characterization technique which provides information about the morphology, components, and crystallite size of the material. It uses X-ray radiations which pass through the material at an angle to the source. The diffraction angle is calculated, and the intensity is recorded[7]. At an angle how many radiations deflect form a specific plane on material gives information regarding its structure morphology (Figure 19).

This technique relies on the distinct nature of X-rays, i.e., double wave/particle nature, in order to confirm the crystalline structure of the materials. In the mechanism of this technique, a beam of monochromatic X-rays is applied on the material under consideration[8]. When the incident beam comes in contact with the material, the atoms of

that material scatter the X-rays which undertake both constructive and destructive interference. Bragg's Law describes the diffraction of X-rays as below:

$$n\lambda = 2d\sin\theta \quad (1)$$

The direction of the diffractions is confirmed by the shape and size of the unit cell of the material, while the intensity of the diffracted X-rays depends on the arrangement of atoms in the material. As most of the materials are not single crystals in nature, so, the X-ray beam will consider all of the interatomic sites and all the possible diffraction peaks will be detected at a certain angle.

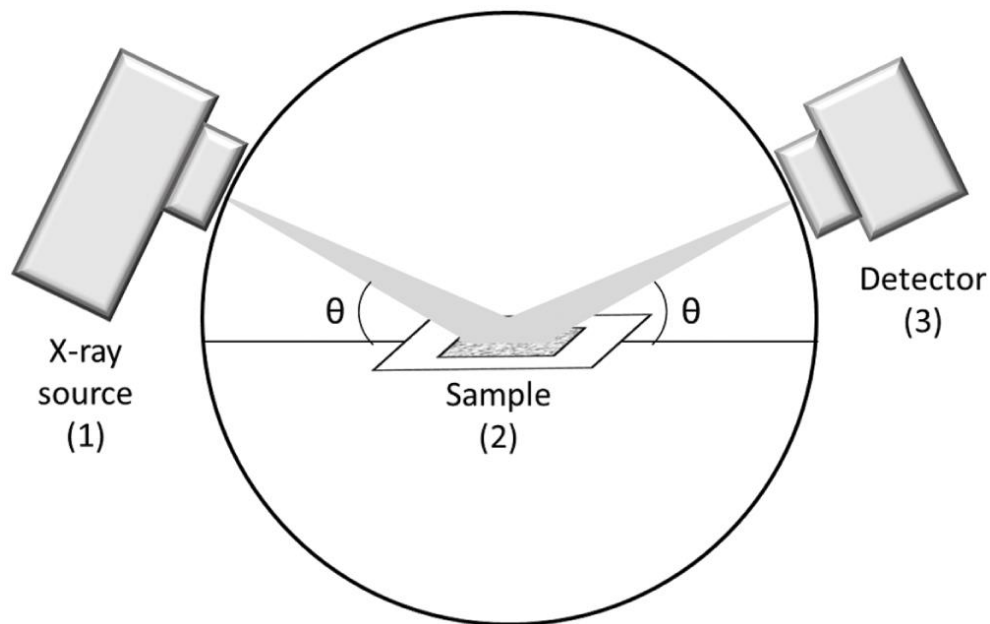


Figure 19 Schematic of XRD Process

3.2.2 Scanning Electron Microscopy

The scanning electron microscope (SEM) utilizes a focused beam of high-energy electrons in order to generate a wide range of signals at the solid specimen surface. The high energy electrons penetrate through the material and escape through the other end as shown in Figure 20. Information about the morphology, materials orientation, and crystal structure is determined by the signals that are derived from the interaction of electrons and the sample[9], [10]. The SEM is proficient of carrying out analyses of specific area or locations

on the sample. Its design and function are quite like the EPMA and significant connection in abilities exists amongst the two devices.

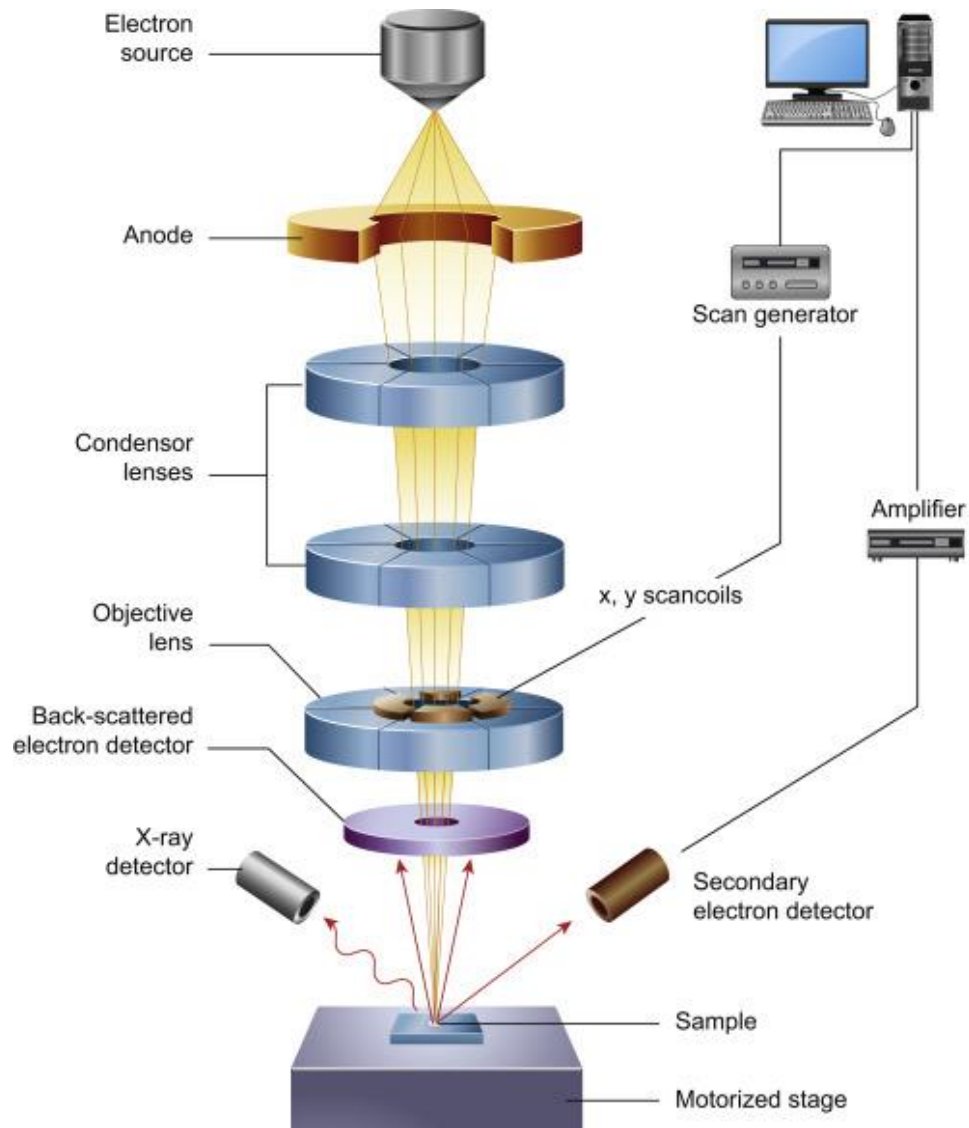


Figure 20 Schematic drawing of the electron and x-ray optics of a combined SEM-EPMA

3.2.3 Energy Dispersive Spectroscopy (EDS)

EDS is an elemental analysis method used to quantify the number of individual elements present in a nanoparticle. This technique gives the number of substances at a particular point but does not give the overall quantity of each element. It is usually combined with

SEM or TEM to get a nanoscale image of particles through them, and EDS performs the analysis of that nanostructure.

In the early 1970s energy dispersive spectroscopy became one commercial product, and rapidly crossed WDS in popularity. The overall structure of the EDS is very simple because of no moving parts like rotation detector in WDS[11]. The detector gathers the signals of X-rays from all range of elements in a sample at the once instead of amassing signals from X-rays one by one which make the EDS systems relatively fast (Figure 21). The usual resolution of energy dispersion is about 150–200 eV, which is lower than the resolution of WDS[12]. The lightest element that can be identified is O ($Z=8$), not C ($Z=6$). But major benefits like low cost and fast analysis make these disadvantages insignificant.

EDS spectrum is a graph between intensity of X-rays and the corresponding energies. Both light and heavy elements can be seen in a spectrum with a range of 0.1 to about 10–20 keV.

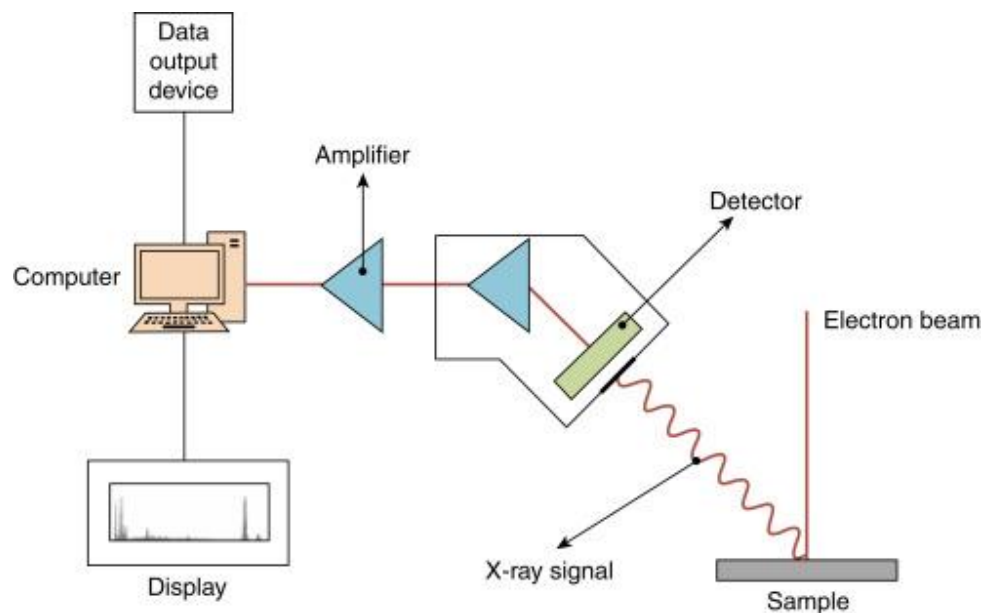


Figure 21 Illustration of EDS

3.2.4 Thermo-Gravimetric Analysis

Thermogravimetric analysis (TGA) determines weight losses in a material with a change in temperature in a controlled atmosphere. The major applications of this characterization

technique are the measurement of thermal stability, volatile content, moisture, organic linker in a sample, and the percent composition of components in a compound.

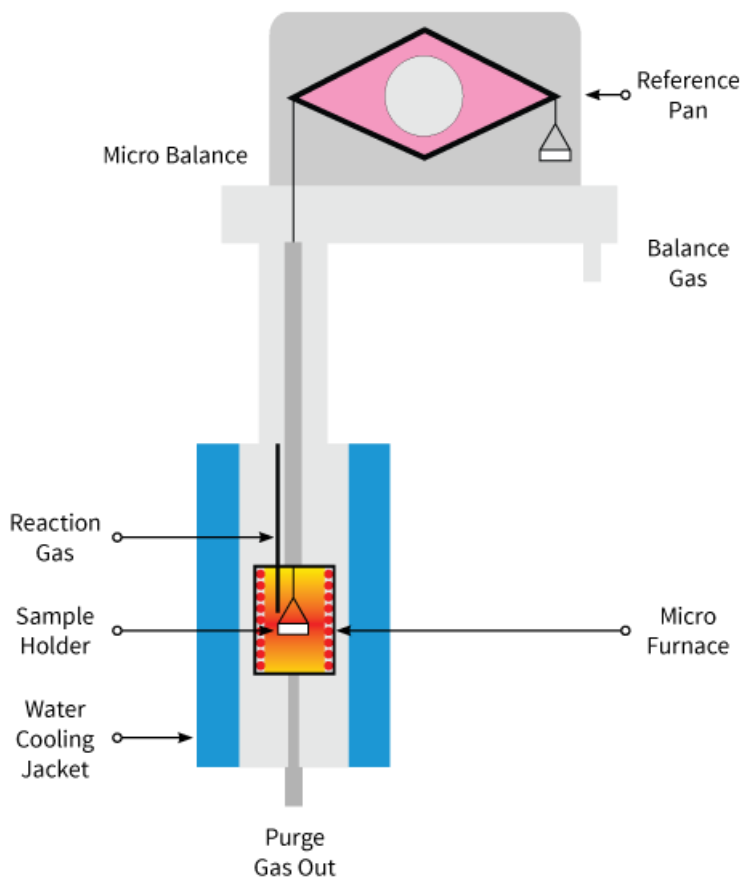


Figure 22 Illustration of TGA

The principle is that the temperature is gradually increased from zero to the required final temperature in a specific gas atmosphere which maybe Ar, air or some other gas. Now when temperature increases the contents in the sample start to evaporate. Moisture is usually the first content that removes from the sample so a change in mass of sample occurs[13]. This mass is measured on the weight balance continuously during the process which is placed outside the furnace (Figure 22). After moisture other volatile contents like organic residue start to escape. The stability of the sample can be defined as the temperature at which the material starts to decompose which is the main point in the curve. After that the line drops sharply causing a major loss in material. This point is called the

decomposition temperature and determines the stability of material[14]. The weight of the material is mapped against temperature or time to demonstrate the thermal changes in the sample, for instance, the loss of solvent, loss of water of hydration, and the decomposition of the material. At the end of the process, the final mass residue is noted, and the total mass loss is calculated.

3.2.5 Fourier Transform Infrared Spectroscopy

Fourier transform infrared spectroscopy is the preferred technique for infrared spectroscopy. When IR radiation passes through a material, some of the incident radiation gets absorbed in the material while the rest is transmitted (Figure 23). The detector at the other end detects the transmitted radiation and sets out a signal that is basically represented in the form of a spectrum and it demonstrates the molecular nature of the material[15].

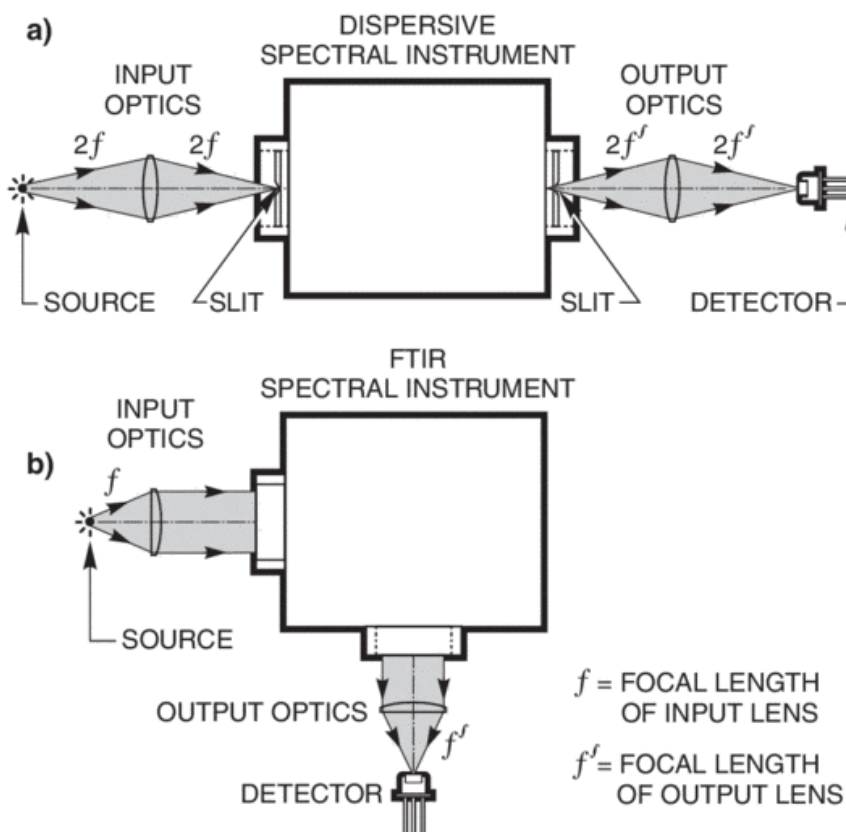


Figure 23 Schematic diagram of FTIR.

3.3 Electrochemical Testing

3.3.1 Suspension formation

For every electrochemical reaction being performed on the glassy carbon electrode, the catalyst ink is always formed to deposit the catalyst onto the surface of the glassy carbon. Ink is formed following different approaches and ratios depending upon the type of catalyst and its solubility. Water, ethanol is used as an aqueous solvent for homogenization while Nafion works as a binding agent. The components in required amount are mixed in a small vial and sonicated for about 6-8 hrs before usage. Ink is usually deposited by spray coating or dip coating technique on the substrate.

3.4 Electrochemical Workstation Techniques

After the formation of the catalyst suspension, its electrochemical testing is performed. For the electrocatalytic activity of metal sulfide composite, the following electrochemical techniques were performed on Electrochemical Workstation:

3.4.1 Cyclic Voltammetry

This electrochemical technique involves the running of the workstation through a complete cycle. The potential range was input into the software which is applied across the two electrodes. Scan rate, sample interval, sensitivity was given for each run along with number of segments[16]. Two segments make one complete cycle. The cyclic voltammetry gives information of the current changing with voltage as shown in Figure 24. When CV is performed the current passes through external circuit and electrons start to flow from anode to cathode[17]. The number of electrons that cause reduction give a particular current signal. For performing CV the electrochemical cell is used which has two compartments[18]. The cell is first purged with Ar inert gas to remove any oxygen from cathode compartment. After that CO₂ is purged and CV is performed. The catalyst is coated on the glassy carbon electrode. CV is sometimes used to check the stability of materials by performing large segments in single run.

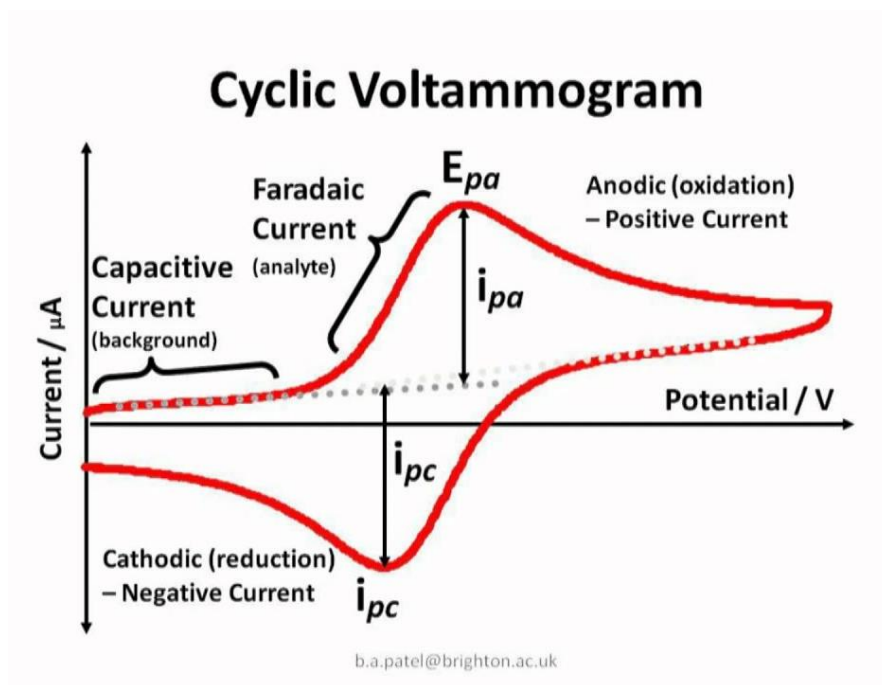


Figure 24 Cyclic voltammogram

3.4.2 Chronopotentiometry

Chronopotentiometry is an electrochemical analysis method where the electrodes are subjected to a constant flow of current in order to cause a constant reduction of the electroactive material (Figure 25). This method is differentiated from constant-current coulometric analysis and coulometric titrimetry¹ because in this technique the applied current appears to be significantly large so that the efficiency of current required for the reduction of the material is reduced below 100% within a few seconds.

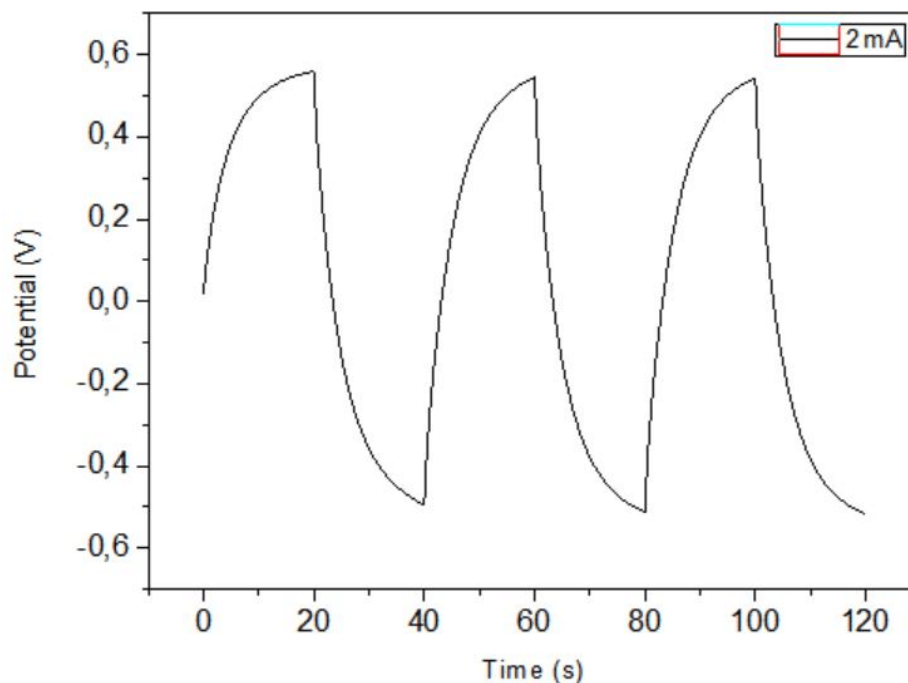


Figure 25 Chronopotentiometry, Galvanostatic charge/discharge curve.

3.4.3 Electrochemical Impedance Spectroscopy

This technique of electrochemical workstation allows us to measure the resistivity of our system. This includes resistance of electrolyte, ohmic loss and or activation losses. (Figure 26)

Electrical resistance is the measure of the of a circuit element that resists current flow.

$$R = \frac{E}{I} \quad (2)$$

According to Ohm's law, R is the resistance which is defined as the ratio of voltage (E), and current (I). This known law use is limited to only one circuit element, the ideal resistor.

An ideal resistor has several simplifying properties:

- Ohm's Law is followed at every range of current and voltage.
- Resistance is not dependent on the frequency.
- The voltage passing through a resistor and the AC current are in a single phase.

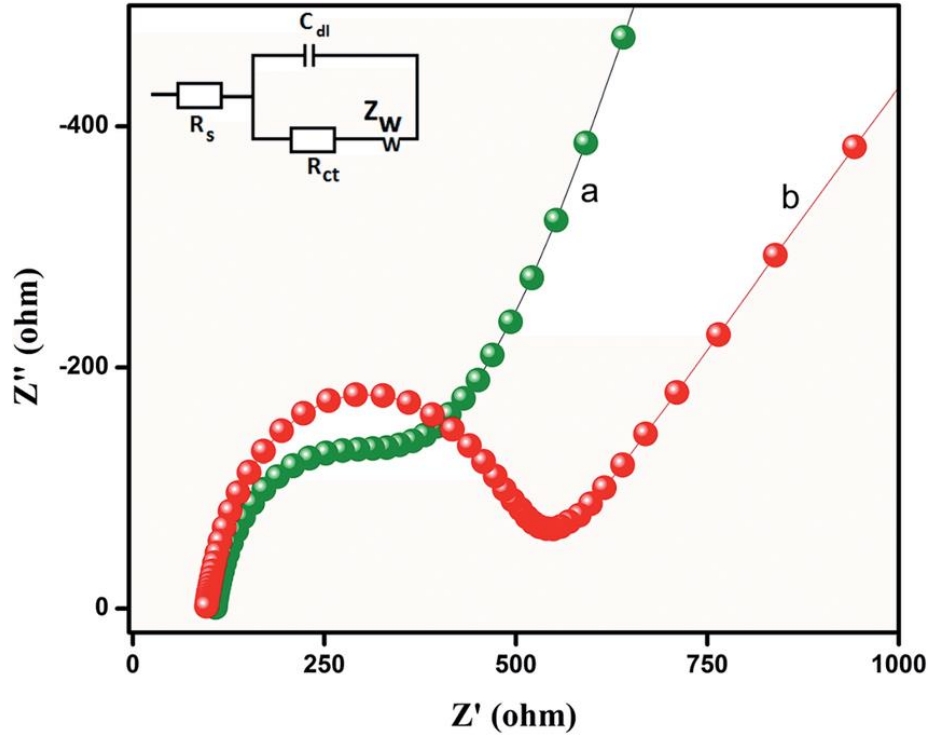


Figure 26 Electrochemical Impedance Spectroscopy.

3.5 Electrochemical parameters

The determination of the energy density and power density is very important to evaluate the efficiency of a supercapacitor for real-life applications. Cyclic voltammetry (CV) and chronopotentiometry are the techniques that can confirm the energy and power densities by using the following equations:

The specific capacitance (C , Fg^{-1}) can be determined using cyclic voltammetry:

$$C_m = \frac{\int IdV}{2mv\Delta V} \quad (3)$$

Here, $\int IdV$ is the integral area of the CV curves, m represents the mass, n represents the scan rate used to perform the analysis, and the voltage window of the process is represented by V .

$$E = \frac{1}{2} \frac{C_m (\Delta V)^2}{3.6} \quad (4)$$

Here, E is the symbol for energy density. The specific power (W/kg) defines how rapidly a device is able to deliver energy under a constant current density to external loads. The maximum specific power is calculated as:

$$P = \frac{E}{\Delta t} \times 3600 \quad (5)$$

Here, P represents the maximum power that can be achieved by a supercapacitor.

Summary

This chapter initially discusses different chemical synthesis methods like solvothermal and hydrothermal method. After that material characterization techniques have been studied i.e., XRD, SEM, EDS, TGA, and FTIR. Main principle of these techniques has been noted down along with diagrams. After that the whole electrochemical testing process implemented was explained including ink formation, ink deposition on substrate and electrochemical performance determination using various techniques like CV, CP, and EIS with a three-electrode system.

References

- [1] M. Lian, X. Wu, Q. Wang, W. Zhang, and Y. Wang, “Hydrothermal synthesis of Polypyrrole/MoS₂ intercalation composites for supercapacitor electrodes,” *Ceram. Int.*, vol. 43, no. 13, pp. 9877–9883, Sep. 2017, doi: 10.1016/j.ceramint.2017.04.171.
- [2] “Solvothermal Synthesis - an overview | ScienceDirect Topics.” <https://www.sciencedirect.com/topics/materials-science/solvothermal-synthesis> (accessed Mar. 07, 2021).
- [3] R. Ramachandran, M. Saranya, P. Kollu, B. P. C. Raghupathy, S. Kwan Jeong, and A. Nirmala Grace, “Solvothermal synthesis of Zinc sulfide decorated Graphene (ZnS/G) nanocomposites for novel Supercapacitor electrodes,” *Electrochim. Acta*, vol. 178, pp. 647–657, 2015, doi: 10.1016/j.electacta.2015.08.010.
- [4] Y. G. Zhu *et al.*, “Application of redox targeting chemistry in electrochromism View project Redox targeting View project,” doi: 10.1039/c3ra42091d.
- [5] Y. G. Zhu *et al.*, “Design and synthesis of NiO nanoflakes/graphene nanocomposite as high performance electrodes of pseudocapacitor,” *RSC Adv.*, vol. 3, no. 42, pp. 19409–19415, Nov. 2013, doi: 10.1039/c3ra42091d.
- [6] T. Noor, M. Ammad, N. Zaman, N. Iqbal, L. Yaqoob, and H. Nasir, “A Highly Efficient and Stable Copper BTC Metal Organic Framework Derived Electrocatalyst for Oxidation of Methanol in DMFC Application,” *Catal. Letters*, vol. 149, no. 12, pp. 3312–3327, Dec. 2019, doi: 10.1007/s10562-019-02904-6.
- [7] D. K. Unruh and T. Z. Forbes, “X-ray Diffraction Techniques,” in *Analytical Geomicrobiology*, Cambridge University Press, 2019, pp. 215–237.
- [8] S. I. AL-Saedi, A. J. Haider, A. N. Naje, and N. Bassil, “Improvement of Li-ion batteries energy storage by graphene additive,” in *Energy Reports*, Feb. 2019, vol. 6, pp. 64–71, doi: 10.1016/j.egy.2019.10.019.
- [9] M. Aghazadeh, “Synthesis, characterization, and study of the supercapacitive

- performance of NiO nanoplates prepared by the cathodic electrochemical deposition-heat treatment (CED-HT) method,” *J. Mater. Sci. Mater. Electron.*, vol. 28, no. 3, pp. 3108–3117, Feb. 2017, doi: 10.1007/s10854-016-5899-x.
- [10] M. M. Peng, M. Ganesh, R. Vinodh, M. Palanichamy, and H. T. Jang, “Solvent free oxidation of ethylbenzene over Ce-BTC MOF,” *Arab. J. Chem.*, vol. 12, no. 7, pp. 1358–1364, Nov. 2019, doi: 10.1016/j.arabjc.2014.11.024.
- [11] Z. M. Wang, J. Wagner, S. Ghosal, G. Bedi, and S. Wall, “SEM/EDS and optical microscopy analyses of microplastics in ocean trawl and fish guts,” *Sci. Total Environ.*, vol. 603–604, pp. 616–626, Dec. 2017, doi: 10.1016/j.scitotenv.2017.06.047.
- [12] F. Georget, W. Wilson, and K. L. Scrivener, “edxia: Microstructure characterisation from quantified SEM-EDS hypermaps,” *Cem. Concr. Res.*, vol. 141, p. 106327, Mar. 2021, doi: 10.1016/j.cemconres.2020.106327.
- [13] Z. Boubacar Laougé and H. Merdun, “Pyrolysis and combustion kinetics of *Sida cordifolia* L. using thermogravimetric analysis,” *Bioresour. Technol.*, vol. 299, p. 122602, Mar. 2020, doi: 10.1016/j.biortech.2019.122602.
- [14] N. Saadatkah *et al.*, “Experimental methods in chemical engineering: Thermogravimetric analysis—TGA,” *Canadian Journal of Chemical Engineering*, vol. 98, no. 1. Wiley-Liss Inc., pp. 34–43, Jan. 01, 2020, doi: 10.1002/cjce.23673.
- [15] N. S. Marinkovic, M. Li, and R. R. Adzic, “Pt-Based Catalysts for Electrochemical Oxidation of Ethanol,” Springer, Cham, 2020, pp. 1–39.
- [16] C. Costentin, J. Fortage, and M. N. Collomb, “Electrophotocatalysis: Cyclic Voltammetry as an Analytical Tool,” *J. Phys. Chem. Lett.*, vol. 11, no. 15, pp. 6097–6104, Aug. 2020, doi: 10.1021/acs.jpcllett.0c01662.
- [17] B. J. Venton and Q. Cao, “Fundamentals of fast-scan cyclic voltammetry for dopamine detection,” *Analyst*, vol. 145, no. 4. Royal Society of Chemistry, pp. 1158–1168, Feb. 21, 2020, doi: 10.1039/c9an01586h.

Chapter 4 Methodology and Experimentation

4.1 Materials

The precursors utilized were Cerium-Nitrate-hexahydrate ($\text{Ce}(\text{NO}_3)_3 \cdot 6\text{H}_2\text{O}$), and Trimesic acid (1,3,5- H_3BTC) was used as the linker. The solvent was an Ethanol and D.I Water solution in the ratio (3:1). Sodium sulfide was used for sulfidation while the improved hummers method was utilized to synthesize graphene oxide.

4.2 Synthesis of Ce-BTC

The following synthesis method was used for Ce-BTC; A 50 mL solution was made by using a combination of 2mM 1,3,5-benzenetricarboxylic acid, and 8mM Cerium-Nitrate-Hexahydrate in DMF, which was then mixed for 30 min at 400 rpm. The as-prepared solution was subjected to thermal treatment in a Teflon-lined 100 mL autoclave made of steel, and subjected to 120 °C temperature for 24 hrs. It was then cooled naturally at the standard room temperature[1]–[3]. The obtained samples were extracted by the separation technique known as centrifugation followed by repeated washing with DMF and ethanol. Finally, the acquired powder was subjected to vacuum drying 80 °C for 14 hrs. (Figure 27)

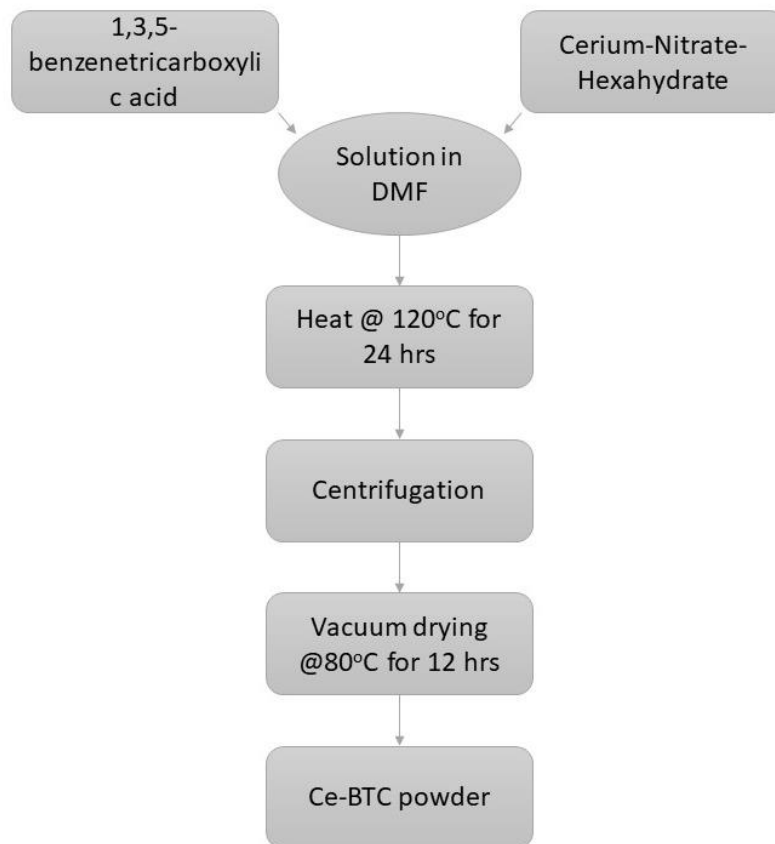


Figure 27 Synthesis scheme for Ce-BTC

4.3 Preparation of CeO₂/rGO composite

Ce-BTC powder was mixed with graphene oxide powder in ethanol solution and sonicated for 1hr. The resultant composite was extracted by centrifugation and dried at 80 °C for 12hrs. It was then subjected to thermal treatment at 350 °C for 90 minutes in a tube furnace, and the temperature was gradually amplified to 600 °C at the ramp of 4 °C min⁻¹. It was then pyrolyzed for 3 hrs at 600 °C under an inert (Hydrogen, Argon) environment and the temperature was spontaneously brought down to room temperature[4], [4], [5]. (Figure 28)

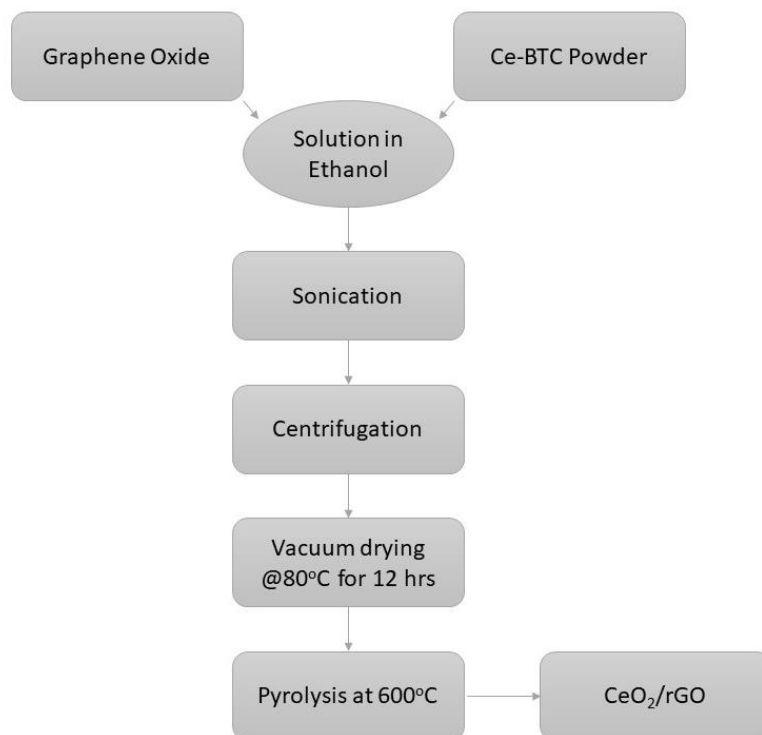


Figure 28 Synthesis scheme for CeO₂/rGO composite

4.4 Ce-BTC derived CeO₂/rGO/CeS₂ composite

The as-obtained CeO₂/rGO composite obtained from pyrolysis was treated for 6 hrs with 0.5 M sulfuric acid, washed, and finally dried at 80 °C for 14 hrs in a vacuum. The dried powder was then added in 30 mL DI water and thoroughly stirred at room temperature and pressure[4]. A separate solution was prepared with 0.1 M Sodium Sulfide in 30 mL water. The two prepared solutions were mixed with a magnetic and stirred at 400 rpm under standard room temperature and pressure. The as-prepared solution was then heated at 180 °C for 14 hrs under high pressure in a 100 mL autoclave with Teflon lining inside, washed multiple times with water in a centrifuge, and subjected to vacuum drying at 70 °C for 12 hrs. (Figure 29)

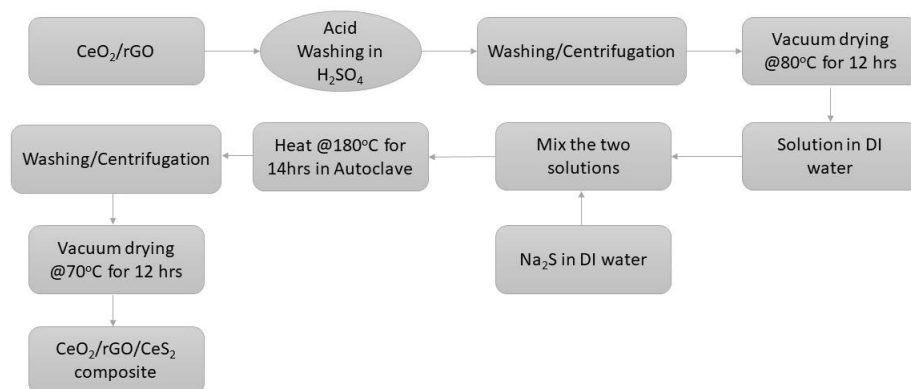


Figure 29 Synthesis scheme for CeO₂/rGO/CeS₂ composite

4.5 Material Characterization

The prepared materials were subject to imaging from a scanning electron microscope (SEM) (VEGA3,51–ADD0007) (Tescan, Brno, Czech Republic) in order to find out the morphology of the samples, while the chemical composition was presented by EDS. X-ray diffraction method (D8 Advance, CuKR, $\lambda = 1.54 \text{ \AA}$) (Bruker, Karlsruhe, Germany) was implemented to demonstrate the crystalline assembly of the prepared samples, while the thermo-gravimetric analysis (TGA) was done with a DTG–60H (Shimadzu, Kyoto, Japan) equipment in a wide array of temperature of up to 900. The elemental analysis was done by the XPS technique while the nanostructure was further analyzed by TEM analysis. In order to find the existing functional groups in the material sample, FTIR technique was employed on the FTIR Agilent carry 630 (Agilent USA).

4.6 Electrochemical Testing

The electrochemical performance of the prepared electrode was tested and determined by using a three-electrode system, including a working electrode, a reference electrode, and a counter electrode. The electrolyte chosen for the procedure was 3M KOH. The testing was done with three distinct electrochemical techniques including the cyclic voltammetry, chronopotentiometry, and electrochemical impedance spectroscopy to find out the specific capacitance, energy density, power density, and cyclic stability of the prepared electrode material over a range of voltage and current.

Summary

This chapter includes the total experimentation that was involved in the research process. The synthesis process of ZIF-8 and Cu-doped ZIF-8 materials and their characterization techniques used were thoroughly demonstrated in the chapter. Finally, the electrochemical testing techniques which were used on electrochemical workstation and the whole process of ink formation and cell setup is explained for the electrocatalytic CO₂ reduction process.

References

- [1] M. M. Peng, M. Ganesh, R. Vinodh, M. Palanichamy, and H. T. Jang, "Solvent free oxidation of ethylbenzene over Ce-BTC MOF," *Arab. J. Chem.*, vol. 12, no. 7, pp. 1358–1364, Nov. 2019, doi: 10.1016/j.arabjc.2014.11.024.
- [2] X. Zhang *et al.*, "A strawsheave-like metal organic framework Ce-BTC derivative containing high specific surface area for improving the catalytic activity of CO oxidation reaction," *Microporous Mesoporous Mater.*, vol. 259, pp. 211–219, Mar. 2018, doi: 10.1016/j.micromeso.2017.10.019.
- [3] P. F. Santos and P. P. Luz, "Synthesis of a CE-based MOF-76 with high yield: A study of reaction parameters based on a factorial design," *J. Braz. Chem. Soc.*, vol. 31, no. 3, pp. 566–573, Mar. 2020, doi: 10.21577/0103-5053.20190218.
- [4] N. Bibi, Y. Xia, S. Ahmed, Y. Zhu, S. Zhang, and A. Iqbal, "Highly stable mesoporous CeO₂/CeS₂ nanocomposite as electrode material with improved supercapacitor electrochemical performance," *Ceram. Int.*, vol. 44, no. 18, pp. 22262–22270, Dec. 2018, doi: 10.1016/j.ceramint.2018.08.348.
- [5] T. Saravanan *et al.*, "Facile synthesis of graphene-CeO₂ nanocomposites with enhanced electrochemical properties for supercapacitors," *Dalt. Trans.*, vol. 44, no. 21, pp. 9901–9908, Jun. 2015, doi: 10.1039/c5dt01235j.

Chapter 5 Results and Discussion

5.1 Material Characterization

5.1.1 XRD

X-ray Diffraction Method was utilized to confirm the crystalline assembly of Ce-BTC before pyrolysis, CeO₂/rGO composite after pyrolysis, and the CeO₂/rGO/CeS₂ composite after sulfidation. Figure 30(a) represents the XRD pattern for Ce-BTC and the peak positions at 8.4°, 10.5°, 18.05° (2θ) determine the good crystallinity of Ce-BTC, which is aligned with the results of the literature[1]. Figure 30(b) represents the XRD peaks obtained after the pyrolysis of Ce-BTC. The peaks appearing at 28.4°, 32.9°, 47.3°, and 56.2° (2θ) confirm the formation of CeO₂/rGO which is in accordance with the JCPDS card number (81-0792).

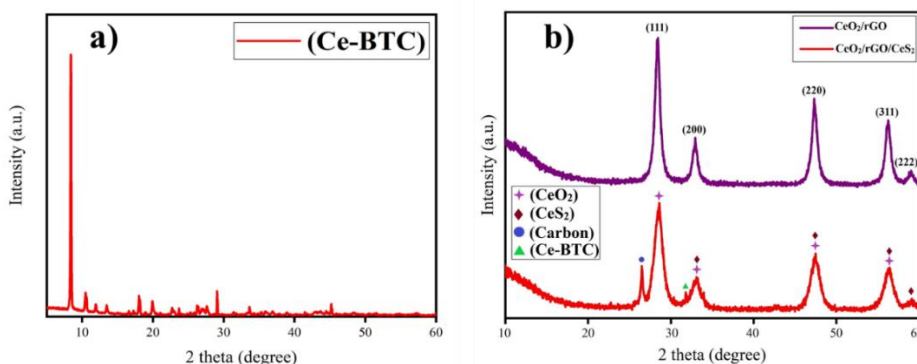


Figure 30 Represents the XRD pattern of, a) Ce-BTC, b) CeO₂/rGO composite and CeO₂/rGO/CeS₂ composite.

It is clear from the pattern that the influence of graphene oxide is not significant as only a small quantity was added. According to the diffraction peak at (220), the size of the crystallite for CeO₂/rGO was calculated to be 11.467nm using the Sherer equation which revealed that it consists of nanocrystal units. The XRD pattern was determined for the CeO₂/rGO/CeS₂ composite, which was consistent with the literature. The wide diffraction peak at 26.4° (2θ) represents graphite carbon. The appearance of the characteristic peaks of CeO₂, CeS₂, and rGO verifies the formation of the nanocomposite[2]. No extra peaks were detected, which verifies the formation of pure CeO₂/rGO/CeS₂ nanocomposite.

5.1.2 Scanning Electron Microscope-SEM

SEM measurements demonstrated the morphology of the prepared materials, as shown in Figure 31(a, b, c). Metal-Organic Framework Ce-BTC showed pillar-like rods which is consistent with the literature[3], [4]. The particle size for the Ce-BTC pillar-like rods was found to be 37.47nm which confirms the mesoporous structure of Ce-BTC, hence more electrochemical activity. After pyrolysis at 600°C, the morphology was changed to cubic structures on a BTC framework, while nanoparticles of reduced graphene oxide were dispersed over the cubic morphology of cerium oxide, holding it together. Morphology features of CeO₂/rGO/CeS₂ composite are displayed in Figure 31(c).

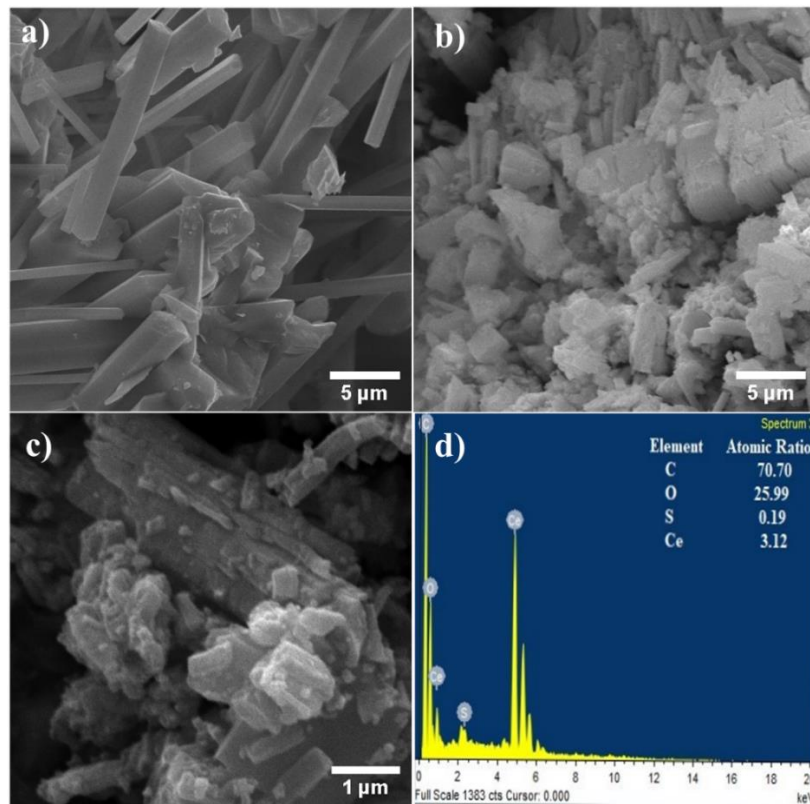


Figure 31 SEM images of, a) Pillar like rods of Ce-BTC, b) Cubic CeO₂/rGO, c) Irregular nanorods of CeO₂/rGO/CeS₂ composite, and d) EDX measurements for C:O:S:Ce

The image shows the formation of Irregular nanorods, grown on the BTC framework. Several cubic structures can be seen in the image that confirms the existence of CeO₂ in the composite and the rGO nanoparticles can be seen dispersed and holding the crystal structures together over the BTC framework[5]. The atomic percentage of C, O, S, and Ce

was established by the energy-dispersive X-ray spectroscopy (EDS) measurements, Figure 31(d). Table 1 EDX analysis of CeO₂/rGO/CeS₂ nanocomposite represents the atomic ratios and weight% of the elements present in the CeO₂/rGO/CeS₂.

Table 1 EDX analysis of CeO₂/rGO/CeS₂ nanocomposite

| Element | Weight % | Atomic Ratio |
|---------|----------|--------------|
| C | 49.70 | 70.70 |
| O | 24.33 | 25.99 |
| S | 0.35 | 0.19 |
| Ce | 25.62 | 3.12 |

5.1.3 Transmission Electron Microscopy-TEM

TEM analysis was carried out in order to figure out the analytical characterization of the nanoparticles of the nanocomposite. In the case of CeO₂/rGO/CeS₂ nanocomposite, the TEM image demonstrates the small size of the particles in addition to the uniform distribution across the particle structure. Figure 32 represents the uniform distribution of the CeO₂/rGO/CeS₂ nanoparticles over the BTC framework[6]. The dark spot in the center represents the sulfide and oxide particles while rGO can be seen distributed along the boundary of the composite.

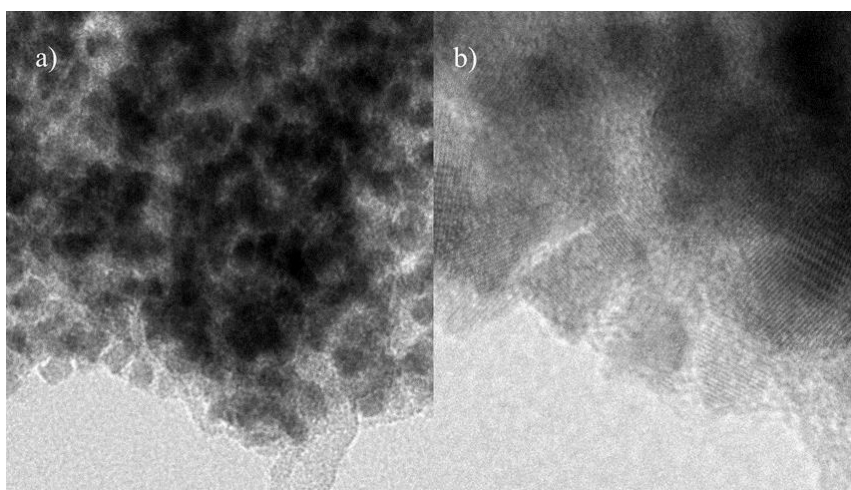


Figure 32(a,b) TEM image for CeO₂/rGO/CeS₂ nanocomposite at 20 nm and 10 nm respectively

5.1.4 X-ray photoelectron spectroscopy-XPS

XPS analysis was done in order to confirm the elemental composition of the CeO₂/rGO/CeS₂ nanocomposite. Figure 33(a) represents the detailed survey analysis of the CeO₂/rGO/CeS₂ composite with the help of XPS measurements. The figure represents the presence of four elements including Carbon (C1s), Cerium (Ce3d), Oxygen (O1s), and Sulfur (S2p) which demonstrates the elemental composition of CeO₂/rGO/CeS₂ nanocomposite. The spectrum for Ce3d represented two characteristic peaks at 882.09, and 901.2 confirming the existence of Ce⁺³ and Ce⁺⁴ oxidation states. The spectrum for S2p represented two peaks at 169.03 and 163.4 confirming the existence of sulfide. Similarly, O1s represented two distinct peaks at 529.2 and 531.8 demonstrating the existence of oxides. Finally, C1s represented one specific peak at 284.15 confirming the existence of carbon or rGO.

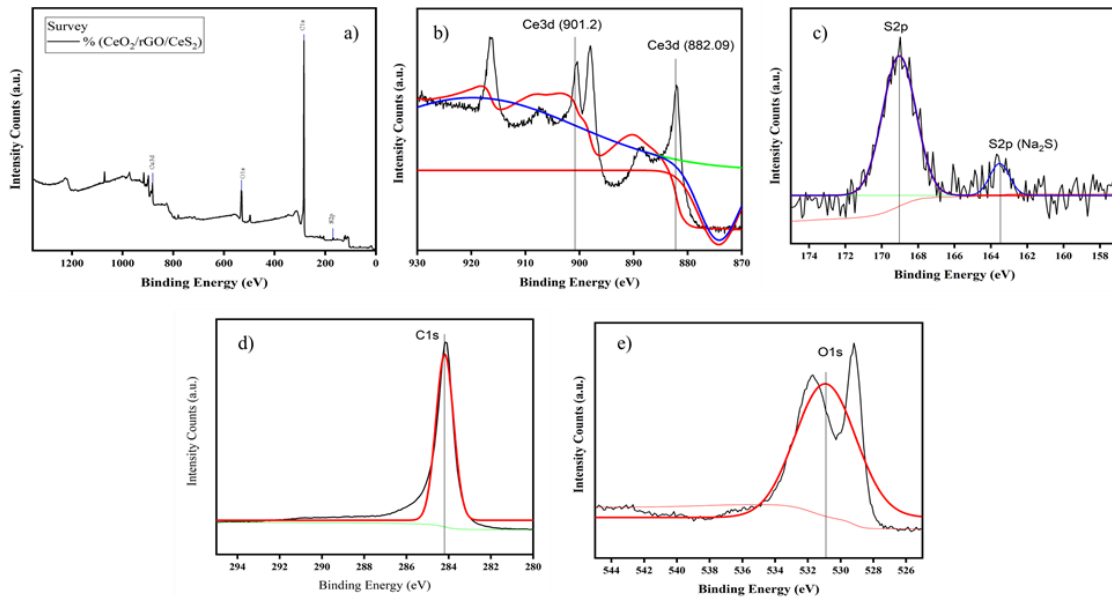


Figure 33 a) XPS survey of CeO₂/rGO/CeS₂ composite, b)XPS spectrum for Ce3d, c) XPS spectrum for S2p, d)XPS spectrum for C1s, e) XPS spectrum for O1s

5.1.5 Fourier Transform Infrared Spectroscopy-FTIR

FTIR analysis was done in order to find out the existence of the essential functional groups at designated peak positions. Figure 34 represents the FTIR spectra for the prepared

sample, i.e., CeO₂/rGo/CeS₂. The graph demonstrates the specific peak positions confirming the presence of rGO instead of GO. As per the reported literature, the FTIR spectra for GO shows the C-O stretching vibrations at 1066 cm⁻¹, C-O-C bending at 1288 cm⁻¹, C-OH bending at 1587 cm⁻¹, C=O stretching at 1724 cm⁻¹, and OH stretching at 3448 cm⁻¹. It can be seen in the figure that there are no considerable peaks in the FTIR spectra of the synthesized composite material, at 1066 cm⁻¹, 1288 cm⁻¹, 1724 cm⁻¹, and 3448 cm⁻¹. The low intensity of these peaks confirms the presence of rGO in the sample instead of graphene oxide.

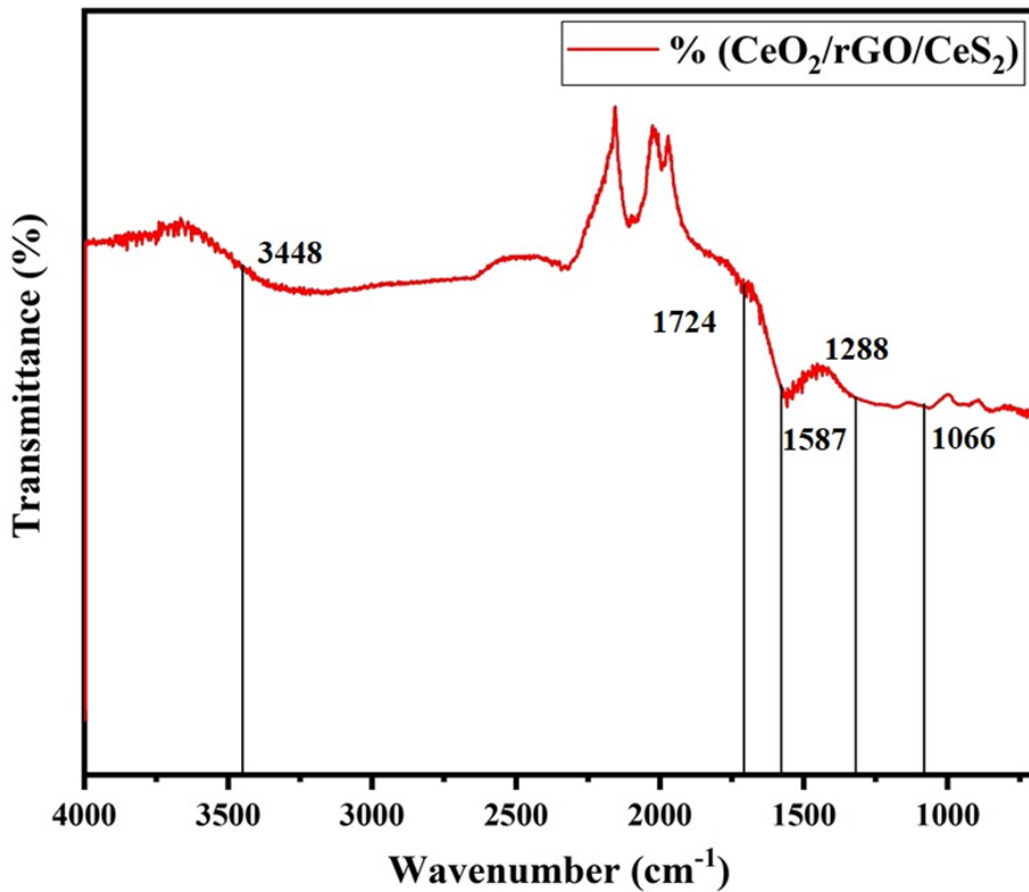


Figure 34 FTIR spectra of CeO₂/rGO/CeS₂ composite

5.1.6 Raman Spectroscopy

Raman spectroscopy was carried out in order to find out the inelastic scattering of the molecules that are irradiated by a beam of monochromatic light. Figure 35 demonstrates the Raman spectrum for the $\text{CeO}_2/\text{rGO}/\text{CeS}_2$ composite. The figure represents multiple peaks that correspond to specific materials. In order to confirm the existence of rGO instead of GO in the sample, the peaks in the range of 1000 and 1700 are considered. The higher intensities at the D band in the graph suggest that the excess oxygen has been removed, which confirms the presence of rGO instead of GO[10]. The I_D/I_G ratio for GO is reported to be 0.86 in the literature, while in this work this ratio tends to decrease in the case of rGO due to reduction.

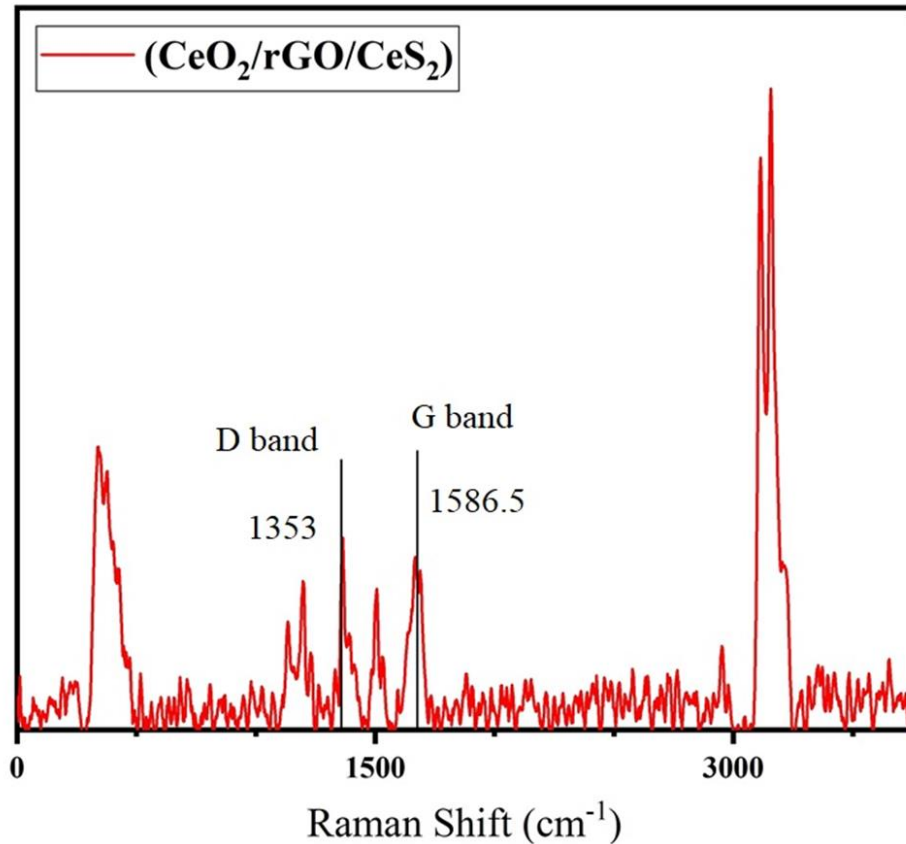


Figure 35 Raman Spectroscopy of $\text{CeO}_2/\text{rGO}/\text{CeS}_2$ composite

5.1.7 Thermal Gravimetric Analysis

The TGA analysis of the prepared materials is displayed in Figure 36. Considering the Ce-BTC, a slight weight loss was detected at 100 °C which explains the loss of water, which

was adsorbed physically, then there was a steady loss in weight up until 500 °C which represents DMF and water synchronized within the pores of the MOF, and then there was a major reduction in weight from 550 °C to 650 °C which can be explained by the disintegration of the MOF. Similarly, with CeO₂/rGO the pattern represents an initial mass loss below 100 °C which attributes to the loss of adsorbed water. The second major mass loss at 300 °C attributes to the disintegration of rGO and loss of organic elements present in MOF-derived CeO₂. The weight-loss trend in CeO₂/rGO/CeS₂ composite shows a sharp decrease of weight at 100 °C, then there is a continuous gradual loss in weight until 600 °C which attributes to the gradual decomposition of rGO and CeS₂. As there are no drastic weight losses in the case of composite, this represents the relatively better thermal stability of the composite.

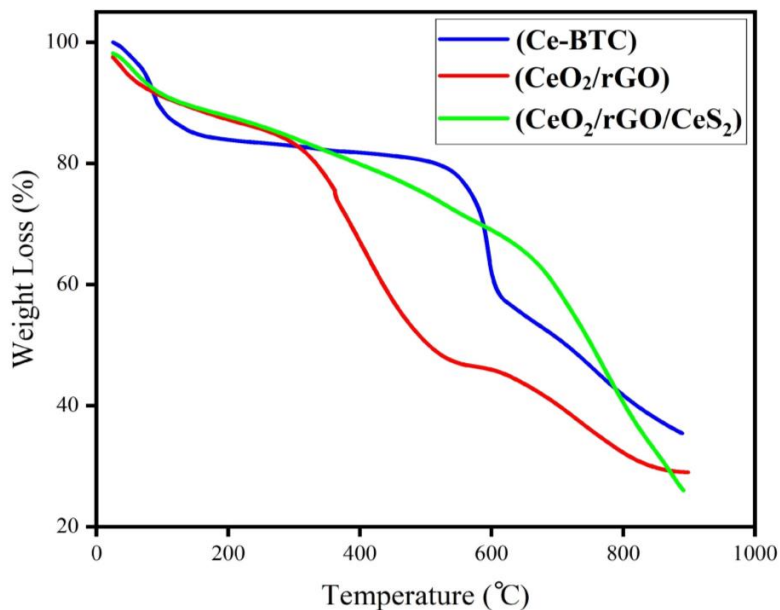


Figure 36 Thermogravimetric analysis of Ce-BTC MOF, CeO₂/rGO, and CeO₂/rGO/CeS₂ composite

5.2 Electrochemical Measurements

The electrochemical characterization was done by cyclic-voltammetry analysis (CV), chrono-potentiometry technique (CP), and electrochemical impedance spectroscopy (EIS) in an electrolyte made with 3 M KOH.

5.2.1 Cyclic Voltammetry

The CV curves were examined at various scan rates in the scale of 10 mVs⁻¹ up to 100 mVs⁻¹ in the potential range of 0-0.5 V, Figure 37(a, b, c). By enhancing the scan rate values, the peak value of the CV curve was enhanced which represents the quasi-reversible nature of the electrodes. This trend can be attributed to the fast anion exchange and rapid electron transfer in between the sulfide ions and electrolyte. The oxidation-reduction peaks instead of rectangular peaks, refer to the faradaic pseudo-capacitive nature of the sulfur based composite electrodes. To calculate the specific capacitances of the composite electrodes, following formula was used:

$$C_m = \frac{\int IdV}{2mv\Delta V} \quad (6)$$

This specific equation is used for the three-electrode configuration to determine the specific capacitance from CV analysis. The maximum calculated specific capacitance of the CeO₂/rGO/CeS₂ nanocomposite electrode was calculated to be 720 Fg⁻¹ at a scan rate of 10mVs⁻¹. On the other hand, the highest specific capacitance of CeO₂/rGO composite was computed to be 568 Fg⁻¹ at 10 mVs⁻¹. The difference in the specific capacitance's attributes to the greater surface area, mesoporous structure, and decreased crystallinity of the CeO₂/rGO/CeS₂ nanocomposite. Figure 37(d) represents the specific capacitance against distinct scan rates in the range of 10 mVs⁻¹ to 100 mVs⁻¹. It is clear from the figure and Table 2 Scan Rates versus specific capacitances of CeO₂/rGO, and CeO₂/rGO/CeS₂, that if the scan rate is increased, the specific capacitance drops. This decrease in the specific capacitance at elevated scan rates can be rationalized by two conditions involving the lower levels of resistance and kinetic energy of ions at lower scan rates, as under these conditions the ions have more time to interact with the electrode surface. Then again, higher scan rates allow the ions a minimum time to intermingle with the surface of the electrode as the kinetic energy of the ions is improved which produces relatively more resistance, reducing the specific capacitance value.

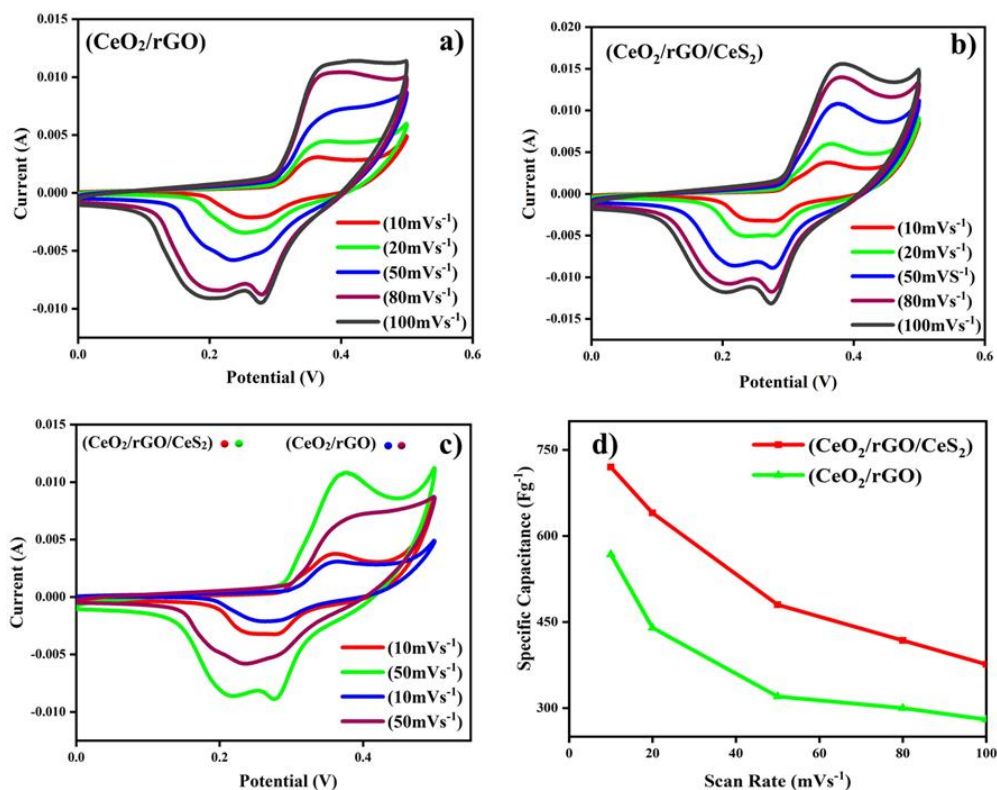


Figure 37 CV analysis at different scan rates for, (a) CeO₂/rGO (b) CeO₂/rGO/CeS₂ (c) Comparison of CV curves for CeO₂/rGO and CeO₂/rGO/CeS₂ (d) Scan Rate versus Specific Capacitance for CeO₂/rGO and CeO₂/rGO/CeS₂

Table 2 Scan Rates versus specific capacitances of CeO₂/rGO, and CeO₂/rGO/CeS₂

| Scan Rate (mVs ⁻¹) | Specific Capacitance (Fg ⁻¹) | |
|--------------------------------|--|--|
| | CeO ₂ /rGO | CeO ₂ /rGO/CeS ₂ |
| 10 | 568 | 720 |
| 20 | 440 | 640 |
| 50 | 320 | 480 |
| 80 | 300 | 418 |
| 100 | 280 | 376 |

5.2.2 Chronopotentiometry

The charge-discharge properties of the assembled electrodes were analyzed by chronopotentiometry. Figure 38(a, b, c) signifies the galvanic charge/discharge (GCD) curves of the two composite electrodes at a maximum employed voltage value of 0.5 V. The GCD curves represent a non-triangular shape with plateaus at approximately 0.2 V and 0.3 V, respectively, which shows the existence of pseudocapacitive behavior of the electrodes caused due to the faradic reactions. It is also evident from the figure that with the addition of CeS₂, the overall conductivity of the composite is increased resulting in high specific energy, and specific power, which was concluded from the specific capacitance using the following equations:

$$E = \frac{1}{2} \frac{C_m (\Delta V)^2}{3.6} \quad (7)$$

$$P = \frac{E}{\Delta t} \times 3600 \quad (8)$$

Here, C_m is specific capacitance (Fg^{-1}), E is energy density ($Whkg^{-1}$), P represents the power density (Wkg^{-1}), and Δt is the discharge-time that is represented in seconds (s). The maximum energy and power densities were calculated to be $23.5 Whkg^{-1}$ and $2917.5 Wkg^{-1}$, respectively.

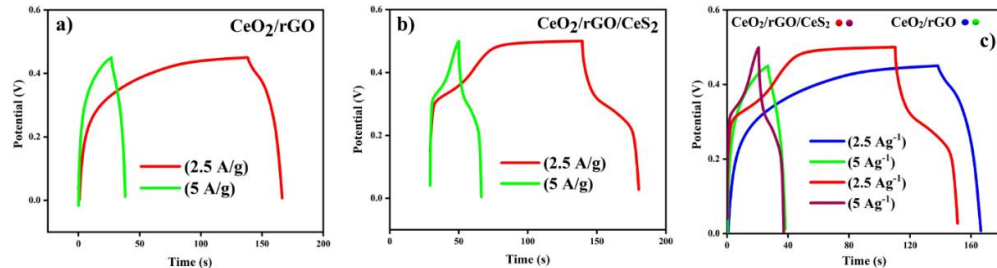


Figure 38 Galvanic Charge-Discharge curves of, (a) CeO₂/rGO, (b) CeO₂/rGO/CeS₂, (c) Comparison between GCD curves of CeO₂/rGO and CeO₂/rGO/CeS₂

5.2.3 Cyclic Stability

Moreover, to examine the cyclic stability and durability of the $\text{CeO}_2/\text{rGO}/\text{CeS}_2$ composite electrode, cycle stability analysis was done at a 100 mVs^{-1} scan rate for consecutive cycles up to 3000. The Figure 39 demonstrates that the specific capacitance of $\text{CeO}_2/\text{rGO}/\text{CeS}_2$ nanocomposite increased with the increasing number of cycles up to ~ 2600 cycles and then showed a consistent decreasing trend up to 3000 cycles. This phenomenon posits the concept that still more cycles are required for the activation of $\text{CeO}_2/\text{rGO}/\text{CeS}_2$ nanocomposite. The maximum value of specific capacitance was obtained after ~ 2600 cycles, i.e., 428.6 Fg^{-1} . The exceptional electrochemical activity of the prepared nanocomposite can be attributed to the excellent cyclic stability of the nanocomposite. Figure 39 posits that the exceptional electrochemical capability of the nanocomposite can be accredited to the good electrical conductivity of CeS_2 , as it provides a smooth track for the movement of the electrons among electrolyte ions and the electrode surface. Also, the activation of CeO_2 was carried out after the electrolyte penetrated through the surface with the increasing number of cycles, which enhanced the bulk electron transfer and provided the required stability to the electrode.

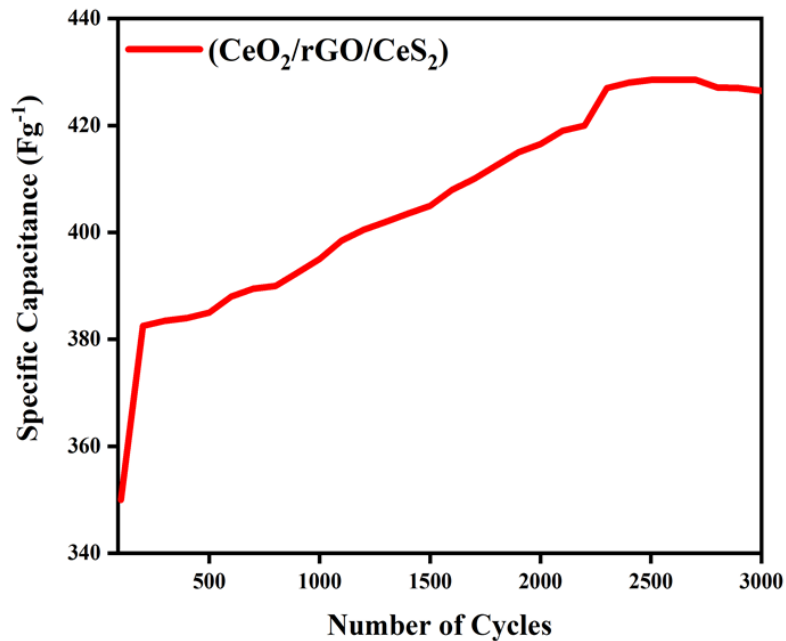


Figure 39 Capacitance Retention of $\text{CeO}_2/\text{rGO}/\text{CeS}_2$ composite at 100 mVs^{-1} for 3000 cycles

5.2.4 Electrochemical Impedance Spectroscopy

To evaluate the charge-transfer phenomenon based on the concept of frequency, EIS investigation was done at the frequency of 100 kHz to 1 kHz. It is evident from Figure 40, in case of the $\text{CeO}_2/\text{rGO}/\text{CeS}_2$ nano composite, the distinctive semicircle plot is not visible in the upper component of the frequency range, but the imaginary part of the plot increases vertically which represents the good pseudocapacitive performance of the composite electrode due to the oxide functional groups in rGO. In the case of CeO_2/rGO composite, the semicircle cannot be seen, also the imaginary part of the plot is not showing significant vertical growth, which means that the composite does not possess good capacitive behavior.

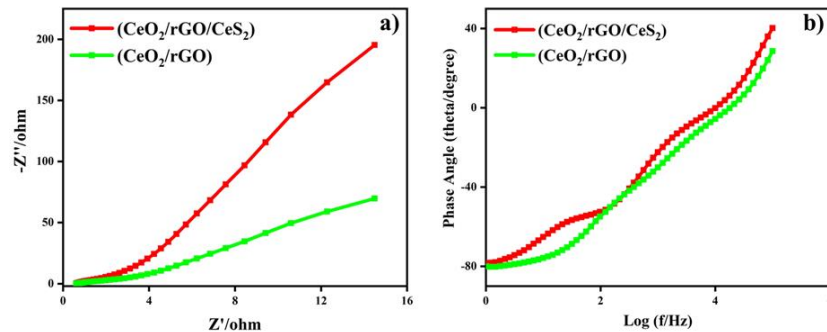


Figure 40 Electrochemical Impedance Spectroscopy (EIS) measurements, (a) Nyquist plot CeO_2/rGO and $\text{CeO}_2/\text{rGO}/\text{CeS}_2$, (b) Bode plot for CeO_2/rGO and $\text{CeO}_2/\text{rGO}/\text{CeS}_2$

Similarly, the Bode plot of $\text{CeO}_2/\text{rGO}/\text{CeS}_2$ and CeO_2/rGO represents that at low frequency regions the phase angle lies in the range of 70 to 80 degrees, which refers to the redox reactions and excellent capacitor behavior of the composites. The phase angle for the $\text{CeO}_2/\text{rGO}/\text{CeS}_2$ nanocomposite is relatively higher than the CeO_2/rGO composite, due to the good conductivity and good pseudocapacitance behavior. With the increase in frequency values, the phase angle decreases, which can be explained by the limited adsorption of the ions onto the electrode surface that significantly reduces the number of active sites resulting in less specific capacitance.

Summary

All the results obtained during the research are discussed in this chapter. Characterization results of XRD, SEM, EDS, and TGA are supported with facts from previous studies and justified to understand the morphology, structure, composition, thermal stability, functional groups, surface area and porosity of the synthesized materials. The testing results for electrocatalytic CO₂ reduction are explained at the end and their link with characterization properties of material are justified and compared with literature work.

References

- [1] N. Bibi, Y. Xia, S. Ahmed, Y. Zhu, S. Zhang, and A. Iqbal, "Highly stable mesoporous CeO₂/CeS₂ nanocomposite as electrode material with improved supercapacitor electrochemical performance," *Ceram. Int.*, vol. 44, no. 18, pp. 22262–22270, Dec. 2018, doi: 10.1016/j.ceramint.2018.08.348.
- [2] S. K. Jha, C. Naveen Kumar, R. P. Raj, N. S. Jha, and S. Mohan, "Synthesis of 3D porous CeO₂/reduced graphene oxide xerogel composite and low level detection of H₂O₂," *Electrochim. Acta*, vol. 120, pp. 308–313, 2014, doi: 10.1016/j.electacta.2013.12.051.
- [3] T. Noor, M. Ammad, N. Zaman, N. Iqbal, L. Yaqoob, and H. Nasir, "A Highly Efficient and Stable Copper BTC Metal Organic Framework Derived Electrocatalyst for Oxidation of Methanol in DMFC Application," *Catal. Letters*, vol. 149, no. 12, pp. 3312–3327, Dec. 2019, doi: 10.1007/s10562-019-02904-6.
- [4] M. M. Peng, M. Ganesh, R. Vinodh, M. Palanichamy, and H. T. Jang, "Solvent free oxidation of ethylbenzene over Ce-BTC MOF," *Arab. J. Chem.*, vol. 12, no. 7, pp. 1358–1364, Nov. 2019, doi: 10.1016/j.arabjc.2014.11.024.
- [5] P. F. Santos and P. P. Luz, "Synthesis of a CE-based MOF-76 with high yield: A study of reaction parameters based on a factorial design," *J. Braz. Chem. Soc.*, vol. 31, no. 3, pp. 566–573, Mar. 2020, doi: 10.21577/0103-5053.20190218.

Chapter 6 Conclusions and Recommendation

6.1 Conclusions

This work comprises of the synthesis, characterization, and electrochemical analysis of CeO₂/rGO/CeS₂ composite which was derived from Ce-BTC (MOF). The as synthesized material composite was used as an electrode for supercapacitor applications. It demonstrated highest specific capacitance of 720 Fg⁻¹ at 10mVs⁻¹ scan rate, where the energy and power densities were calculated to be 23.5 Wh/kg and 2917.2 W/kg, respectively. The high conductivity of CeS₂ in the composite provided a platform for enhanced electron transfer among the electrolyte ions, and the porous electrode surface, while the CeO₂ provided better charge transport in the bulk. The large mesoporous structure of the Ce-BTC MOF and the pseudo-capacitive performance of reduced graphene oxide enhanced the electrochemical behavior of the electrode. The excellent cyclic stability showed by the electrode provides promising grounds for future research on the metal-oxide and metal-sulfide composites to be used as efficient electrode materials for supercapacitor applications.

6.2 Recommendations

The electrochemical performance and efficiency of supercapacitors for energy storage applications can be increased by exploring new combinations of materials to be employed as electrodes, in addition to the informed selection of electrolytes. The following recommendations are presented to address the shortcomings in the research regarding the electrode materials for supercapacitors:

1. Focus of the future research should be towards the various transition metals and their sulfides in addition to the metal oxides to be used as efficient electrode materials for supercapacitors.

2. Graphene based materials and composites should be explored to enhance the stretch, flexibility and electrochemical performance of the supercapacitors.
3. In contrast to Li-ion batteries, supercapacitors lack the required energy density. Therefore, research is required in the direction of hybrid batteries or hybrid capacitors, i.e., combination of Li-ion and supercapacitor assemblies, to ensure maximum power density and energy density simultaneously.
4. MOFs provide the basic framework for such applications, as they demonstrate large surface areas as compared to other compounds and composites. Research should be done to explore the various existing MOFs compounds and their derivatives.

Summary

This chapter includes the conclusion of all the research process and the results obtained. Also, a few recommendations are also made that could benefit the researchers in future that want to carry out research on this topic.

Appendix

Cerium based metal organic framework derived composite with reduced graphene oxide as efficient supercapacitor electrode.

Usman Ali Khan¹, Naseem Iqbal^{1*}, Tayyaba Noor², Rabia Ahmad¹, Awais Ahmad¹, Zain Amjad¹, Abdul Wahab¹

¹U.S-Pakistan Center for Advanced Studies in Energy (USPCAS-E), National University of Sciences and Technology (NUST) H-12, Islamabad

²School of Chemical and Materials Engineering (SCME), National University of Sciences and Technology (NUST), H-12, Islamabad, Pakistan

Corresponding author: naseem@uspcase.nust.edu.pk

Abstract

The excellent stability of CeO₂ coupled with the high-level conductivity of CeS₂ and enhanced electrochemical performance of rGO prove to be a workable nanocomposite electrode for supercapacitor applications. Here in this work, we synthesized mesoporous Ce-BTC metal-organic framework (MOF) derived CeO₂/rGO composite, which was then subjected to sulfidation to prepare CeO₂/rGO/CeS₂ nanocomposite, which was characterized by XRD, SEM, EDS, and TGA to find out its crystalline nature, material composition, morphology, and thermal stability. The electrochemical behavior of the metal oxide/sulfide composite was studied by making use of the cyclic voltammetry analysis (CV), chronopotentiometry (CP), and electrochemical impedance spectroscopy (EIS). The as-produced porous CeO₂/rGO/CeS₂ composite demonstrated the highest specific capacitance of 720 Fg⁻¹ in 3 M KOH electrolyte, with the specific energy and specific power of 23.5 Whkg⁻¹, and 2917.2 Wkg⁻¹ correspondingly, at a current density of 2.5 Ag⁻¹. The electrode demonstrated exceptional cyclic stability over 3000 cycles at a 100mVs⁻¹ scan rate. The brilliant electrochemical efficacy of the synthesized material was ascribed

to its tiered structure. The obtained results show that the CeO₂/rGO/CeS₂ composite opens new possibilities of metal sulfide composites as efficient electrodes for supercapacitor applications.

Keywords: Electrochemical Supercapacitors, Metal-Organic Framework, Pseudocapacitance, metal-sulfide composite.

Introduction

Due to the ever-rising requirement of electrical energy in the current era, owing to the increase in the use of electronic devices, the scientific world has been focusing on harvesting energy from renewable resources like wind, solar, thermal, etc. This increase in energy production has given rise to the need for efficient storage devices, i.e., Batteries and supercapacitors. Li-ion batteries are being developed and used for this very purpose for some time now. These batteries help improve the technological advancements ranging from compact electric gadgets to electric automobiles and renewable power generation and storage systems. Among various examples of the use of batteries is the Hybrid Electric Vehicle which uses a combination of a battery, an electric motor, and a combustion engine to increase the efficiency of the fuel [1]. Lithium-ion batteries despite having the maximum energy densities of all other energy storage systems demonstrate lower levels of specific power and cycle life. To cater to the specific power and cycle life, a new and more efficient storage device has been of significant importance these days, i.e., supercapacitors. supercapacitors have drawn a lot of interest in the last decade due to their efficient cycle life, high charge/discharge rate, and high power density [2]. Electrochemical supercapacitors refer to a kind of storage device for energy that can merge the remarkable specific power of an electrolytic capacitor with that of a battery in terms of the remarkable specific energy, making it an efficient alternative for a battery [3–5]. On the basis of the mechanism of supercapacitors to store charge, they can be categorized into two distinct kinds, i.e. Electric double-layer capacitors (EDLCs) and pseudo-capacitors [6]. In the case of the EDLCs, the charge is stored on the inner surface of active materials based on carbon [7] while pseudocapacitors store energy with electrochemical oxidation-reduction reactions [8–11] occurring on the active material's surface [12]. Although many electrode materials for pseudocapacitors have been developed which include materials based on

carbon [13–15] in addition to the transition metal oxides [16–18] and sulfides, and conducting polymers [19,20]. But there is still a need for further research to increase the efficiency of the supercapacitors.

Metal-Organic Frameworks (MOFs) have demonstrated promising results when used as base materials for electrodes of supercapacitor devices due to large surface area, adjustable pore sizes, and assimilated metal centers based on redox reactions [21,22]. MOFs can be incorporated into a supercapacitor in two ways. 1) By directly using them as an electrode for supercapacitors [23,24]. 2) MOF-derived materials like oxides, nanoporous carbons, and sulfides, etc. can be developed and then used as electrode materials [25–27]. So far, several MOFs and their derivatives have been developed as supercapacitor electrode material [28]. Several research papers have been published by our research group regarding the MOF derived and zeolitic imidazolate framework (ZIF) derived carbon materials and other derivatives to be used as effective electrocatalysts [29–35]. Porous carbon materials originated from ZIF are extensively examined as potential materials for electrode of supercapacitors [36]. But apart from the use of metallic or bimetallic MOF-derived materials, MOFs have a major limitation in the use of electrolytes, which decreases cyclic stability during an electrochemical charge/discharge process [37]. Moreover, MOFs can also be coupled with carbon compounds including carbon nanotubes, graphene, and reduced graphene oxide (rGO), etc. to increase the electrochemical performance of a supercapacitor [38,39]. Wen et al. reported a combination of Ni-MOF/CNT as a composite utilized for various applications in supercapacitor devices which consist of considerable specific energy value of 36.6 Whkg^{-1} [40]. Sarah et al. recently investigated the effects of rGO on a Cu-MOF and described that with the add-on of rGO, the electrochemical activity of Cu-MOF was significantly improved [41]. In short, the addition of carbon-based material in a MOF structure increases the stability of pseudocapacitors in addition to a tremendous increase in the electrochemical performance of the device.

MOF-76 signifies a category of compounds that are synthesized by the reaction of lanthanides and BTC (1,3,5-benzenetricarboxylic acid) [42]. Among various applications of MOF-76 include highly efficient uranium sorption, adsorbing dyes, and fluorescence detecting aromatic pollutants [43]. Ce-BTC is one of the MOFs formed from the mentioned

combination and it was used as a favorable material for electrode of supercapacitors. Also, Ce-BTC transition metal sulfides and oxides have recently established their usefulness for supercapacitors, due to the large internal surface area that is easily accessible, and it can expedite the diffusion of ions through the extremely porous substructure. Guojin Zeng et. al. synthesized Ce-oxide derived from Ce-BTC, which showed excellent specific capacitance of 779 Fg^{-1} at 1 Ag^{-1} current density, while the retention of capacitance was maintained at 91% at 10000 cycles [44]. Rajendran Ramachandran et. al. reported a specific capacitance of a huge value of 2221.2 Fg^{-1} with an amazing specific energy value of 111.05 Whkg^{-1} at 1 Ag^{-1} current density for Ce-BTC/GO composite in an electrolyte combination of 3 M KOH+0.2 M $\text{K}_3\text{Fe}(\text{CN})_6$ [45].

Apart from metal oxides, metal sulfides are gaining importance regarding being used as electrodes for supercapacitors because of their better electrical conductivity and more flexibility than the corresponding oxides of metals because of the smaller values of electronegativity for sulfur as compared to oxygen [6,46]. But the limitation of metal sulfide is that they do not show considerable cyclic stability when used directly as the electrodes [47,48]. To cater to this limitation metal sulfides can be coupled with metal oxides to make a composite that shows good electrical conductivity and better cyclic stability. In this work we synthesized Ce-BTC derived CeO_2/rGO and further converted it into $\text{CeO}_2/\text{rGO}/\text{CeS}_2$ nanocomposite by a wet chemical route. The as-obtained composite was then characterized by various techniques to find out its crystal structure, morphology, and electrochemical capability.

Experimental

Materials

The precursors utilized were Cerium-Nitrate-hexahydrate ($\text{Ce}(\text{NO}_3)_3 \cdot 6\text{H}_2\text{O}$), and Trimesic acid (1,3,5- H_3BTC) was used as the linker. The solvent was an Ethanol and D.I Water solution in the ratio (3:1). Sodium sulfide was used for sulfidation while the improved hummers method was utilized to synthesize graphene oxide.

Synthesis of Ce-BTC

The following synthesis method was used for Ce-BTC; A 50 mL solution was made by using a combination of 2mM 1,3,5-benzenetricarboxylic acid, and 8mM Cerium-Nitrate-Hexahydrate in DMF, which was then mixed for 30 min at 400 rpm. The as-prepared solution was subjected to thermal treatment in a Teflon-lined 100 mL autoclave made of steel, and subjected to 120 °C temperature for 24 hrs. It was then cooled naturally at the standard room temperature. The obtained samples were extracted by the separation technique known as centrifugation followed by repeated washing with DMF and ethanol. Finally, the acquired powder was subjected to vacuum drying 80 °C for 14 hrs. The schematic representation of the synthesis scheme for Ce-BTC is demonstrated in Figure 41.

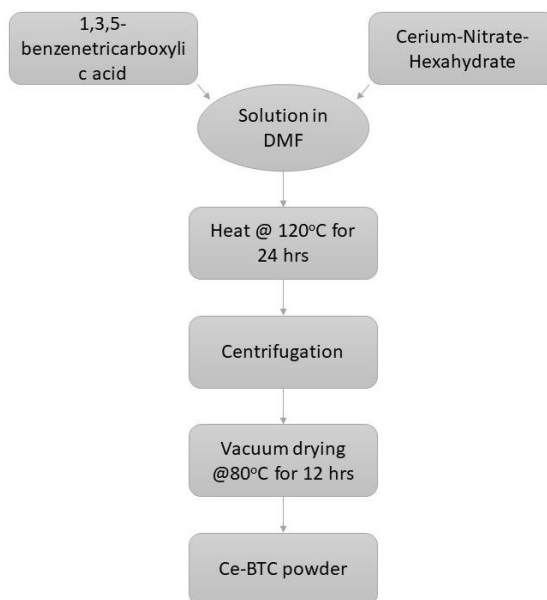


Figure 41 Schematic Representation of Preparation of Ce-BTC

Preparation of CeO₂/rGO composite

Ce-BTC powder was mixed with graphene oxide powder in ethanol solution and sonicated for 1hr. The resultant composite was extracted by centrifugation and dried at 80 °C for 12hrs. It was then subjected to thermal treatment at 350 °C for 90 minutes in a tube furnace, and the temperature was gradually amplified to 600 °C at the ramp of 4 °C min⁻¹. It was then pyrolyzed for 3 hrs at 600 °C under an inert (Hydrogen, Argon) environment and the temperature was spontaneously brought down to room temperature. The schematic

representation of the preparation scheme for CeO₂/rGO composite is demonstrated in Figure 42.

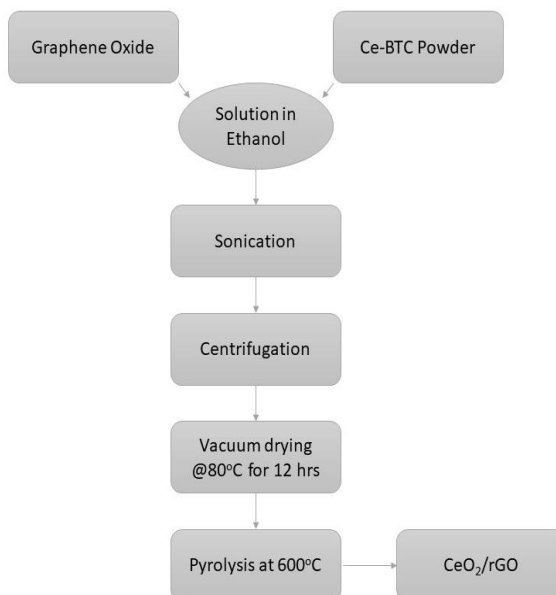


Figure 42 Schematic representation of preparation of CeO₂/rGO composite

Ce-BTC derived CeO₂/rGO/CeS₂ composite

The as-obtained CeO₂/rGO composite obtained from pyrolysis was treated for 6 hrs with 0.5 M sulfuric acid, washed, and finally dried at 80 °C for 14 hrs in a vacuum. The dried powder was then added in 30 mL DI water and thoroughly stirred at room temperature and pressure. A separate solution was prepared with 0.1 M Sodium Sulfide in 30 mL water. The two prepared solutions were mixed with a magnetic and stirred at 400 rpm under standard room temperature and pressure. The as-prepared solution was then heated at 180 °C for 14 hrs under high pressure in a 100 mL autoclave with Teflon lining inside, washed multiple times with water in a centrifuge, and subjected to vacuum drying at 70 °C for 12 hrs. The schematic representation of the preparation scheme for CeO₂/rGO/CeS₂ is demonstrated in Figure 43.

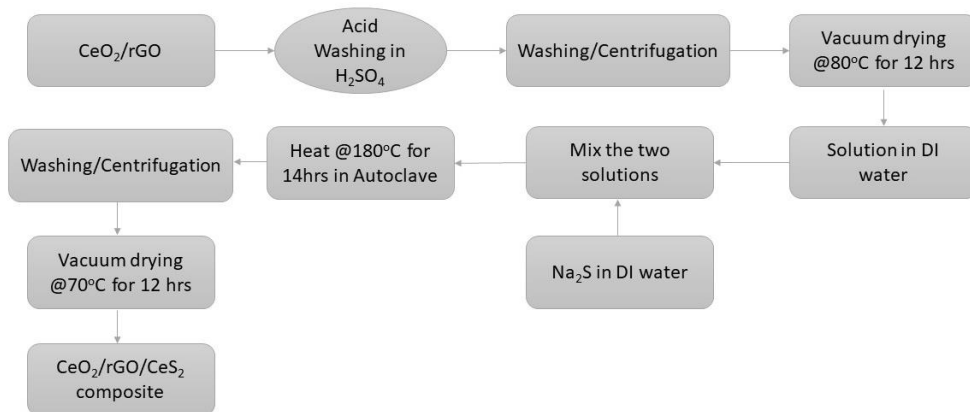


Figure 43 Schematic representation of Synthesis of CeO₂/rGO/CeS₂ nanocomposite

Materials Characterization

The prepared materials were subject to imaging from a scanning electron microscope (SEM) (VEGA3,51–ADD0007) (Tescan, Brno, Czech Republic) in order to find out the morphology of the samples, while the chemical composition was presented by EDS. X-ray diffraction method (D8 Advance, CuK α , $\lambda = 1.54 \text{ \AA}$) (Bruker, Karlsruhe, Germany) was implemented to demonstrate the crystalline assembly of the prepared samples, while the thermo-gravimetric analysis (TGA) was done with a DTG–60H (Shimadzu, Kyoto, Japan) equipment in a wide array of temperature of up to 900 °C.

Electrochemical measurements

The electrochemical characterization of the prepared samples was done with an electrochemical workstation CHI 760E (CH Instrument, Texas, USA). The apparatus used for characterization was based on a three-electrode system involving a counter-electrode made up of a platinum coil, a reference-electrode of (Ag/AgCl), and a working electrode. The assembly of the working electrode was completed by depositing the ink prepared from the samples onto a 1×1 cm piece of Ni-foam by dip coating, which was then dried at 70 °C for 6hrs and immersed in 3 M KOH electrolyte before connecting it to the three-electrode system. The preparation scheme for the ink is as follows: 2.5 mg of active material was dissolved in ethanol (0.08 mL) and Nafion (0.03 ml) solution to develop a homogeneous ink. Cyclic Voltammetric analysis was done over a voltage span of 0 V-0.5 V in a 3 M

KOH electrolyte at diverse scan rates ranging from 10 to 100 mVs⁻¹ including 10, 20, 50, 80, and 100 mVs⁻¹. Electrochemical impedance spectroscopy (EIS) was done at a frequency of 1 Hz to 10⁵ Hz in 3 M KOH electrolyte. The galvanostatic charge/discharge analysis was done by the chronopotentiometry technique, where the cathodic current was maintained at 0.1mA in a potential frame of 0.5 V.

Results and Discussions

X-ray Diffraction-XRD

X-ray Diffraction Method was utilized to confirm the crystalline assembly of Ce-BTC before pyrolysis, CeO₂/rGO composite after pyrolysis, and the CeO₂/rGO/CeS₂ composite after sulfidation. *Figure 44(a)* represents the XRD pattern for Ce-BTC and the peak positions at 8.4°, 10.5°, 18.05° (2θ) determine the good crystallinity of Ce-BTC, which is aligned with the results of the literature [49,50]. *Figure 44(b)* represents the XRD peaks obtained after the pyrolysis of Ce-BTC. The peaks appearing at 28.4°, 32.9°, 47.3°, and 56.2° (2θ) confirm the formation of CeO₂/rGO which is in accordance with the JCPDS card number (81-0792).

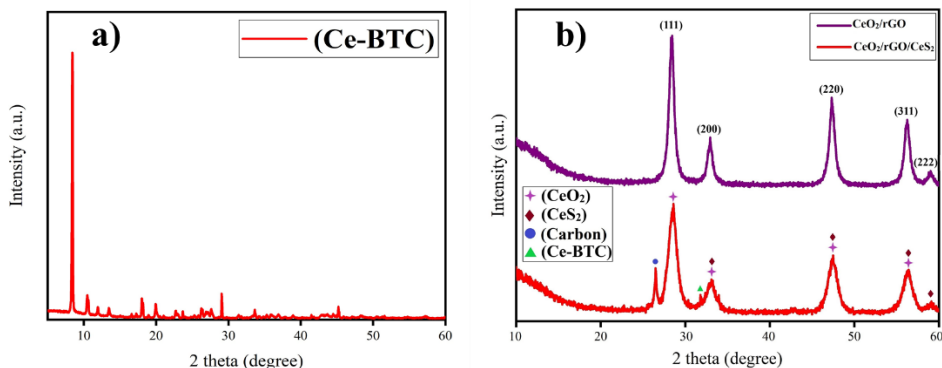


Figure 44. Represents the XRD pattern of, a) Ce-BTC, b) CeO₂/rGO composite and CeO₂/rGO/CeS₂ composite.

It is clear from the pattern that the influence of graphene oxide is not significant as only a small quantity was added [51]. According to the diffraction peak at (220), the size of the crystallite for CeO₂/rGO was calculated to be 11.467nm using the Sherer equation which revealed that it consists of nanocrystal units. The XRD pattern was determined for the CeO₂/rGO/CeS₂ composite, which was consistent with the literature [46]. The wide

diffraction peak at 26.4° (2θ) represents graphite carbon. The appearance of the characteristic peaks of CeO_2 , CeS_2 , and rGO verifies the formation of the nanocomposite. No extra peaks were detected, which verifies the formation of pure $\text{CeO}_2/\text{rGO}/\text{CeS}_2$ nanocomposite.

Scanning Electron Microscope-SEM

SEM measurements demonstrated the morphology of the prepared materials, as shown in *Figure 45*(a, b, c). Metal-Organic Framework Ce-BTC showed pillar-like rods which is consistent with the literature [49,52]. The particle size for the Ce-BTC pillar-like rods was found to be 37.47nm which confirms the mesoporous structure of Ce-BTC, hence more electrochemical activity. After pyrolysis at 600°C , the morphology was changed to cubic structures on a BTC framework, while nanoparticles of reduced graphene oxide were dispersed over the cubic morphology of cerium oxide, holding it together. Morphology features of $\text{CeO}_2/\text{rGO}/\text{CeS}_2$ composite are displayed in *Figure 45*(c).

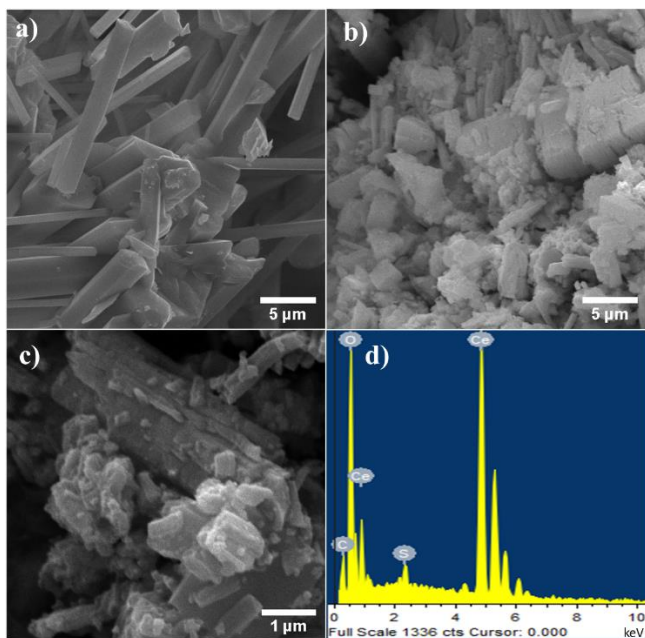


Figure 45. SEM images of, a) Pillar like rods of Ce-BTC, b) Cubic CeO_2/rGO , c) Irregular nanorods of $\text{CeO}_2/\text{rGO}/\text{CeS}_2$ composite, and d) EDX measurements for C:O:S:Ce

The image shows the formation of Irregular nanorods, grown on the BTC framework. Several cubic structures can be seen in the image that confirms the existence of CeO_2 in

the composite and the rGO nanoparticles can be seen dispersed and holding the crystal structures together over the BTC framework. The atomic percentage of C, O, S, and Ce was established by the energy-dispersive X-ray spectroscopy (EDS) measurements, *Figure 45(d)*. Table 3 represents the atomic ratios and weight% of the elements present in the CeO₂/rGO/CeS₂.

Table 3. EDX analysis of CeO₂/rGO/CeS₂ nanocomposite

| Element | Weight % | Atomic Ratio |
|---------|----------|--------------|
| C | 49.70 | 70.70 |
| O | 24.33 | 25.99 |
| S | 0.35 | 0.19 |
| Ce | 25.62 | 3.12 |

Thermal Gravimetric Analysis

The TGA analysis of the prepared materials is displayed in *Figure 46*. Considering the Ce-BTC, a slight weight loss was detected at 100 °C which explains the loss of water which was adsorbed physically, then there was a steady loss in weight up until 500 °C which represents DMF and water synchronized within the pores of the MOF, and then there was a major reduction in weight from 550 °C to 650 °C which can be explained by the disintegration of the MOF. Similarly, with CeO₂/rGO the pattern represents an initial mass loss below 100 °C which attributes to the loss of adsorbed water. The second major mass loss at 300 °C attributes to the disintegration of rGO and loss of organic elements present in MOF-derived CeO₂ [53]. The weight-loss trend in CeO₂/rGO/CeS₂ composite shows a sharp decrease of weight at 100 °C, then there is a continuous gradual loss in weight until 600 °C which attributes to the gradual decomposition of rGO and CeS₂. As there are no drastic weight losses in the case of composite, this represents the relatively better thermal stability of the composite.

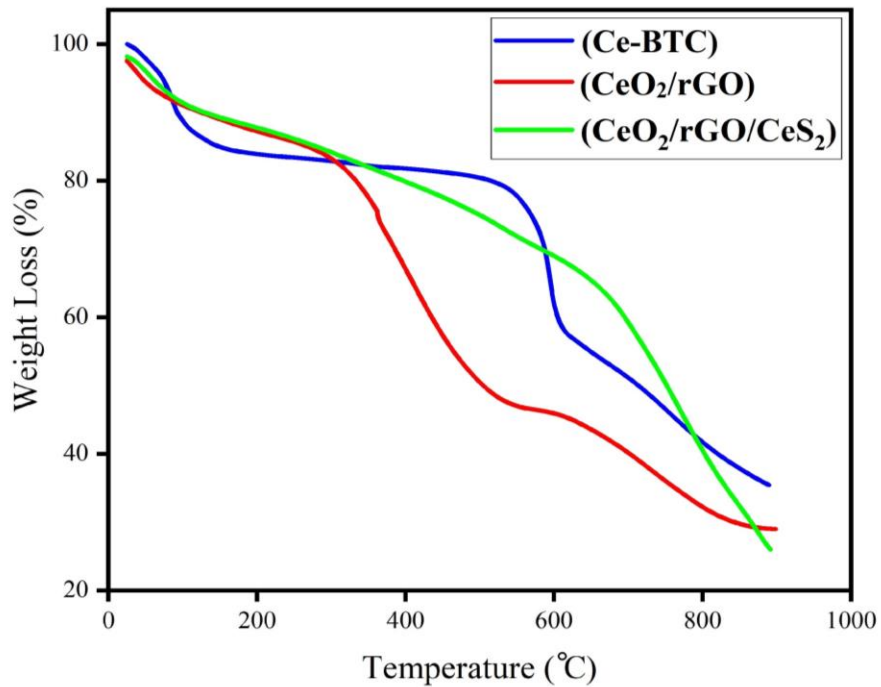


Figure 46 Thermogravimetric analysis of Ce-BTC MOF, CeO₂/rGO, and CeO₂/rGO/CeS₂ composite

Fourier Transform Infrared Spectroscopy

FTIR analysis was done in order to find out the existence of the essential functional groups at designated peak positions. *Figure 47* represents the FTIR spectra for the prepared sample, i.e., CeO₂/rGo/CeS₂. The graph demonstrates the specific peak positions confirming the presence of rGO instead of GO. As per the reported literature [54], the FTIR spectra for GO shows the C-O stretching vibrations at 1066 cm⁻¹, C-O-C bending at 1288 cm⁻¹, C-OH bending at 1587 cm⁻¹, C=O stretching at 1724 cm⁻¹, and OH stretching at 3448 cm⁻¹. It can be seen in the figure that the that there are no considerable peaks in the FTIR spectra of the synthesized composite material, at 1066 cm⁻¹, 1288 cm⁻¹, 1724 cm⁻¹, and 3448 cm⁻¹. The low intensity of these peaks confirms the presence of rGO in the sample instead of graphene oxide.

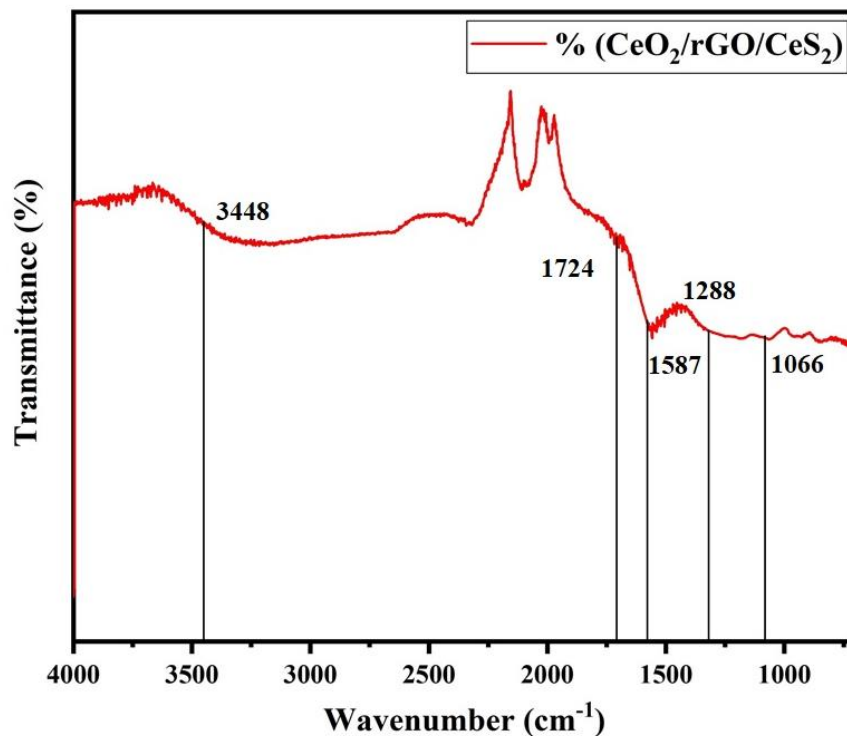


Figure 47 FTIR spectra of CeO₂/rGO/CeS₂ composite

Raman Spectroscopy

Raman spectroscopy was carried out in order to find out the inelastic scattering of the molecules that are irradiated by a beam of monochromatic light. *Figure 48* demonstrates the Raman spectrum for the CeO₂/rGO/CeS₂ composite. The figure represents multiple peaks that correspond to specific materials. In order to confirm the existence of rGO instead of GO in the sample, the peaks in the range of 1000 and 1700 are considered. The higher intensities at the D band in the graph suggest that the excess oxygen has been removed, which confirms the presence of rGO instead of GO [55]. The I_D/I_G ratio for GO is reported to be 0.86 in the literature, while in this work this ratio tends to decrease in the case of rGO due to reduction.

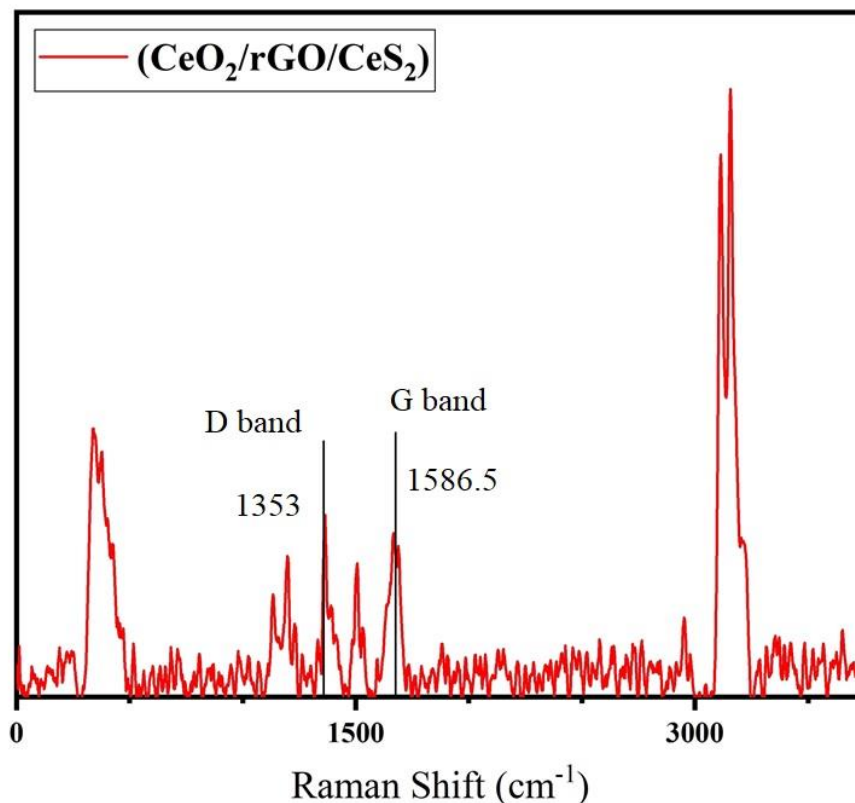


Figure 48 Raman Spectroscopy of $\text{CeO}_2/\text{rGO}/\text{CeS}_2$ composite

Transmission Electron Microscopy – (TEM)

TEM analysis was carried out in order to figure out the analytical characterization of the nanoparticles of the nanocomposite. In the case of $\text{CeO}_2/\text{rGO}/\text{CeS}_2$ nanocomposite, the TEM image demonstrates the small size of the particles in addition to the uniform distribution across the particle structure. Figure 9 represents the uniform distribution of the $\text{CeO}_2/\text{rGO}/\text{CeS}_2$ nanoparticles over the BTC framework. The dark spot in the center represent the sulfide and oxide particles while rGO can be seen distributed along the boundary of the composite.

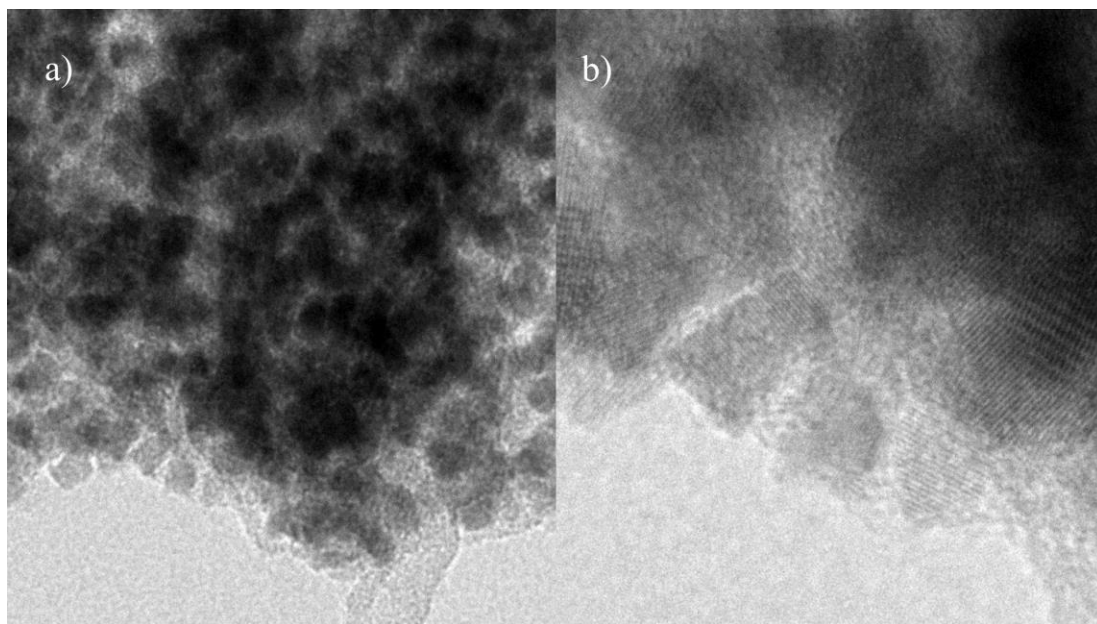


Figure 49 (a,b) TEM image for CeO₂/rGO/CeS₂ nanocomposite at 20 nm and 10 nm respectively

X-ray photoelectron spectroscopy

XPS analysis was done in order to confirm the elemental composition of the CeO₂/rGO/CeS₂ nanocomposite. Figure 10 (a) represents the detailed survey analysis of the CeO₂/rGO/CeS₂ composite with the help of XPS measurements. The figure represents the presence of four elements including Carbon (C1s), Cerium (Ce3d), Oxygen (O1s), and Sulfur (S2p) which demonstrates the elemental composition of CeO₂/rGO/CeS₂ nanocomposite. The spectrum for Ce3d represented two characteristic peaks at 882.09, and 901.2 confirming the existence of Ce⁺³ and Ce⁺⁴ oxidation states. The spectrum for S2p represented two peaks at 169.03 and 163.4 confirming the existence of sulfide. Similarly, O1s represented two distinct peaks at 529.2 and 531.8 demonstrating the existence of oxides. Finally, C1s represented one specific peak at 284.15 confirming the existence of carbon or rGO.

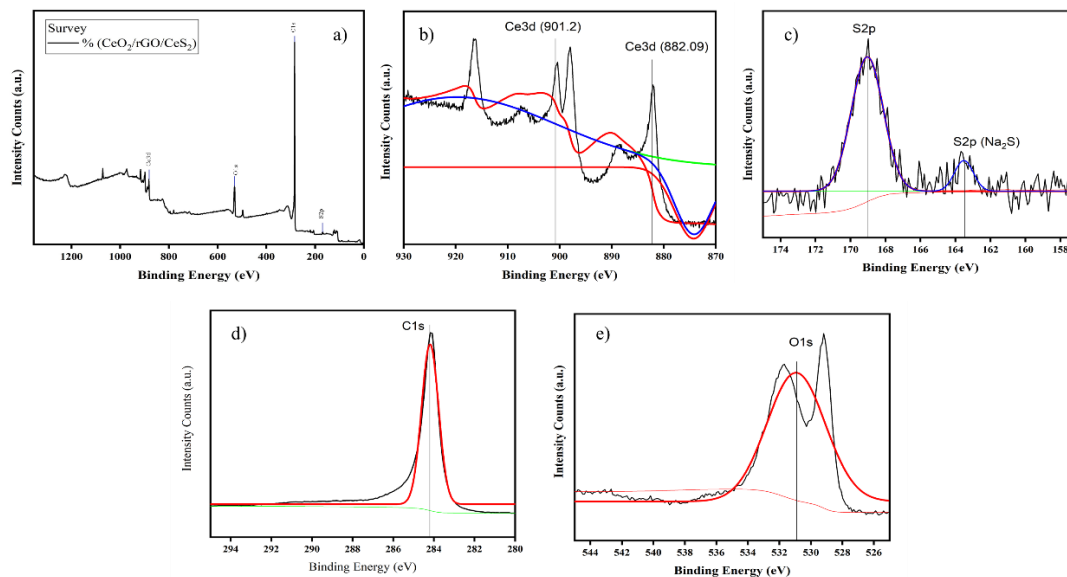


Figure 50 a) XPS survey of CeO₂/rGO/CeS₂ composite, b) XPS spectrum for Ce3d, c) XPS spectrum for S2p, d) XPS spectrum for C1s, e) XPS spectrum for O1s

Electrochemical Characterization

The electrochemical characterization was done by cyclic-voltammetry analysis (CV), chrono-potentiometry technique (CP), and electrochemical impedance spectroscopy (EIS) in an electrolyte made with 3 M KOH. The CV curves were examined at various scan rates in the scale of 10 mVs⁻¹ up to 100 mVs⁻¹ in the potential range of 0-0.5 V, *Figure 51*(a, b, c). By enhancing the scan rate values, the peak value of the CV curve was enhanced which represents the quasi-reversible nature of the electrodes [31]. This trend can be attributed to the fast anion exchange and rapid electron transfer in between the sulfide ions and electrolyte. The oxidation-reduction peaks instead of rectangular peaks refer to the faradaic pseudo-capacitive nature of the sulfur-based composite electrodes. To calculate the specific capacitances of the composite electrodes, the following formula was used [56]:

$$C_m = \frac{\int IdV}{2mv\Delta V}$$

This specific equation is used for the three-electrode configuration to determine the specific capacitance from CV analysis. The maximum calculated specific capacitance of the CeO₂/rGO/CeS₂ nanocomposite electrode was calculated to be 720 Fg⁻¹ at a scan rate of

10mVs⁻¹. On the other hand, the highest specific capacitance of CeO₂/rGO composite was computed to be 568 Fg⁻¹ at 10 mVs⁻¹. The difference in the specific capacitance's attributes to the greater surface area, mesoporous structure, and decreased crystallinity of the CeO₂/rGO/CeS₂ nanocomposite. *Figure 51(d)* represents the specific capacitance against distinct scan rates in the range of 10 mVs⁻¹ to 100 mVs⁻¹. It is clear from the figure and Table 4, that if the scan rate is increased, the specific capacitance drops. This decrease in the specific capacitance at elevated scan rates can be rationalized by two conditions involving the lower levels of resistance and kinetic energy of ions at lower scan rates, as under these conditions the ions have more time to interact with the electrode surface. Then again, higher scan rates allow the ions a minimum time to intermingle with the surface of the electrode as the kinetic energy of the ions is improved which produces relatively more resistance, reducing the specific capacitance value.

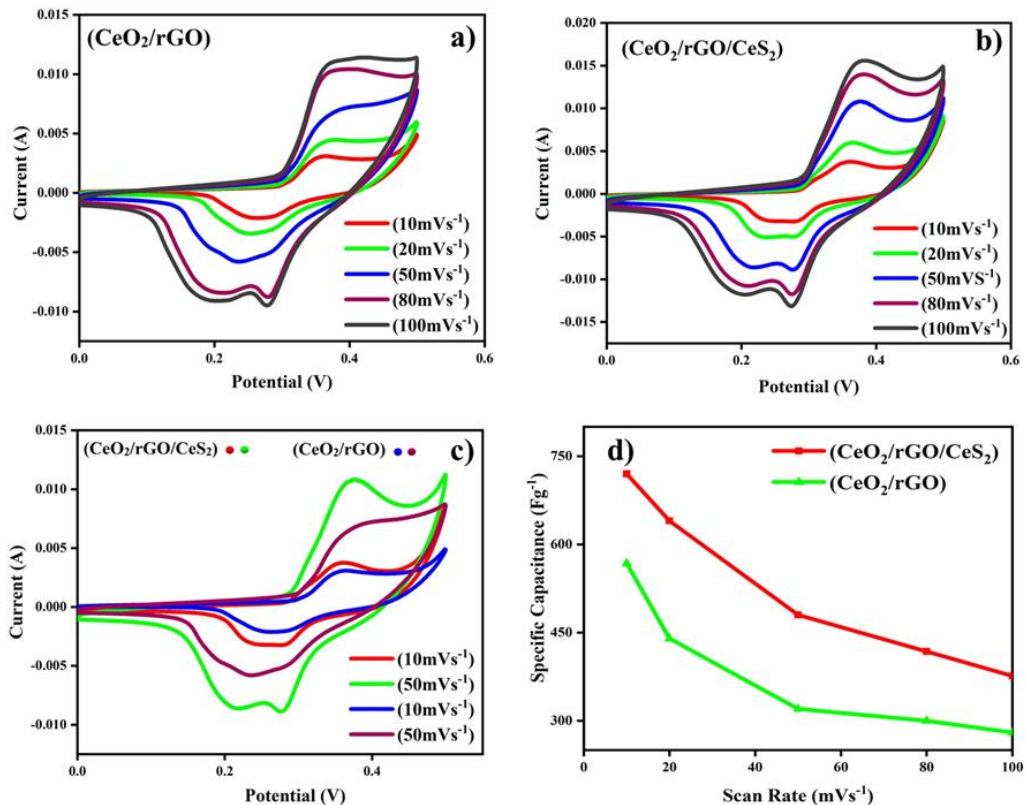


Figure 51. CV analysis at distinct scan rates for, (a) CeO₂/rGO (b) CeO₂/rGO/CeS₂ (c) Comparison of CV curves for CeO₂/rGO and CeO₂/rGO/CeS₂ (d) Scan Rate versus Specific Capacitance for CeO₂/rGO and CeO₂/rGO/CeS₂

Table 4. Scan Rates versus specific capacitances of CeO₂/rGO, and CeO₂/rGO/CeS₂

| Scan Rate (mVs ⁻¹) | Specific Capacitance (Fg ⁻¹) | |
|--------------------------------|--|--|
| | CeO ₂ /rGO | CeO ₂ /rGO/CeS ₂ |
| 10 | 568 | 720 |
| 20 | 440 | 640 |
| 50 | 320 | 480 |
| 80 | 300 | 418 |
| 100 | 280 | 376 |

The charge-discharge properties of the assembled electrodes were analyzed by chronopotentiometry. *Figure 52(a, b, c)* signifies the galvanic charge/discharge (GCD) curves of the two composite electrodes at a maximum employed voltage value of 0.5 V. The GCD curves represent a non-triangular shape with plateaus at approximately 0.2 V and 0.3 V, respectively, which shows the existence of pseudocapacitive behavior of the electrodes caused due to the faradic reactions. It is also evident from the figure that with the addition of CeS₂, the overall conductivity of the composite is increased resulting in high specific energy, and specific power, which was concluded from the specific capacitance using the following equations:

$$E = \frac{1}{2} \frac{C_m (\Delta V)^2}{3.6}$$

$$P = \frac{E}{\Delta t} \times 3600$$

Here, C_m is specific capacitance (Fg⁻¹), E is energy density (Whkg⁻¹), P represents the power density (Wkg⁻¹), and Δt is the discharge-time that is represented in seconds (s). The maximum energy and power densities were calculated to be 23.5 Whkg⁻¹ and 2917.5 Wkg⁻¹, respectively.

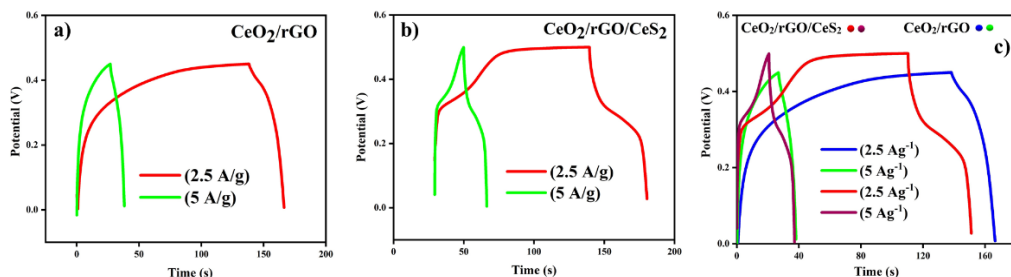


Figure 52. Galvanic Charge-Discharge curves of, (a) CeO₂/rGO, (b) CeO₂/rGO/CeS₂, (c) Comparison between GCD curves of CeO₂/rGO and CeO₂/rGO/CeS₂

Moreover, to examine the cyclic stability and durability of the CeO₂/rGO/CeS₂ composite electrode, cycle stability analysis was done at a 100 mVs⁻¹ scan rate for consecutive cycles up to 3000. The Figure 53 demonstrates that the specific capacitance of CeO₂/rGO/CeS₂ nanocomposite increased with the increasing number of cycles up to ~2600 cycles and then showed a consistent decreasing trend up to 3000 cycles. This phenomenon posits the concept that still more cycles are required for the activation of CeO₂/rGO/CeS₂ nanocomposite. The maximum value of specific capacitance was obtained after ~2600 cycles, i.e., 428.6 Fg⁻¹. The exceptional electrochemical activity of the prepared nanocomposite can be attributed to the excellent cyclic stability of the nanocomposite. Figure 53 posits that the exceptional electrochemical capability of the nanocomposite can be accredited to the good electrical conductivity of CeS₂, as it provides a smooth track for the movement of the electrons among electrolyte ions and the electrode surface. Also, the activation of CeO₂ was carried out after the electrolyte penetrated through the surface with the increasing number of cycles, which enhanced the bulk electron transfer and provided the required stability to the electrode.

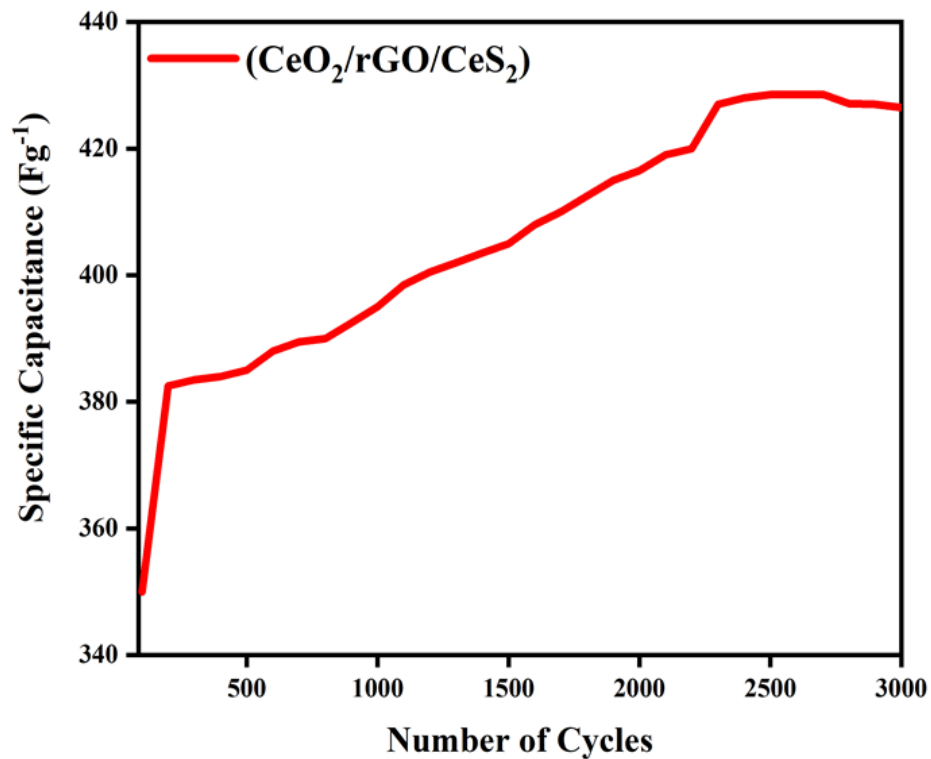


Figure 53. Capacitance Retention of CeO₂/rGO/CeS₂ composite at 100mVs⁻¹ for 3000 cycles

To evaluate the charge-transfer phenomenon based on the concept of frequency, EIS investigation was done at the frequency of 100 kHz to 1 kHz. It is evident from *Figure 54*, that considering the CeO₂/rGO/CeS₂ nanocomposite, the distinctive semicircle plot is not visible in the upper component of the frequency range, but the imaginary part of the plot increases vertically which represents the good pseudocapacitive performance of the composite electrode due to the oxide functional groups in rGO. In the case of the CeO₂/rGO composite, the semicircle cannot be seen, also the imaginary part of the plot is not showing significant vertical growth, which means that the composite does not possess good capacitive behavior.

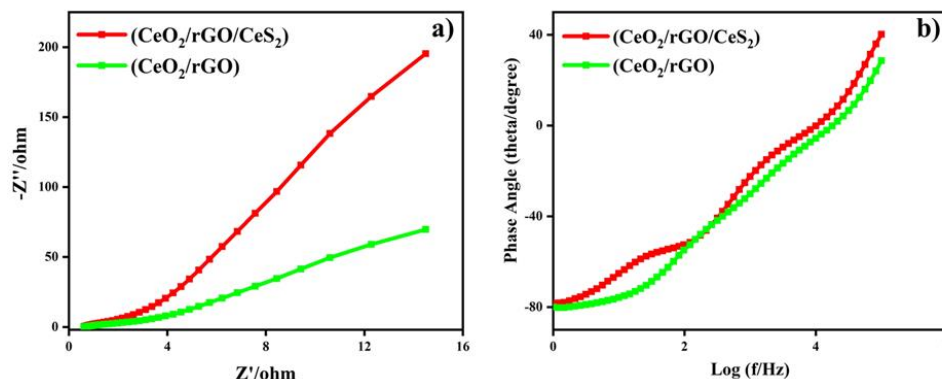


Figure 54. Electrochemical Impedance Spectroscopy (EIS) measurements, (a) Nyquist plot CeO₂/rGO and CeO₂/rGO/CeS₂, (b) Bode plot for CeO₂/rGO and CeO₂/rGO/CeS₂.

Similarly, the Bode plot of CeO₂/rGO/CeS₂ and CeO₂/rGO represents that at low-frequency regions the phase angle lies in the range of 70 to 80 degrees, which refers to the redox reactions and excellent capacitor behavior of the composites. The phase angle for the CeO₂/rGO/CeS₂ nanocomposite is relatively higher than the CeO₂/rGO composite, due to the good conductivity and good pseudocapacitance behavior. With the increase in frequency values, the phase angle decreases, which demonstrates the limited adsorption of the ions onto the surface of the electrode, which significantly reduces the number of active sites resulting in less specific capacitance.

Conclusions

This work comprises the synthesis, characterization, and electrochemical analysis of CeO₂/rGO/CeS₂ composite which was originated from Ce-BTC (MOF). The as-synthesized material composite was utilized as a promising material for electrode for supercapacitor applications. It demonstrated the greatest specific capacitance of 720 Fg⁻¹ at 10mVs⁻¹ scan rate, where the energy and power densities were calculated to be 23.5 Wh/kg and 2917.2 W/kg, respectively. The high conductivity of CeS₂ in the composite provided a platform for enhanced electron transfer among the electrolyte ions, and the porous electrode surface, while the CeO₂ provided better charge transport in the bulk. The large mesoporous configuration of the Ce-BTC MOF and the pseudo-capacitive performance of reduced graphene oxide enhanced the electrochemical behavior of the

electrode. The excellent cyclic stability showed by the electrode provides promising grounds for future research on the metal-oxide and metal-sulfide composites to be used as effective materials for electrodes for supercapacitor applications.

Acknowledgments

This research work has been supported and funded by the U.S.-Pakistan Center for Advanced Studies in Energy (USPCASE) at the National University of Science and Technology. The authors of this work are grateful for the technical support by the staff of the Energy Storage and Conservation lab.

References

- [1] K.A. Smith, Electrochemical Control of Lithium-Ion Batteries, *IEEE Control Syst.* 30 (2010) 18–25. <https://doi.org/10.1109/MCS.2010.935882>.
- [2] P.Y. Tang, Y.Q. Zhao, Y.M. Wang, C.L. Xu, A metal-decorated nickel foam-inducing regulatable manganese dioxide nanosheet array architecture for high-performance supercapacitor applications, *Nanoscale.* 5 (2013) 8156–8163. <https://doi.org/10.1039/c3nr02119j>.
- [3] J. Zhao, Y. Gao, A.F. Burke, Performance testing of supercapacitors: Important issues and uncertainties, *J. Power Sources.* 363 (2017) 327–340. <https://doi.org/10.1016/j.jpowsour.2017.07.066>.
- [4] H. Heydari, S.E. Moosavifard, S. Elyasi, M. Shahraki, Nanoporous CuS nano-hollow spheres as advanced material for high-performance supercapacitors, *Appl. Surf. Sci.* 394 (2017) 425–430. <https://doi.org/10.1016/j.apsusc.2016.10.138>.
- [5] Y.G. Zhu, G.S. Cao, C.Y. Sun, J. Xie, S.Y. Liu, T.J. Zhu, X.B. Zhao, H.Y. Yang, Design and synthesis of NiO nanoflakes/graphene nanocomposite as high performance electrodes of pseudocapacitor, *RSC Adv.* 3 (2013) 19409–19415. <https://doi.org/10.1039/c3ra42091d>.
- [6] R. Ramachandran, M. Saranya, P. Kollu, B.P.C. Raghupathy, S. Kwan Jeong, A. Nirmala Grace, Solvothermal synthesis of Zinc sulfide decorated Graphene

- (ZnS/G) nanocomposites for novel Supercapacitor electrodes, *Electrochim. Acta*. 178 (2015) 647–657. <https://doi.org/10.1016/j.electacta.2015.08.010>.
- [7] L. Wang, X. Feng, L. Ren, Q. Piao, J. Zhong, Y. Wang, H. Li, Y. Chen, B. Wang, Flexible solid-state supercapacitor based on a metal-organic framework interwoven by electrochemically-deposited PANI, *J. Am. Chem. Soc.* 137 (2015) 4920–4923. <https://doi.org/10.1021/jacs.5b01613>.
- [8] A. Afzal, F.A. Abuilaiwi, A. Habib, M. Awais, S.B. Waje, M.A. Atieh, Polypyrrole/carbon nanotube supercapacitors Technological advances and challenges, *J. Power Sources*. 352 (2017) 174–186. <https://doi.org/10.1016/j.jpowsour.2017.03.128>.
- [9] Q. Meng, K. Cai, Y. Chen, L. Chen, Research progress on conducting polymer based supercapacitor electrode materials, *Nano Energy*. 36 (2017) 268–285. <https://doi.org/10.1016/j.nanoen.2017.04.040>.
- [10] Y. Zhan, Y. Meng, N. Yan, Y. Li, D. Wei, X. Tao, Enhancing electrochemical performance of Fe₃O₄/graphene hybrid aerogel with hydrophilic polymer, *J. Appl. Polym. Sci.* 134 (2017) 45566. <https://doi.org/10.1002/app.45566>.
- [11] M. Lian, X. Wu, Q. Wang, W. Zhang, Y. Wang, Hydrothermal synthesis of Polypyrrole/MoS₂ intercalation composites for supercapacitor electrodes, *Ceram. Int.* 43 (2017) 9877–9883. <https://doi.org/10.1016/j.ceramint.2017.04.171>.
- [12] L. Lian, J. Yang, P. Xiong, W. Zhang, M. Wei, Facile synthesis of hierarchical MnO₂ sub-microspheres composed of nanosheets and their application for supercapacitors, *RSC Adv.* 4 (2014) 40753–40757. <https://doi.org/10.1039/c4ra07880b>.
- [13] Y. Wang, Z. Shi, Y. Huang, Y. Ma, C. Wang, M. Chen, Y. Chen, Supercapacitor devices based on graphene materials, *J. Phys. Chem. C*. 113 (2009) 13103–13107. <https://doi.org/10.1021/jp902214f>.
- [14] Y. Korenblit, M. Rose, E. Kockrick, L. Borchardt, A. Kvit, S. Kaskel, G. Yushin,

- High-rate electrochemical capacitors based on ordered mesoporous silicon carbide-derived carbon, *ACS Nano*. 4 (2010) 1337–1344.
<https://doi.org/10.1021/nn901825y>.
- [15] M. Kaempgen, C.K. Chan, J. Ma, Y. Cui, G. Gruner, Printable thin film supercapacitors using single-walled carbon nanotubes, *Nano Lett.* 9 (2009) 1872–1876. <https://doi.org/10.1021/nl8038579>.
- [16] Y. Wang, Y. Lei, J. Li, L. Gu, H. Yuan, D. Xiao, Synthesis of 3D-Nanonet Hollow Structured Co_3O_4 for High Capacity Supercapacitor, *ACS Appl. Mater. Interfaces*. 6 (2014) 6739–6747. <https://doi.org/10.1021/am500464n>.
- [17] Q. Li, Z.L. Wang, G.R. Li, R. Guo, L.X. Ding, Y.X. Tong, Design and synthesis of $\text{MnO}_2/\text{Mn}/\text{MnO}_2$ sandwich-structured nanotube arrays with high supercapacitive performance for electrochemical energy storage, *Nano Lett.* 12 (2012) 3803–3807. <https://doi.org/10.1021/nl301748m>.
- [18] Z.S. Wu, D.W. Wang, W. Ren, J. Zhao, G. Zhou, F. Li, H.M. Cheng, Anchoring hydrous RuO_2 on graphene sheets for high-performance electrochemical capacitors, *Adv. Funct. Mater.* 20 (2010) 3595–3602.
<https://doi.org/10.1002/adfm.201001054>.
- [19] H. Gao, K. Lian, Proton-conducting polymer electrolytes and their applications in solid supercapacitors: A review, *RSC Adv.* 4 (2014) 33091–33113.
<https://doi.org/10.1039/c4ra05151c>.
- [20] H. Gao, K. Lian, Characterizations of proton conducting polymer electrolytes for electrochemical capacitors, *Electrochim. Acta.* 56 (2010) 122–127.
<https://doi.org/10.1016/j.electacta.2010.09.036>.
- [21] Y. Zhao, Z. Song, X. Li, Q. Sun, N. Cheng, S. Lawes, X. Sun, Metal organic frameworks for energy storage and conversion, *Energy Storage Mater.* 2 (2016) 35–62. <https://doi.org/10.1016/j.ensm.2015.11.005>.
- [22] W. Xia, A. Mahmood, R. Zou, Q. Xu, Metal-organic frameworks and their derived

- nanostructures for electrochemical energy storage and conversion, *Energy Environ. Sci.* 8 (2015) 1837–1866. <https://doi.org/10.1039/c5ee00762c>.
- [23] A. Wahab, N. Iqbal, T. Noor, S. Ashraf, M.A. Raza, A. Ahmad, U.A. Khan, Thermally reduced mesoporous manganese MOF @reduced graphene oxide nanocomposite as bifunctional electrocatalyst for oxygen reduction and evolution, *RSC Adv.* 10 (2020) 27728–27742. <https://doi.org/10.1039/d0ra04193a>.
- [24] L. Yaqoob, T. Noor, N. Iqbal, H. Nasir, M. Sohail, N. Zaman, M. Usman, Nanocomposites of cobalt benzene tricarboxylic acid MOF with rGO: An efficient and robust electrocatalyst for oxygen evolution reaction (OER), *Renew. Energy.* 156 (2020) 1040–1054. <https://doi.org/10.1016/j.renene.2020.04.131>.
- [25] J. Kim, C. Young, J. Lee, M.S. Park, M. Shahabuddin, Y. Yamauchi, J.H. Kim, CNTs grown on nanoporous carbon from zeolitic imidazolate frameworks for supercapacitors, *Chem. Commun.* 52 (2016) 13016–13019. <https://doi.org/10.1039/c6cc07705f>.
- [26] B. Liu, H. Shioyama, T. Akita, Q. Xu, Metal-organic framework as a template for porous carbon synthesis, *J. Am. Chem. Soc.* 130 (2008) 5390–5391. <https://doi.org/10.1021/ja7106146>.
- [27] R.R. Salunkhe, Y.V. Kaneti, J. Kim, J.H. Kim, Y. Yamauchi, Nanoarchitectures for Metal-Organic Framework-Derived Nanoporous Carbons toward Supercapacitor Applications, *Acc. Chem. Res.* 49 (2016) 2796–2806. <https://doi.org/10.1021/acs.accounts.6b00460>.
- [28] A. Ahmad, N. Iqbal, T. Noor, A. Hassan, U.A. Khan, A. Wahab, M.A. Raza, S. Ashraf, Cu-doped zeolite imidazole framework (ZIF-8) for effective electrocatalytic CO₂reduction, *J. CO₂ Util.* 48 (2021) 101523. <https://doi.org/10.1016/j.jcou.2021.101523>.
- [29] R. Anwar, N. Iqbal, S. Hanif, T. Noor, X. Shi, N. Zaman, D. Haider, S.A. M. Rizvi, A.M. Kannan, MOF-Derived CuPt/NC Electrocatalyst for Oxygen Reduction Reaction, *Catalysts.* 10 (2020) 799.

<https://doi.org/10.3390/catal10070799>.

- [30] R. Ahmad, N. Iqbal, T. Noor, Development of ZIF-Derived Nanoporous Carbon and Cobalt Sulfide-Based Electrode Material for Supercapacitor, *Materials (Basel)*. 12 (2019) 2940. <https://doi.org/10.3390/ma12182940>.
- [31] R. Ahmad, N. Iqbal, M.M. Baig, T. Noor, G. Ali, I.H. Gul, ZIF-67 derived nitrogen doped CNTs decorated with sulfur and Ni(OH)₂ as potential electrode material for high-performance supercapacitors, *Electrochim. Acta*. 364 (2020) 137147. <https://doi.org/10.1016/j.electacta.2020.137147>.
- [32] S. Hanif, X. Shi, N. Iqbal, T. Noor, R. Anwar, A.M. Kannan, ZIF derived PtNiCo/NC cathode catalyst for proton exchange membrane fuel cell, *Appl. Catal. B Environ.* 258 (2019) 117947. <https://doi.org/10.1016/j.apcatb.2019.117947>.
- [33] L. Yaqoob, T. Noor, N. Iqbal, H. Nasir, N. Zaman, Development of Nickel-BTC-MOF-Derived Nanocomposites with rGO Towards Electrocatalytic Oxidation of Methanol and Its Product Analysis, *Catalysts*. 9 (2019) 856. <https://doi.org/10.3390/catal9100856>.
- [34] T. Noor, M. Ammad, N. Zaman, N. Iqbal, L. Yaqoob, H. Nasir, A Highly Efficient and Stable Copper BTC Metal Organic Framework Derived Electrocatalyst for Oxidation of Methanol in DMFC Application, *Catal. Letters*. 149 (2019) 3312–3327. <https://doi.org/10.1007/s10562-019-02904-6>.
- [35] S.A.M. Rizvi, N. Iqbal, M.D. Haider, T. Noor, R. Anwar, S. Hanif, Synthesis and Characterization of Cu-MOF Derived Cu@AC Electrocatalyst for Oxygen Reduction Reaction in PEMFC, *Catal. Letters*. 150 (2020) 1397–1407. <https://doi.org/10.1007/s10562-019-03024-x>.
- [36] R. Ahmad, U.A. Khan, N. Iqbal, T. Noor, Zeolitic imidazolate framework (ZIF)-derived porous carbon materials for supercapacitors: An overview, *RSC Adv.* 10 (2020) 43733–43750. <https://doi.org/10.1039/d0ra08560j>.
- [37] J. Yang, C. Zheng, P. Xiong, Y. Li, M. Wei, Zn-doped Ni-MOF material with a

- high supercapacitive performance, *J. Mater. Chem. A.* 2 (2014) 19005–19010.
<https://doi.org/10.1039/c4ta04346d>.
- [38] A. Hosseini, A.H. Amjad, R. Hosseinzadeh-Khanmiri, E. Ghorbani-Kalhor, M. Babazadeh, E. Vessally, Nanocomposite of ZIF-67 metal–organic framework with reduced graphene oxide nanosheets for high-performance supercapacitor applications, *J. Mater. Sci. Mater. Electron.* 28 (2017) 18040–18048.
<https://doi.org/10.1007/s10854-017-7747-z>.
- [39] P. Srimuk, S. Luanwuthi, A. Krittayavathananon, M. Sawangphruk, Solid-type supercapacitor of reduced graphene oxide-metal organic framework composite coated on carbon fiber paper, *Electrochim. Acta.* 157 (2015) 69–77.
<https://doi.org/10.1016/j.electacta.2015.01.082>.
- [40] P. Wen, P. Gong, J. Sun, J. Wang, S. Yang, Design and synthesis of Ni-MOF/CNT composites and rGO/carbon nitride composites for an asymmetric supercapacitor with high energy and power density, *J. Mater. Chem. A.* 3 (2015) 13874–13883.
<https://doi.org/10.1039/c5ta02461g>.
- [41] M. Saraf, R. Rajak, S.M. Mobin, A fascinating multitasking Cu-MOF/rGO hybrid for high performance supercapacitors and highly sensitive and selective electrochemical nitrite sensors, *J. Mater. Chem. A.* 4 (2016) 16432–16445.
<https://doi.org/10.1039/c6ta06470a>.
- [42] P.F. Santos, P.P. Luz, Synthesis of a CE-based MOF-76 with high yield: A study of reaction parameters based on a factorial design, *J. Braz. Chem. Soc.* 31 (2020) 566–573. <https://doi.org/10.21577/0103-5053.20190218>.
- [43] X. Lian, B. Yan, A lanthanide metal-organic framework (MOF-76) for adsorbing dyes and fluorescence detecting aromatic pollutants, *RSC Adv.* 6 (2016) 11570–11576. <https://doi.org/10.1039/c5ra23681a>.
- [44] G. Zeng, Y. Chen, L. Chen, P. Xiong, M. Wei, Electrochimica Acta Hierarchical cerium oxide derived from metal-organic frameworks for high performance supercapacitor electrodes, *Electrochim. Acta.* 222 (2016) 773–780.

<https://doi.org/10.1016/j.electacta.2016.11.035>.

- [45] R. Ramachandran, W. Xuan, C. Zhao, X. Leng, D. Sun, D. Luo, F. Wang, metal – organic framework based composite application †, *RSC Adv.* 8 (2018) 3462–3469. <https://doi.org/10.1039/C7RA12789H>.
- [46] N. Bibi, Y. Xia, S. Ahmed, Y. Zhu, S. Zhang, A. Iqbal, Highly stable mesoporous CeO₂/CeS₂ nanocomposite as electrode material with improved supercapacitor electrochemical performance, *Ceram. Int.* 44 (2018) 22262–22270. <https://doi.org/10.1016/j.ceramint.2018.08.348>.
- [47] Z. Gao, C. Wang, J. Li, Y. Zhu, Z. Zhang, W. Hu, Conductive Metal-Organic Frameworks for Electrocatalysis : Achievements, Challenges, and Opportunities, *Acta Phys. Chim. Sin.* 0 (2020) 2010025–0. <https://doi.org/10.3866/pku.whxb202010025>.
- [48] C.S. Lee, J.M. Lim, J.T. Park, J.H. Kim, Direct growth of highly organized, 2D ultra-thin nano-accordion Ni-MOF@NiS₂@C core-shell for high performance energy storage device, *Chem. Eng. J.* 406 (2021) 126810. <https://doi.org/10.1016/j.cej.2020.126810>.
- [49] X.H. Meng, C.B. Wan, X.P. Jiang, X. Ju, Rodlike CeO₂/carbon nanocomposite derived from metal–organic frameworks for enhanced supercapacitor applications, *J. Mater. Sci.* 53 (2018) 13966–13975. <https://doi.org/10.1007/s10853-018-2536-5>.
- [50] (15) A strawsheave-like metal organic framework Ce-BTC derivative containing high specific surface area for improving the catalytic activity of CO oxidation reaction, (n.d.). https://www.researchgate.net/publication/320365155_A_strawsheave-like_metal_organic_framework_Ce-BTC_derivative_containing_high_specific_surface_area_for_improving_the_catalytic_activity_of_CO_oxidation_reaction (accessed January 20, 2021).
- [51] T. Saravanan, M. Shanmugam, P. Anandan, M. Azhagurajan, K. Pazhanivel, M. Arivanandhan, Y. Hayakawa, R. Jayavel, Facile synthesis of graphene-CeO₂

nanocomposites with enhanced electrochemical properties for supercapacitors, *Dalt. Trans.* 44 (2015) 9901–9908. <https://doi.org/10.1039/c5dt01235j>.

- [52] M.M. Peng, M. Ganesh, R. Vinodh, M. Palanichamy, H.T. Jang, Solvent free oxidation of ethylbenzene over Ce-BTC MOF, *Arab. J. Chem.* 12 (2019) 1358–1364. <https://doi.org/10.1016/j.arabjc.2014.11.024>.
- [53] S.K. Jha, C. Naveen Kumar, R.P. Raj, N.S. Jha, S. Mohan, Synthesis of 3D porous CeO₂/reduced graphene oxide xerogel composite and low level detection of H₂O₂, *Electrochim. Acta.* 120 (2014) 308–313. <https://doi.org/10.1016/j.electacta.2013.12.051>.
- [54] E. Andrijanto, S. Shoelarta, G. Subiyanto, S. Rifki, Facile synthesis of graphene from graphite using ascorbic acid as reducing agent, in: *AIP Conf. Proc.*, American Institute of Physics Inc., 2016: p. 020003. <https://doi.org/10.1063/1.4945457>.
- [55] N.M.S. Hidayah, W.W. Liu, C.W. Lai, N.Z. Noriman, C.S. Khe, U. Hashim, H.C. Lee, Comparison on graphite, graphene oxide and reduced graphene oxide: Synthesis and characterization, in: *AIP Conf. Proc.*, American Institute of Physics Inc., 2017: p. 150002. <https://doi.org/10.1063/1.5005764>.
- [56] A.A. Ensafi, N. Ahmadi, B. Rezaei, Electrochemical preparation and characterization of a polypyrrole/nickel-cobalt hexacyanoferrate nanocomposite for supercapacitor applications, *RSC Adv.* 5 (2015) 91448–91456. <https://doi.org/10.1039/c5ra17945a>.